Title
Dayside Aurora and its Connection to the Solar Wind-Magnetosphere-Ionosphere Interaction

Author
Wang, Boyi

Publication Date
2018

Peer reviewed|Thesis/dissertation

UNIVERSITY OF CALIFORNIA

Los Angeles

Dayside Aurora and its Connection to the Solar Wind-Magnetosphere-Ionosphere Interaction

A dissertation submitted in partial satisfaction of the

requirements for the degree Doctor of Philosophy

in Atmospheric and Oceanic Sciences

by

Boyi Wang

2018

ABSTRACT OF THE DISSERTATION

Dayside aurora and its connection to

the solar wind-magnetosphere-ionosphere interaction

by

Boyi Wang

Doctor of Philosophy in Atmospheric and Oceanic Sciences

University of California, Los Angeles, 2018

Professor Lawrence R. Lyons, Chair

This dissertation presents a comprehensive study of the dayside auroral dynamics and remote sensing of coupled magnetosphere-ionosphere system responses to various upstream disturbances, which include interplanetary magnetic field (IMF) discontinuities, foreshock transients, and magnetosheath high speed jets (HSJs). Recent studies have shown that these disturbances have significant impacts on coupled magnetosphere-ionosphere system, changing the particle transportation and energy budget. However, it has been difficult to find spatial structure and evolution of the interaction processes using a limited number of in-situ measurements. This dissertation aims to understand how dayside aurora and airglow respond to upstream disturbances, and to utilize auroral imaging to determine how the magnetosphere-

ionosphere system responds to the upstream disturbances. Our study takes a unique approach by taking advantage of high-resolution 2D imaging to vastly increase community's understanding of magnetosphere-ionosphere responses to upstream disturbances, through tracing location, size and propagation of optical structures.

We first examine the role of IMF southward turnings as the trigger of Poleward Moving Auroral Forms (PMAFs), which are thought to be an ionospheric signature of dayside magnetic reconnection. While PMAFs are more likely to occur when the IMF is southward, how often PMAFs are triggered by changes in solar wind parameters is still a major open question and has only been poorly understood due to the use of solar wind monitors far away from the bow shock. This dissertation addresses this question with the conjunction between the all-sky imager (ASI) at Automatic Geophysical Observatories (AGO) P1 station in Antarctica and the Time History of Events and Macroscale Interactions during Substorms (THEMIS) B and C satellites, which provide much more accurate solar wind conditions than the solar wind monitors at the L1 point. In a statistical study using 60 PMAF events, 70% of the events show a reduction of IMF Bz before PMAF onset, which indicates that IMF southward turning plays an important role in triggering a majority of PMAFs.

Those PMAFs were further found to evolve to polar cap airglow patches. This dissertation investigates how often polar cap patches originate in PMAFs and are associated with flow channels, using the conjunction between the ASI at the AGO P1 station and DMSP satellites. Our 50-event statistical study shows that in a majority (45) of events, longitudinally narrow flow enhancements directed anti-sunward are found to be collocated with the patches, have velocities (up to a few km/s) substantially larger than the large-scale background flows (~500 m/s) and have widths comparable to patch widths (~400 km). The patches emanated out of

PMAFs and were found to have a large IMF By dependence on the MLT of patches entering the polar cap.

Through investigation of dayside aurora, we noticed that auroral brightenings can occur even without substantial changes in the IMF Bz or dynamic pressure. We examined whether disturbances generated in the foreshock and magnetosheath can contribute to dayside auroral brightening. Studies of the impact of foreshock and magnetosheath transients on the magnetosphere-ionosphere system are very limited, and it has been difficult to find how the transients interact in individual events due to limited in-situ and space-based imaging observations. In this dissertation, the conjunction between the ASI at South Pole and the THEMIS satellites during 2008 through 2011 is utilized to determine the magnetosphere-ionosphere responses to foreshock transients and magnetosheath HSJs in a 2D perspective.

In situ observation by the THEMIS satellites showed that a foreshock transient during 1535–1545 UT on 25 June 2008 was associated with magnetospheric compression. The ASI at South Pole observed that both diffuse and discrete aurora brightened locally soon after the appearance of this foreshock transient. With the advantage of the high-resolution 2D imaging, we were able to determine that the diffuse auroral brightening corresponds to a localized azimuthal extent of a few Re size on the equatorial plane, and propagated duskward with an average speed of ~100 km/s. Similarly, we for the first time show a nearly one-to-one relationship between the HSJs and individual localized discrete/diffuse auroral brightenings using eight HSJ events. The azimuthal size of HSJ-related diffuse auroral signatures is ~800 km at 230-km altitude in the ionosphere and ~3.7 Re in the magnetosphere, which is slightly larger but of the order of the cross-sectional diameter of HSJs (~1 Re). Furthermore, most of those

auroral signatures have azimuthal motions, whose magnitude and direction agree with magnetosheath background flows.

In addition to magnetospheric compression, foreshock transients were also found to cause Pc5-band (150-600s) ultra-low frequency (ULF) waves, which are important in transporting mass, energy and momentum in the coupled magnetosphere-ionosphere system. Although it is difficult to find spatial structure of dayside Pc5 waves by a small number of satellites or ground magnetometers, we have successfully determined the 2D structure and motion of ULF waves in the ionosphere using optical imagers. This dissertation reports two series of foreshock-driven Pc5 waves, which are found to be field line resonances (FLRs). The ground-based ASI at South Pole shows that periodic poleward moving east-west arcs are the ionospheric signature of FLRs. The azimuthal distribution, including dawn-dusk symmetricity and azimuthal wavenumbers, of the FLRs in the magnetosphere, are further determined by 2D imaging. The fine structure embedded in the large-scale arcs indicates a wave with high toroidal wavenumber ($m \sim 140$) was coupled with the FLRs. Based on these works, a likely scenario revealed from the satellite-imaging coordinated observations is as follows: Foreshock transients and magnetosheath HSJs drive compressions of the magnetopause at a few RE, much more localized than global compression by shocks. The compressions launch fast-mode waves and FLRs, which create localized electron precipitation and auroral brightenings. The auroral responses found in this study can highlight structure and evolution of the magnetospheric and ionospheric responses, and signify the geoeffectiveness of localized and transient upstream energy input.

The dissertation of Boyi Wang is approved.

Vassilis Angelopoulos

Jacob Bortnik

Toshi Nishimura

Lawrence R. Lyons, Committee Chair

University of California, Los Angeles

2018

Contents

List of Figures

List of Tables

Acknowledgments

I would like to thank my advisors, Prof. Larry Lyons and Prof. Toshi Nishimura, for their guidance, support and also continuing encouragements during these years at UCLA and Boston University. They are knowledgeable, creative and prominent scientists, who taught me a lot and very patiently. The discussion with them create important ideas in my research. I would also thank Prof. Vassilis Angelopoulos and Prof. Jacob Bortnik for their service on my thesis committee, and more importantly, I would thank them for their insightful comments/suggestions, encouragements and wonderful classes.

Many thanks to all my co-authors and collaborators who contribute greatly to the development of my research during these years: Dr. Heli Hietala for her inspiring ideas and patient instructions since our first discussion in 2016; Prof. Hui Zhang for the deep discussions and insightful suggestions during conferences and my visit to University of Alaska, Fairbanks; Prof. Quanqi Shi and Prof. Herbert C. Carlson for the inspiring discussions and their great comments/suggestions; Prof. Desheng Han for the deep discussions and patient instructions during conferences and his visit to UCLA; Dr. Ying Zou, for her patient instructions, especially when I nearly had no knowledge about aurora during my first graduate year at UCLA; Dr. Terry Z. Liu and Dr. Xiaochen Shen for the discussions and their patience in answering my questions with their expertise; Dr. Ferdinand Plaschke, Dr. Harald U. Frey, Dr. Stephen B. Mende, Dr. Yusuke Ebihara and Dr. Allan Weatherwax for providing data or event lists, which are so important to my research.

I would also like to thank all my colleagues in or ever in our research group, led by Prof. Larry Lyons. The discussions with them, about both academic topics and life, encouraged my

Ph.D. pursuit. I also would like to thank all the members in the research groups, led by Prof. Wen Li and Prof. Toshi Nishimura, respectively, at Boston University, for their helpful comments and suggestions on my research during my stay as a visiting student.

I thank all my friends in or ever in AOS and EPSS departments at UCLA. I always miss the days we went out together for meals, chatting, hiking and having a lot of fun. I would also thank all my CSP colleagues at Boston University for their help during my visit there since 2017.

Lastly, my sincere thanks go to my grandparents and parents, who always love and support me no matter what.

Boyi Wang
Boston, Massachusetts
November, 2018

Chapter 4 is a modified version of "**Wang, B.**, Y. Nishimura, Y. Zou, L. R. Lyons, V. Angelopoulos, H. Frey, and S. Mende (2016a). Investigation of triggering of poleward moving auroral forms using satellite-imager coordinated observations, J. Geophys. Res. Space Physics, 121, 10, 929-10, 941, doi: 10.1002/2016JA023128."

Chapter 5 is a modified version of "**Wang, B.**, Y. Nishimura, L. R. Lyons, Y. Zou, H. C. Carlson, H. U. Frey, and S. B. Mende (2016b), Analysis of close conjunctions between dayside polar cap airglow patches and flow channels by all-sky imager and DMSP, Earth Planets Space, 68(1), 150, doi:10.1186/s40623-016-0524-z."

Chapter 6 is a modified version of "**Wang, B.**, Nishimura, Y., Hietala, H., Shen, X.-C., Shi, Q., Zhang, H., et al. (2018a). Dayside magnetospheric and ionospheric responses to a foreshock transient on 25 June 2008: 2. 2D evolution based on dayside auroral imaging. Journal of Geophysical Research: Space Physics, 123, 6347–6359, doi: 10.1029/2017JA024846."

Chapter 7 is a modified version of "**Wang, B.**, Nishimura, Y., Hietala, H., Lyons, L., Angelopoulos, V., Plaschke, F., et al. (2018b). Impacts of magnetosheath high-speed jets on the magnetosphere and ionosphere measured by optical imaging and satellite observations. Journal of Geophysical Research: Space Physics, 123, 4879–4894, doi: 10.1029/2017JA024954."

Chapter 8 is a modified version of "**Wang, B.**, Yukitoshi Nishimura, Hui Zhang, Xiao-Chen Shen, Larry Lyons, Vassilis Angelopoulos, Yusuke Ebihara, Allan Weatherwax (2018c). 2D structure of foreshock driven Pc5 ULF waves observed by the THEMIS satellite and ground-based imager conjunctions. In preparation to be submitted to Journal of Geophysical Research: Space Physics"

This research was funded by NSF Grant PLR-1341359. We thank S. Mende and H. Frey for use of the AGO ASI data. The South Pole imager has been supported by a cooperative

agreement between NSF and the National Institute of Polar Research, Japan. The DMSP data are maintained by the Air Force Research Laboratory and Applied Physics Laboratory at Johns Hopkins University. All THEMIS data are from the THEMIS official website (http://themis.ssl.berkeley.edu/). The OMNI solar wind data were obtained from the CDAWeb.

VITA

2013	**B. A., Geophysics**
	School of Earth and Space Sciences
	University of Science and Technology of China (USTC), China
2016	**M.S., Atmospheric Sciences**
	Department of Atmospheric and Oceanic Sciences
	University of California, Los Angeles (UCLA), California, USA
2017	**Outstanding Student Poster Award** at the GEM Conference
2016-2017	**Teaching Assistant** at UCLA
2013-present	**Graduate Student Research Assistant** at UCLA

PUBLICATIONS

1. Nishimura, Y., **B. Wang**, Y. Zou, E. F. Donovan, V. Angelopoulos, et al. (2018). Transient solar wind-magnetosphere-ionosphere interaction associated with foreshock and magnetosheath transients and localized magnetopause reconnection, AGU Books, Accepted.

2. **Wang, B.**, Nishimura, Y., Hietala, H., Lyons, L., et al. (2018). Impacts of magnetosheath high-speed jets on the magnetosphere and ionosphere measured by optical imaging and satellite observations. J. Geophys. Res. Space Physics, 123, 4879–4894, doi: 10.1029/2017JA024954.

3. **Wang, B.**, Nishimura, Y., Hietala, H., Shen, X.-C., Shi, Q., Zhang, H., et al. (2018). Dayside magnetospheric and ionospheric responses to a foreshock transient on 25 June 2008: 2. 2-D evolution based on dayside auroral imaging. J. Geophys. Res. Space Physics, 123, 6347–6359, doi: 10.1029/2017JA024846.

4. Shen, X.-C., Shi, Q., **Wang, B.**, et al. (2018). Dayside magnetospheric and ionospheric responses to a foreshock transient on 25 June 2008: 1. FLR observed by satellite and ground-based magnetometers., J. Geophys. Res. Space Physics, 123, 6335–6346. doi: 10.1029/2018JA025349.

5. **Wang, B.**, Y. Nishimura, Y. Zou, L. R. Lyons, V. Angelopoulos, et al., (2016b). Investigation of triggering of poleward moving auroral forms using satellite-imager coordinated observations, J. Geophys. Res. Space Physics, 121, 10, 929-10, 941, doi: 10.1002/2016JA023128.

6. **Wang, B.**, Y. Nishimura, L. R. Lyons, Y. Zou, H. C. Carlson, et al. (2016a), Analysis of close conjunctions between dayside polar cap airglow patches and flow channels by all-sky imager and DMSP, Earth Planets Space, 68(1), 150, doi:10.1186/s40623-016-0524-z.

7. Wang, Y., **B. Wang**, C. Shen, F. Shen, and N. Lugaz (2014), Deflected propagation of a coronal mass ejection from the corona to interplanetary space, J. Geophys. Res. Space Physics, 119, 5117–5132, doi: 10.1002/2013JA019537.

INVITED ORAL PRESENTATIONS

the 5th Cluster-THEMIS Workshop Chania, Crete, 24-28 September, 2018

2D observation of foreshock-driven magnetospheric responses

Physics Department Seminar University of New Hampshire, April 25, 2018

Dayside MI responses to transient upstream disturbances

Physics Department Seminar University of Alaska, Fairbanks, March 09, 2018

Dayside M-I responses to transient upstream disturbances

Seminar Polar Research Institute of China, January 09, 2017

Solar wind/foreshock effects on dayside auroras

CHAPTER 1

General Introduction

The Earth's magnetosphere and ionosphere are located above the Earth's atmosphere that form as a result of Sun-Earth interaction. Those regions receive momentum and energy from the Sun and the solar wind, and their variable conditions create "space weather". Extreme events can have societal impacts such as satellite anomalies, radio communication disruptions, and satellite drag. Understanding the coupled magnetosphere and ionosphere system and their interaction with the solar wind is important for us to achieve physics understanding and forecast extreme space weather events. In this chapter, we give a general introduction and broad background on how the coupled magnetosphere-ionosphere system behaves under quiet and disturbed upstream space environment, and how optical emissions in the upper atmosphere (aurora and airglow) reveal dynamics in the coupled magnetosphere-ionosphere system for remote sensing. A more specific introduction and outstanding questions are given in Chapter 2.

1.1 Magnetospheric Convection under Steady Solar Wind Conditions

The Sun continuously emits supersonic plasma flows to the interplanetary space. These plasma flows, which are known as the solar wind, bring particles and energy from the sun toward Earth. The interplanetary magnetic field (IMF) is frozen into the solar wind due to the magnetic Reynolds number ($\mathcal{R}_m$) of the solar wind is about 10^{16}, which is high enough to be treated as an infinite electric conductivity in physics. As the solar wind propagates radially outward, with the rotation speed of the Sun, the field lines are bent into the Archimedes spiral [*Parker*, 1965]. The

spiral angle increases with radial distance from the Sun, and when solar wind arrives at Earth, it is approximately 45°.

Due to Earth's intrinsic magnetic field, when solar wind gets closer to the Earth, the solar wind flow is abruptly decelerated from supersonic to subsonic by the Earth's magnetosphere and deflects around it, forming the bow shock and magnetopause in front of the magnetosphere. The locations of the bow shock and magnetopause are mostly controlled by two parameters of the solar wind: a) the dynamic pressure, due to the balance between dynamic pressure in the solar wind and magnetic pressure in the magnetosphere; and b) the IMF, an inward displacement of the sunward magnetopause can be caused by the dayside low-latitude reconnection under southward IMF.

Besides the effect on the positions of bow shock and magnetopause, another important role of IMF in interaction with the Earth's magnetosphere is to control the magnetospheric convection. The low-latitude reconnection erodes the magnetic field lines around the reconnection site, and couples the Earth's intrinsic magnetic field and the IMF. Several statistical studies [e.g., *Holzer & Slavin*, 1979; *Lei et al*., 1981] have shown that coupling efficiency is ~20%, which means that ~20% of IMF that reaches the magnetopause penetrates into the magnetosphere. Those coupled magnetic field lines are very curved, so that they are carried to high latitudes by strong magnetic curvature force, and form open field lines at high latitudes. The coupled magnetic fluxes continue to move anti-sunward with the solar wind, which generate a large-scale convection electric field through the entire magnetosphere. This electric field is well known as the dawn-to-dusk electric field. The dawn-to dusk electric field also drives sunward flow into the closed field lines. The anti-sunward flows across the open field lines and the

sunward return flows in the magnetosphere form a closed circulation (see Figure 1.1a), which is known as magnetospheric convection or Dungey cycle [*Dungey*, 1961].

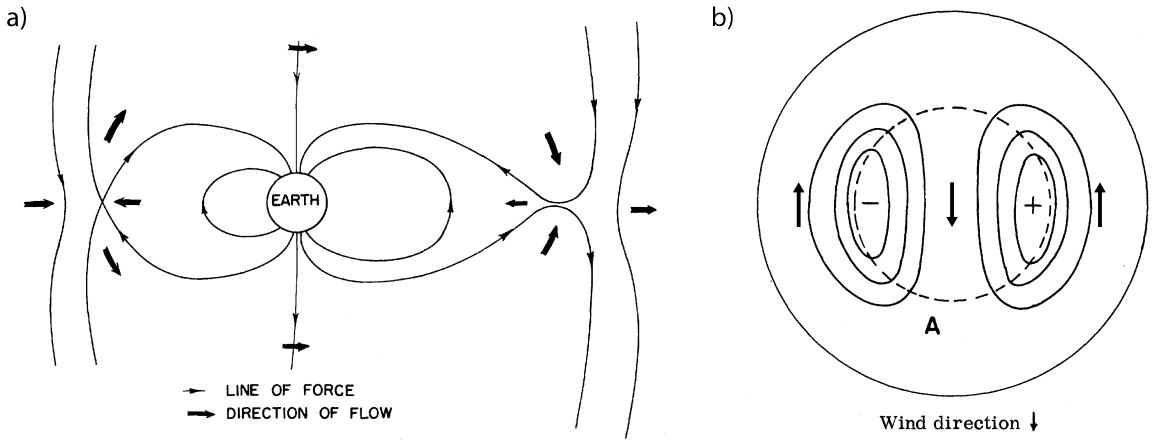

Figure 1.1 (a) Interplanetary plasma flow in a plane containing neutral points. Here, solid lines are magnetic field lines. (b) Equipotentials (solid lines within the solid circle) in northern hemisphere for plasma winds of panel (a). Here, dashed circle is the open-closed magnetic field boundary. [modified from Figure 1 and 2 of *Dungey*, 1961].

The particles in the nightside magnetosphere drift from the nightside to dayside after the nightside reconnection, which correspond to the return sunward flows in the convection pattern. As shown in Figure 1.1a, the return sunward flows in the Dungey cycle starts from the tail reconnection, which brings the open field lines from the lobes into the nightside magnetosphere. The nightside magnetic field is highly deviated from a dipole field. This magnetic field structure is associated with strong magnetic curvature, consistent with the existence of dawn-to-dusk electric field and a current sheet. This region is known as the plasma sheet. The plasma sheet has a thickness of less than 1 Re and a small z component magnetic field of less than 2 nT at ~20 Re from Earth in the nightside [*Paterson et al.*, 1998; *Plaschke et al.*, 2016; *Sergeev et al.*, 1996]. The particles, which enter the magnetosphere from lobes with sunward flows, undergo mainly

betatron and Fermi acceleration when passing through the plasma sheet. The acceleration makes plasma sheet particles to be ~a few tens of keV, which is much higher than solar wind particles (~a few keV). These particles can be further accelerated by betatron, Fermi acceleration and other mechanisms, such as radial diffusion and local wave heating, constructing the ring current, inner and outer radiation belts. Convection brings the particles with different energies from the nightside to dayside, forming similar particle structures in the dayside. Especially, although there is no highly curved magnetic field and current sheet in the dayside magnetic field, plasma sheet particles with a few tens of keV are still found in the dayside outer magnetosphere.

Due to the high conductivity in the magnetosphere, magnetospheric magnetic field lines can generally be treated as equipotentials. The magnetospheric convection can be mapped down to the ionosphere along the magnetic field lines. The anti-sunward flows across the open field lines correspond to the anti-sunward flows over the polar cap in the ionosphere. The sunward flows in the closed magnetosphere correspond to the return flows within the auroral oval, which is roughly at 67°-77° in magnetic latitudes during magnetically quiet times. The convection in the ionosphere consists of two cells, and it is named two-cell convection (Figure 1.1b).

The two-cell convection pattern shown in Figure 1.1b is symmetric but the symmetry is affected by the IMF By [*Reiff & Burch*, 1985; *Rich & Hairston*, 1994]. As shown in Figure 1.2a, with positive IMF By, convection is deflected westward by magnetic tension, which results in a shrunk dawnside cell and an expanded duskside cell. The pattern is opposite under negative IMF By.

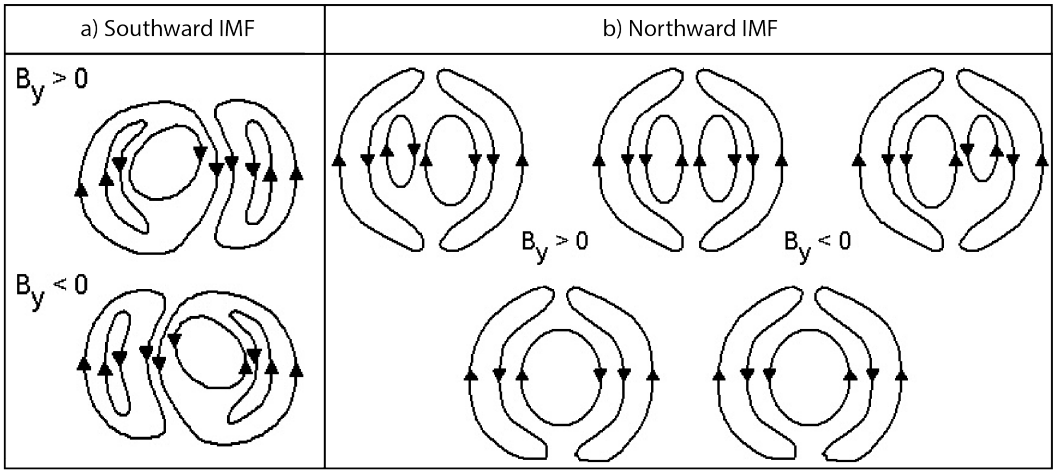

Figure 1.2 Convection patterns in the northern hemisphere, under different IMF conditions. The upper row of Panel (b) presents strong By condition while the lower row presents weak By condition. [*Reiff & Burch*, 1985]

The convection under northward IMF is predicted to be much more complicated. The reconnection may also occur during northward IMF but at higher latitudes and with lower efficiency in magnetic flux transfer than southward IMF [*Øieroset et al*., 1997]. Some observations indicated a four-cell pattern to be developed with northward IMF [*Burke et al*., 1979], as shown in the upper row of Figure 1.2b. Meanwhile, some other studies [e.g., *Burke et al*., 1979; *Rich & Hairston*, 1994] show that although three or four-cell pattern presented during northward IMF, they are not distributed as shown in Figure 1.2b. Rather, the extra cell(s) is(are) superimposed on the afternoon cell of the two-cell pattern.

1.2 Transient disturbances in the upstream region and their impacts on the coupled magnetosphere-ionosphere system

While the steady solar wind interacting with the geomagnetic field controls the large-scale plasma boundaries (i.e., the bow shock and the magnetopause), magnetospheric configuration, and convection patterns, there are also numerous types of transient disturbances in

the region upstream of the Earth's magnetosphere, which also interact with the earth's magnetosphere and leave significant impacts on the Earth's space environment.

The geoeffective disturbances can be generated in three upstream regions, which are solar wind, foreshock and magnetosheath. In this section, the transient disturbances in these three regions are introduced.

1.2.1 Solar wind transients

The transient disturbances in the solar wind are much larger than the Earth's magnetosphere, which usually cause global and significant impacts on the Earth. As we discussed in Section 1.1, the southward IMF can drive the coupling between the solar wind and magnetosphere with a high efficiency. In reality, a quasi-stationary solar wind usually does not contain long intervals of the southward IMF component since the field primarily lies on the ecliptic plane with small fluctuations in Bz. However, sometimes the large-scale disturbances propagate in the solar wind, such as interplanetary shocks (IP shocks), magnetic clouds (MC), corotating interaction region (CIR), coronal mass ejections (CME) and some other types that contain inside itself and/or modify an environment in such a manner that appreciable southward IMF can be present in the solar wind within several hours. Such a behavior of the IMF can result in energy input into the magnetosphere and in generation of magnetospheric disturbances, including geomagnetic storms [e.g., *Crooker & Cliver*, 1994; *Gonzalez et al*., 1999; *Gosling et al*., 1991; *Gosling & Pizzo*, 1999; *Mende et al*., 2009b].

Besides the sustained southward IMF, some solar wind transients, such as IP shocks and fast solar wind streams, are also associated with steep dynamic pressure changes. Such significant dynamic pressure changes, including positive and negative impulses, can compress or

inflate the magnetosphere, and in turn trigger global ultra-low-frequency (ULF) waves in the magnetosphere [*Zhang et al*., 2010; *Zong & Zhang*, 2011]. They also impact on the ionosphere significantly, by triggering travelling convection vortices (TCVs) and global auroral brightening [*Nishimura et al*., 2016; *Zhou et al*., 2009].

Although IP shocks are the most well-known source to generate magnetospheric compression and significant impacts on the coupled magnetosphere-ionosphere system in a global size, recent studies reported that, besides triggerred by large-scale interplanetary shock, magnetospheric compression can also occur with transient and localized disturbances in the foreshock and magnetosheath [*Hartinger et al*., 2013; *Hietala et al*., 2012; *Sibeck et al*., 1999], which are introduced in the following two subsections.

1.2.2 Foreshock transients

In addition to the effects on the convection pattern in the magnetosphere, the variation of IMF directions can also change the space environment in front of the bow shock. Here, the angle between the IMF and bow shock (denoted as θ_{BN}) is an important parameter. Generally, the bow shock conditions are divided to two categories; which are quasi-perpendicular ($\theta_{BN} > 45°$) and quasi-parallel ($\theta_{BN} < 45°$). Under the quasi-parallel shock condition, the upstream of bow shock is filled with backstreaming particles [e.g., *Eastwood et al*., 2005] which could originate from magnetospheric leakage or solar wind reflection [e.g., *Burgess et al*., 2012], forming a region called foreshock. Two types of reflections, i.e., specular reflection [*Fuselier*, 1995; *Gosling*, 1983] and adiabatic reflection [*Sonnerup*, 1969], occur in the foreshock ions. These backstreaming foreshock ions interact with the anti-sunward solar wind flows [*Omidi et al*., 2009], causing the foreshock to be highly dynamic, full of locally generated instabilities and

waves [*Eastwood et al*., 2005; *Fairfield et al*., 1990; *Paschmann et al*., 1981; *Yumoto*, 1985]. The foreshock usually stays in the dawnside since the quasi-parallel shock condition is satisfied in the dawnside under the Parker spiral IMF.

The transient kinetic processes in the foreshock can significantly modify the solar wind condition in front of the bow shock, generating transient and localized fluctuating structures, which are known as foreshock transients.

There are several types of foreshock transients, which are classified according to their properties and formation mechanisms. The most famous transients include hot flow anomalies (HFAs), spontaneous HFAs, foreshock bubbles (FBs), foreshock cavities, foreshock cavitons, foreshock compressional boundary, density holes, and short, large-amplitude magnetic structures (SLAMs). Most of these transients are associated with significant compressions and rarefactions [e.g., *Blanco-Cano et al*., 2011; *Schwartz*, 1995; *Sibeck et al*., 2002; *Turner et al*., 2013], which can potentially impact the magnetosphere and ionosphere.

HFAs, FBs, foreshock cavities, and density holes are often associated with IMF discontinuities in the solar wind [e.g., *Lin*, 1997; *Liu et al*., 2015; *Omidi et al*., 2010, 2013; *Wang et al*., 2013], while other transients could evolve from ULF waves or other physical processes in the foreshock [*Le & Russell*, 1992; *Schwartz et al*., 1992].

Unlike large-scale solar wind changes such as interplanetary shocks, foreshock transients are localized and short-lived. Their size and lifetime are between an ion gyroradius and a few Re, and from a few seconds to a few minutes, respectively [*Billingham et al*., 2011; *Omidi et al*., 2010, 2013; *Parks et al*., 2006]. Figure 1.3 shows a simulation of a foreshock cavity [*Omidi et al*., 2013], where the color indicates the density distribution. Foreshock cavity is formed within two tangential discontinuities (Figure 1.3a), and convecting along the bow shock with two

compressed boundaries. The compressed boundaries are localized and propagates azimuthally, which would compress the magnetosphere in the same manner. Similarly, HFAs are associated with flow deflections in the magnetosheath and deformation of the magnetopause, which results in various impacts on the magnetosphere including plasma injection into the cusp generation of field-aligned currents (FACs), triggering global-size Pc3 waves in the magnetosphere, and creating traveling convection vortices (TCVs) in the ionosphere [*Jacobsen et al*., 2009; *Omidi et al*., 2010; *Sibeck et al*., 1999; *Zhao et al*., 2017]. FBs also lead to transient magnetopause compression and ULF waves in the magnetosphere [*Archer et al., 2012; Hartinger et al*., 2013b; *Omidi et al*., 2010].

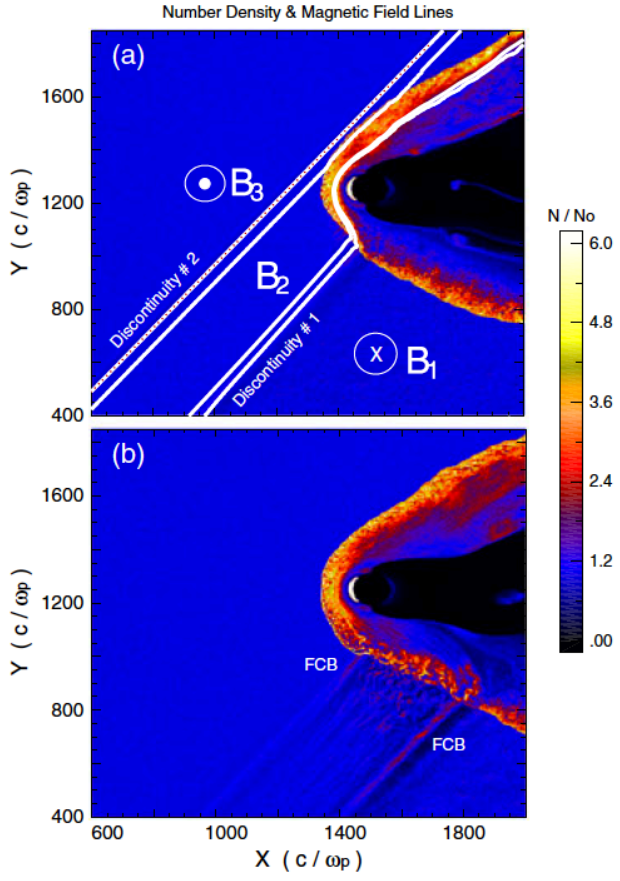

Figure 1.3 Plots of density at two times during the simulation. (a) Two discontinuities responsible for the changes in the IMF direction during the run of simulation. (b) Formation of a convecting foreshock bounded by two FCBs. [*Omidi et al*., [2013].

1.2.3 Magnetosheath Transients

The transient and localized disturbances can be generated not only in the foreshock, but also in the magnetosheath. The magnetosheath is the region downstream of the bow shock and its earthward boundary is the Earth's magnetopause. It is a highly turbulent region, consisting of subsonic flows moving around the magnetosphere. The region downstream from the quasi-parallel shock is called the quasi-parallel magnetosheath, where the plasma properties are more turbulent [e.g., *Fuselier et al*., 1991; *Gutynska et al*., 2012] while on the other hand, the region downstream from the quasi-perpendicular side is less turbulent.

The magnetosheath, especially quasi-parallel magnetosheath, generates a lot of transient and localized disturbances. Especially, transient impulses of the dynamic pressure in the magnetosheath are associated with increases in plasma density and antisunward flows [*Archer & Horbury*, 2013; *Hietala et al*., 2012; *Němeček et al*., 1998; *Plaschke et al*., 2009]. These characteristics in the subsolar magnetosheath are denoted as magnetosheath high-speed jets (HSJs) by *Hietala & Plaschke* [2013]. Their temporal scales are a few tens of seconds (median: 29s), which correspond to a median spatial-scale of ~4,000 km [*Plaschke et al*., 2016] in the geocentric solar magnetospheric (GSM) -X direction. The scale-size of HSJs perpendicular to their propagation directions is localized to ~1 Re based on the multisatellite observation [*Plaschke et al*., 2016] (shown in Figure 1.4a).

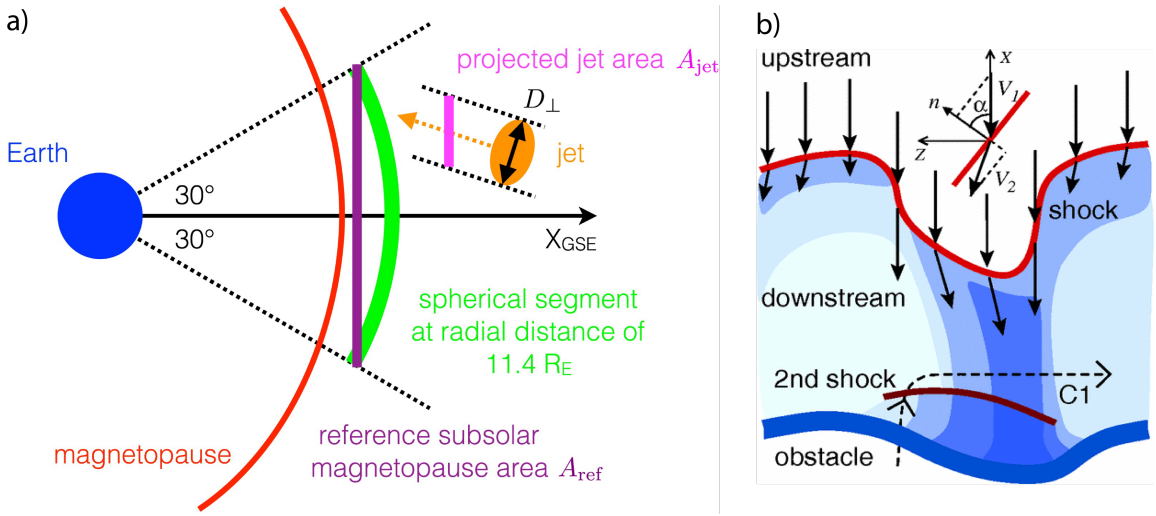

Figure 1.4 a) Sketch illustrating the reference and jet areas A_{ref} and A_{jet}perpendicular to the GSE x direction. [Figure 6 of Plaschke et al., 2016] b) Illustration of the effect of local shock curvature,. The variation of the plasma number density in the downstream region is illustrated by the shading: dark blue indicates density enhancement, light blue indicates density depletion. [Figure 1 of *Hietala et al.*, 2012]

Many HSJs can occur in the absence of dynamic pressure impulses in the solar wind. Some HSJs are generated by solar wind structures, including rotational discontinuities of the IMF [*Archer et al.*, 2012; *Dmitriev & Suvorova*, 2012; *Lin et al.*, 1996a, 1996b], HFAs in the foreshock [*Savin et al.*, 2012], and a rippled bow shock surface [*Hietala et al.*, 2009, 2012]. Recent papers show that HSJs tend to occur when the IMF cone angle is low, especially less than 40° [*Plaschke et al.*, 2013]. Among different possible sources of HSJs, a statistical study by *Hietala & Plaschke* [2013] showed that about 97% of the observed HSJs are generated due to the ripples of the quasi-parallel bow shock. The result of 2D hybrid simulation is also consistent with this proposed mechanism [*Hao et al.*, 2016, 2017; *Karimabadi et al.*, 2014].

HSJs could be geoeffective on a localized scale. When HSJs hit the magnetopause, an increase in dynamic pressure in the GSM-x direction compresses the magnetopause, causing indentations on the magnetopause [*Karimabadi et al.*, 2014; *Shue et al.*, 2009]. This could trigger

disturbances of the Chapman-Ferraro current system, magnetopause surface waves, and magnetospheric compressional waves (including Pc4-5 ULF; *Archer & Horbury*, 2013; *Hietala et al*., 2012; *Plaschke et al*., 2009; *Plaschke & Glassmeier*, 2011]. It also shows that localized magnetopause reconnection could be triggered by HSJs [*Hietala et al*., 2012, 2018], which potentially contributes to the energy input of the Earth's system. Besides, *Hietala et al*., [2012] reported a case showing that a dayside fast flow channel in the ionosphere, which was embedded in two-cell large convection, was probably triggered by an HSJ.

1.3 Aurora and Airglow

In order to explore the interaction between upstream conditions/disturbances and the Earth's coupled magnetosphere-ionosphere system, different instruments, including satellite instruments, ground-based magnetometers, radars and ground-based all sky cameras make their own contributions. In situ observations have an advantage in directly detecting and analyzing upstream disturbances with their magnetic field, electric field and particle structures. But the finite number of satellites limits its spatial coverage, failing to observe the events with larger scale than the separation between satellites. In contrast, space-based imaging is able to cover a large spatial range over the auroral zone, while the resolution is much lower than ground-based measurements and no emission filters exist to distinguish discrete aurora, diffuse aurora and airglow. Ground-based magnetometers and radars have an advantage of measuring magnetic field and flows, respectively, with a relatively higher resolution. However, among all the instruments, the ground-based all sky cameras have an advantage in identifying the types of aurora/airglow, and are able to provide a remote-sensing of the upstream activities in a horizontal 2D perspective and with the highest spatial resolution. Thus, aurora and airglow, which can

respond to upstream activities and also can be measured in ground-based optical imagers, are important to be studied.

1.3.1 Discrete and Diffuse Aurora

When electrons precipitate into the atmosphere and collide with ambient neutrals, the collisions will raise the particles to an excited energy state. The de-excitation of atomic oxygen and nitrogen molecules by radiation produces the aurora light. There are a lot of atoms or molecules in the Earth's atmosphere, such as N, O, N_2, N_2^+, O_2, O_2^+. They have specific excitation levels and the characteristic wavelength of typical emission lines. The 5577 Å green atomic oxygen line and the violet N_2^+ bands at 3914 and 4278 Å are the most intense emissions seen in the auroral zone, at ~100 km altitude *[Axelsson et al., 2014; Gulledge et al., 1968; Sakai et al.*, 2014]. The red 6300 Å oxygen band is also intense in the auroral zone, and the emission usually occurs at ~150-300 km altitude [*Solomon et al.*, 1988].

Aurora generally occurs within about 67°-77° in geomagnetic latitudes in both hemispheres during quiet space environment (shifting equatorward geomagnetically), forming a continuous band around the Earth. This region is called the auroral oval. In the auroral oval, aurora is found in different geometries and different colors, which indicates that there are different aurora categories. Typically, there are two categories of aurora, which are diffuse and discrete auroras.

Diffuse aurora is relatively homogeneous and often occur in the equatorward portion of the auroral oval, as a relatively faint but almost permanent band. They are primarily generated by electron cyclotron harmonic waves and whistler mode waves scattering energetic electrons into the loss cone [*Ashour-Abdalla & Kennel*, 1978; *Devine et al.*, 1995; *Horne et al.*, 2003; *Li et al.*,

2009, 2011; *Ni et al*., 2008; *Nishimura et al*., 2010a, 2013; *Tao*, 2014; *Thorne et al*., 2010]. Those energetic electrons, with a range of 0.1 to 30 keV, usually come from the plasma sheet [*Han et al*., 2015; *Thorne et al*., 2010; *Meng & Akasofu*, 1983; *Meng et al*., 1979; *Rearwin & Hones*, 1974]. And due to the corresponding energy range, they usually have much stronger green-line emission than red-line emission. Thus, green-line emission measured by ground-based cameras can provide a remote sensing of the disturbances in the magnetosphere (especially the plasma sheet) by identifying their diffuse auroral responses.

Compared to diffuse aurora, discrete aurora is highly structured and dynamic. They often occur at poleward portion of the auroral oval and the polar cap (such as polar cap arcs). The discrete aurora is associated with the precipitation produced by locally accelerated electrons through an electrostatic field along the magnetic field. This electric field can cause a total parallel potential drop of 1-10 kV [*Hull et al*., 2003], generating FACs that connect to the ionosphere. The downward currents are carried by upward ionospheric electrons and the upward currents are carried by downward magnetospheric electron fluxes. Discrete aurora is always associated with upward FACs.

The discrete aurora-related electric fields could be generated by a shear in plasma bulk velocity and/or a gradient of plasma kinetic pressure in the magnetosphere [*Echim et al*., 2009]. An example is the auroral streamers, which are equatorward-moving north-south discrete auroral forms in the nightside. The auroral streamers are the ionospheric projection of upward field-aligned currents forming on the western edge of earthward flow bursts in the plasma sheet [*Echim et al*., 2009; *Lyons et al*., 1999; *Nakamura et al*., 2001; *Nishimura et al*., 2010b; *Sergeev et al*., 2000].

Discrete aurora generally intensifies in both green and red-line emission, but in most cases, they are more intense in red-line emission than in green-line emission. Thus, the red-line emission snapshots taken by ground-based aurora can help to identify discrete aurora, and in turn highlight upward FACs that are associated with magnetospheric disturbances [*Cowley*, 2013; *Maltsev & Lyatsky*, 1975].

1.3.2 Airglow

As discussed in the previous subsection, besides the auroral oval, discrete aurora can also occur in the polar cap. At the same time, another type of emission, called "airglow patches", is also found in the polar cap. However, the physics mechanism of airglow formation is different from aurora.

Airglow patches are identified as enhanced red-line emissions, and the emission intensity is determined by the magnitude and the altitude of plasma peak density [Barbier & Glaume, 1962]. They are high-density plasma with ~100-1000 km in size and their density is typically 2-10 times higher than the surrounding plasma. Airglow patches result from recombination between electrons and molecular oxygen ions by solar EUV radiation [*Weber & Buchau*, 1981]. Those solar-EUV-produced ionospheric plasma enters the polar cap through the cusp dayside auroral region [*Carlson*, 2012]. Their slow (~hours) F region recombination allows their motion to be tracked over long distances and it is found that they cross the polar cap with a timescale of ~2 hours [*Oksavik et al*., 2010]. Some airglow patches are found to stop and decay within the polar cap [*Hosokawa et al*., 2011], while some are reported to continue to exit the polar cap entering the nightside auroral oval [*Zhang et al*., 2013; *Nishimura et al*., 2014] and turn into auroral blobs [*Crowley et al*., 2000]. Thus, patches are not just high-density ionosphere plasma

but highlight active plasma and energy transport across the open field lines. However, there are still some puzzles existing with airglow patches, including the physical mechanisms of patch production and transpolar evolution.

For patch production, there are several processes proposed to explain why sunlit plasma enters the polar cap as patches instead of a continuous tongue. Some studies show that time-dependent motion of the large-scale convection could generate airglow patches [*Sojka et al*., 1993; *Valladares et al*., 1998]. Other studies suggest that some meso-scale bursty flows, which are probably related to transient magnetopause reconnection, i.e. FTEs, are involved in the creation of localized patch structures [*Lockwood & Carlson*, 1992; *Carlson et al*., 2006].

As for the transpolar evolution of airglow patches, it has been believed to follow large-scale two cell convection during southward IMF [*Carlson*, 2012; *Hosokawa et al*., 2010; *Oksavik et al*., 2010]. Correspondingly, the IMF By, which impacts the convection patterns, also controls dawn-dusk motion of patches in the same manner [*Hosokawa, et al*., 2009]. Convection within the polar cap is often assumed to consist of relatively uniform anti-sunward flow with a typical speed of several hundreds of m/s [*MacDougall & Jayachandran*, 2001]. However, there are some recent papers presenting the simultaneous occurrence of airglow patches and meso-scale fast flow channels in the polar cap, which also suggested that the airglow patches are generated by reconnection bursty flows and the patches would propagate over the polar cap with the fast flows [*Nishimura et al*., 2014; *Zou et al*., 2014].

CHAPTER 2

Literature Review and Objectives

Chapter 1 provides a background about basic properties of the coupled magnetosphere-ionosphere system interacting with the upstream environment, auroras and airglow. Chapter 2 more specifically describes current understanding of how upstream processes impact the magnetosphere-ionosphere system particularly in optical emission, and states outstanding questions, limitations of past approaches, and uniqueness of our investigation. We particularly focus on the common types of dayside aurora: poleward moving auroral forms (PMAFs), diffuse/discrete auroral brightening, and periodic poleward moving east-west arcs, which are believed to be related to upstream disturbances.

2.1 Ionospheric signature of FTEs – Poleward moving auroral forms (PMAFs)

PMAFs are one of the most distinct discrete auroral forms in the dayside auroral oval and were first described by *Vorobjev et al*., [1975] as dayside auroral structures associated with poleward motion during the expansion phase of a substorm. PMAFs typically form at the equatorward boundary of the dayside auroral oval, propagate into the polar cap, and end by fading away in the polar cap ~500 km poleward, as shown in Figure 2.1 [*Fasel*, 1995; *Sandholt et al*., 1986]. Recently, PMAFs were reported to leave polar cap patches behind [*Lorentzen et al*., 2010] and also to propagate across the polar cap and lead to nightside auroral activity, showing a nearly continuous sequence from a dayside PMAF to nightside auroral brightening [*Nishimura et*

al., 2014]. Thus, it is important to determine triggering processes of PMAFs for understanding not only dayside auroral physics but also the polar cap and nightside activities.

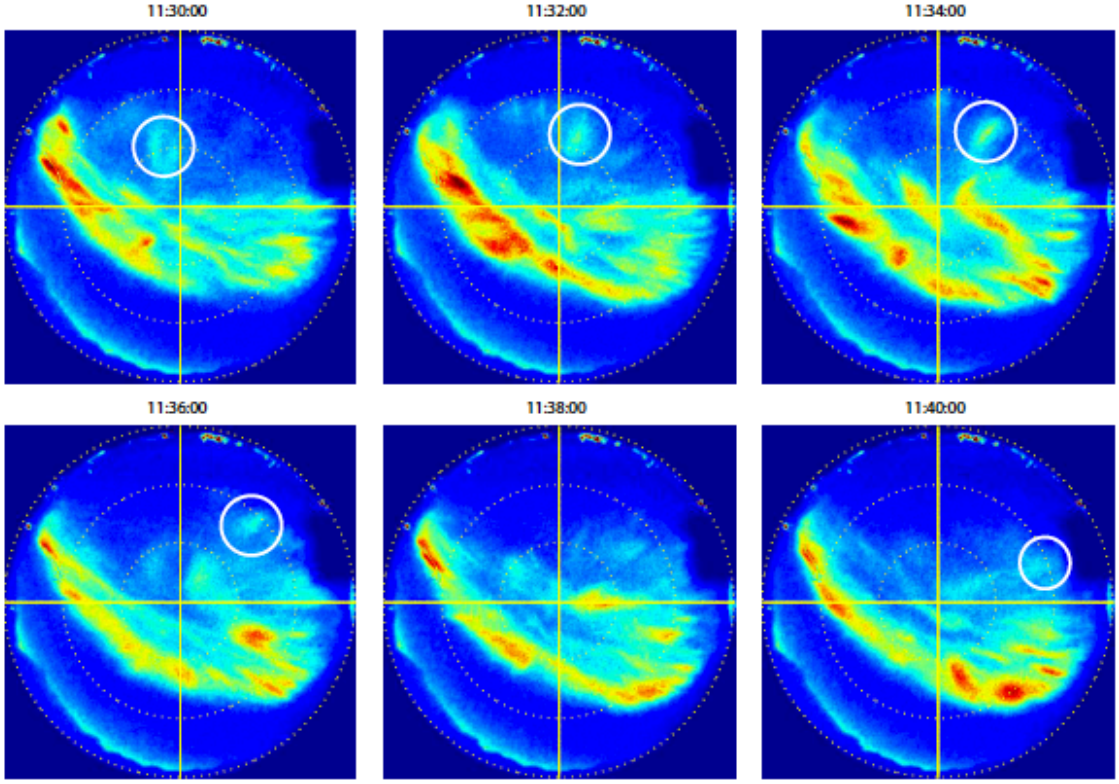

Figure 2.1 ASI image sequence in the red-line emission for the interval 11:30–11:40 UT on 30 November, 1997. The coordinate system is zenith angle vs. azimuth angle with respect to magnetic north. The central vertical line (yellow) marks the 15:00 MLT meridian. Magnetic north is up and west to the left in each image. [Figure 3 of *Sandholt & Farrugia*, 2007].

The dayside auroral oval and PMAFs are strongly dependent on the orientation of the IMF. During the southward IMF, the dayside auroral oval shifts equatorward [*Sandholt et al*., 1983], and PMAFs start with equatorward boundary intensifications (EBIs) [e.g., *Fasel et al*., 1992]. PMAFs are often recurrent with a periodicity of 5-15 minutes and each PMAF lasts for 2-10 minutes [*Sandholt et al*., 1986]. The periodicity, lifetime and motion of PMAFs are similar to flux transfer events (FTEs), which are widely believed to be the transient reconnection that occurs at the dayside magnetopause, and thus PMAFs are considered as an ionospheric signature

of transient dayside reconnection, e.g., FTEs [*Sandholt et al*., 1986; *Sandholt et al*., 1989a]. Multiple FAC structures observed by *Sandholt et al*., [1989b] during a satellite crossing over a sequence of PMAFs has been confirmed by modeling works and observation as FTEs [*Lockwood et al*., 2001b]. Furthermore, associations between EBIs/PMAFs and ion precipitation in the cusp have indicated that PMAFs may occur on newly reconnected field lines [*Farrugia et al*., 1998; *Sandholt et al*., 2003; *Yeoman et al*., 1997].

Besides reconnection induced by IMF Bz changes, IMF By, solar wind pressure pulses, and foreshock phenomena could also modulate dayside reconnection and thus drive PMAFs. *Sandholt et al*., [1986] presented evidence that PMAFs have smaller latitudinal/longitudinal extent and shorter time duration when the IMF By is large. It has been suggested that PMAFs are associated with lobe cells and merging cells, distorted by prevailing By conditions [*Sandholt et al*., 2001]. An IMF By-related prenoon-postnoon asymmetry of PMAF occurrence has also been reported [*Karlson et al*., 1996; *Sandholt et al*., 1993; *Sandholt & Farrugia*, 1999].

Sudden brightening of the dayside auroral oval has also been found to follow HFAs in several coordinated observations [*Fillingim et al*., 2011; *Sibeck et al*., 1999; *Vorobjev et al*., 2001]. Although those studies did not focus on PMAFs, HFAs are thus also a possible trigger for PMAFs after dayside auroral brightenings. PMAFs have been considered as a possible source of ULF wave signatures in the cusp [*Engebretson et al*., 2009], and *Hartinger et al*., [2013] proposed transient ion foreshock phenomena as a driver of ULF waves. Thus, foreshock phenomena may be related to PMAFs and ULF waves. Additionally, HSJs are reported to be associated with localized ionospheric velocity bursts [*Hietala et al*., 2012; *Plaschke et al*., 2013]. The ionospheric flow shear associated with such bursts indicates FACs, which are directly

related to auroral precipitation. Associations between PMAFs and solar wind pressure pulses have also been reported [*Lui & Sibeck*, 1991; *Mende et al*., 2009a; *Sibeck*, 1992].

By knowing the possible relation between PMAFs and different upstream disturbances, it becomes important to understand the probability of those upstream disturbances in triggering PMAFs. And especially, we want to identify whether IMF Bz variances play the most important role in PMAF triggering, as most of the previous case studies show their relation to PMAF occurrence. To answer those questions, accurate measurements of the solar wind and foreshock phenomena in conjunction with imaging are important. However, many of the past studies before the Time History of Events and Macroscale Interactions during Substorms (THEMIS) era used solar wind measurements far away from the bow shock nose and thus may have been limited by large uncertainties in propagation time estimates or by missing structures in an inhomogeneous solar wind that did not pass satellite locations. Thus, it is necessary to measure IMF structures, dynamic pressure and also foreshock phenomena near the dayside bow shock to examine the trigger of PMAFs.

2.2 The evolution of PMAFs in the polar cap − Airglow Patches

PMAFs were recently reported to leave polar cap patches behind [*Carlson*, 2012; *Lorentzen et al*., 2010], to propagate across the polar cap, and to lead to nightside auroral activity, showing a nearly continuous sequence from a dayside PMAF to nightside auroral brightening [*Nishimura et al*., 2014]. Based on those case studies, it is interesting to statistically analyze whether PMAFs tend to fade away near the poleward boundary of dayside auroral oval or continue propagating further into the polar cap in other forms. Thus, as part of our second sub-topic, we examine the evolution of PMAFs in the polar cap.

As shown in Subsection 1.3.2, airglow polar cap patches were believed to follow large-scale two cell convection during southward IMF [*Carlson*, 2012; *Hosokawa et al*., 2010; *Oksavik et al*., 2010]. However, in contrast, around the dayside cusp region, plasma flow observations have shown dynamic meso-scale (of the order of 100 km) structures, which are typically ~2 km/s, that may be involved in the creation of localized patch structures [*Carlson et al*., 2006; *Moen et al*., 2008; *Oksavik et al*., 2004, 2005; *Pinnock et al*., 1993; *Rinne et al*., 2007; *Zhang et al*., 2013a]. *Zhang et al*., [2013a] also suggested that flow bursts lead to the formation of patches. Those fast flows are also associated with PMAFs [*Moen et al*., 1995; *Provan et al*., 1998, 1999; *Provan & Yeoman*, 1999; *McWilliams et al*., 2000; *Milan et al*., 2000; *Sandholt & Farrugia*, 2003; *Carlson et al*., 2006; *Lockwood et al*., 2005; *Zhang et al*., 2011, 2013b], which indicates the connection between PMAFs and polar car airglow patches. However, flow observations associated with polar cap patch propagation are limited in the dayside polar cap, and thus there has not been a systematic study of whether or not dayside polar cap patches propagate deep into the polar cap after patch formation associated with the meso-scale flow channels.

Furthermore, some polar cap patches have also been shown to propagate deep into the polar cap and reach the nightside polar cap [*Oksavik et al*., 2010]. *Zhang et al*., [2013a] showed that airglow patches can even exit the polar cap through magnetic reconnection and enter the nightside auroral oval. Polar cap patches in the nightside auroral oval were reported to connect to auroral poleward boundary intensifications (PBIs) and streamers [*Lorentzen et al*., 2004; *Moen et al*., 2007; *Nishimura et al*., 2013]. On the other hand, recent radar observations have shown the existence of meso-scale fast flows deep within the nightside polar cap, propagating with airglow patches, toward the nightside auroral oval, as shown in Figure 2.2 [*Lyons et al*., 2011; *Nishimura et al*., 2010b; *Zou et al*., 2014]. The similarities between meso-scale flow channels in the dayside

cusp and within the nightside polar cap, as well as the patch propagation from the dayside to nightside polar cap, suggest that meso-scale fast flows in the dayside oval propagate deep into the polar cap [*Wilder et al*., 2012 and references therein]. Recently, *Nishimura et al*., [2014] showed a nearly continuous sequence from a dayside PMAF to nightside PBIs, across the polar cap, associated with meso-scale fast flows.

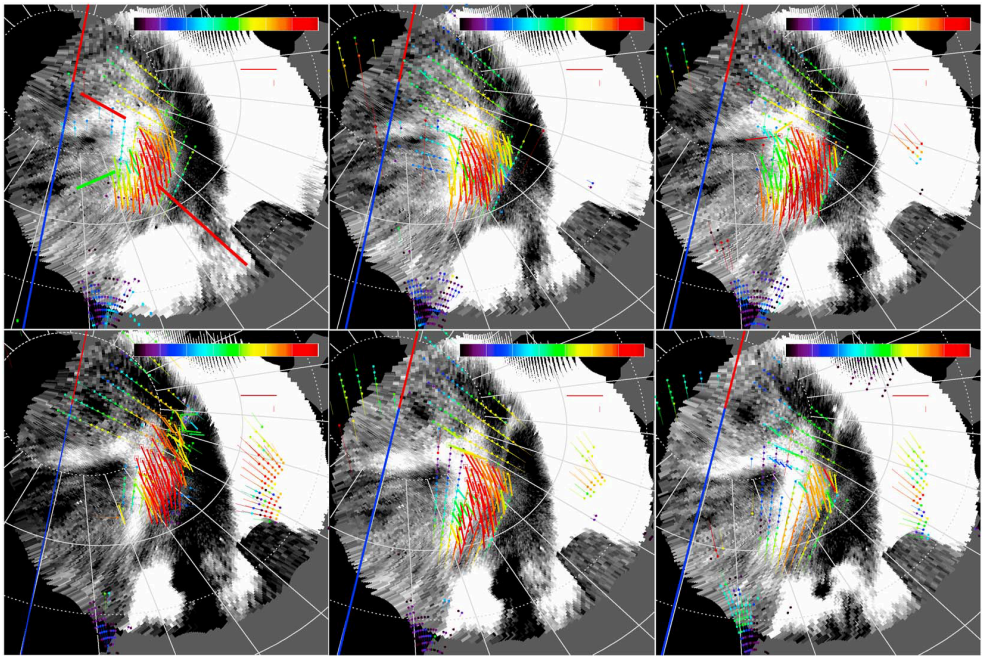

Figure 2.2 (a–f) Snapshots showing polar cap flow structures surrounding an airglow patch on 1 December 2011 based on coordinated observations of the Resolute Bay ASI and SuperDARN at RKN and INV. The radar measurements are shown as thick and thin arrows representing merged 2D flow vectors and LOS velocity, respectively. The color and the length of the arrows indicate the flow speed, and the arrow direction with respect to each dot (for LOS) or empty square (for merge vectors) gives the flow direction. The ASI images were taken in the red-line emission and are shown in a grey scale. The bright crescent on the dawn side is due to intense auroral emissions of the dawnside auroral oval. [Figure 1 of *Zou et al*., 2015].

At the beginning of airglow patch formation on the dayside, they have been found in association with rapid flow channels, which are typically ~2 km/s [*Carlson*, 2012]. *Zhang et al*. [2013a, b] also suggested that flow bursts lead to the formation of patches. However, flow observations associated with polar cap patch are limited in the dayside polar cap, so that there

has not been a systematic study of whether or not dayside polar cap patches are associated with these mesoscale flow channels propagating deep into the polar cap after patch formation. To investigate the relation between airglow patches and mesoscale flows in the dayside polar cap, we use coordinated observations by one of the Automatic Geophysical Observatories (AGO) all-sky imagers (ASIs) in Antarctica, and the Defense Meteorological Satellite Program (DMSP) satellites. While airglow patch emissions primarily occur below 300 km altitude, density enhancements associated with airglow patches have been known to extend to much higher altitudes along the magnetic field lines. For example, *Carlson et al*., [2006] used optical imaging and the European Incoherent Scatter (EISCAT) Svalbard radar, showing that density enhancements associated with patches extend to 600 km altitude or higher. *Hosokawa et al*., [2009] used DMSP and imager data, as we do in this study, showing that the density enhancements at DMSP altitude (~830 km) correspond to airglow patches. ASI observations can trace 2D motions of airglow patches over long distances. Although the imaging in the dayside polar cap is very limited due to sunlight and clouds, the AGO imagers have multi-years of records of dayside emissions without sunlight contamination and in low cloudiness (~10%). While radar backscatter echo regions are generally not sufficiently large to investigate flow structures around dayside polar cap patches, low-altitude satellite observations can provide both density and velocity over a wider region along their trajectories, and their conjunctions with imagers occur routinely, allowing us to perform a statistical study of airglow patches and related flow structures in the dayside polar cap. We note that, although low-altitude satellite observations have been used to study PMAFs [e.g., *Lockwood et al*., 2001a; *Sandholt et al*., 2004], studies using conjunctions with dayside polar cap patches [*Hosokawa et al*., 2010] have been rare.

2.3 Diffuse and discrete auroral brightenings during magnetospheric compressions

Although the IMF orientation changes can trigger auroral forms like PMAFs as shown in previous sections, the upstream dynamic pressure variations, including both global and localized variations, also have corresponding auroral responses.

Many previous works have shown that intensification of dayside aurora, both diffuse and discrete aurora, can be caused by upstream dynamic pressure enhancements. However, most studies focused on large-scale interplanetary shock/pressure pulses, which are well known as shock aurora [*Holmes et al*., 2014; *Tsurutani et al*., 2001; *Zhou et al*., 2003]. How the magnetosphere-ionosphere system responds to localized upstream transient phenomena is poorly understood.

Discrete aurora is generated by electrons accelerated along the magnetic field lines and is associated with upward FACs. Thus, discrete aurora can be used to highlight upward FACs associated with dayside magnetopause disturbances [*Cowley*, 2013; *Maltsev & Lyatsky*, 1975]. *Nishimura et al*., [2016] shows that after sudden commencements (SCs), which are associated with solar wind dynamic pressure impulse, discrete aurora always brightens concurrently with FACs.

As introduced in Subsection 1.3.1, diffuse aurora is generated by electron cyclotron harmonic waves and whistler mode waves scattering energetic electrons into the loss cone. When a compression pulse, e.g. IP shock, hits the Earth, diffuse aurora brightens through almost the entire auroral oval, as shown in Figure 2.3, where the black arrow indicates the arrival time of the IP shock at the Earth. It is because the IP shock compresses the magnetosphere, which leads

to wave intensification and the subsequent electron scattering. Thus, diffuse auroral brightenings can display the area of the dayside magnetosphere where particle anisotropies increase by magnetospheric compression, thereby leading to enhanced wave power and subsequent electron scattering.

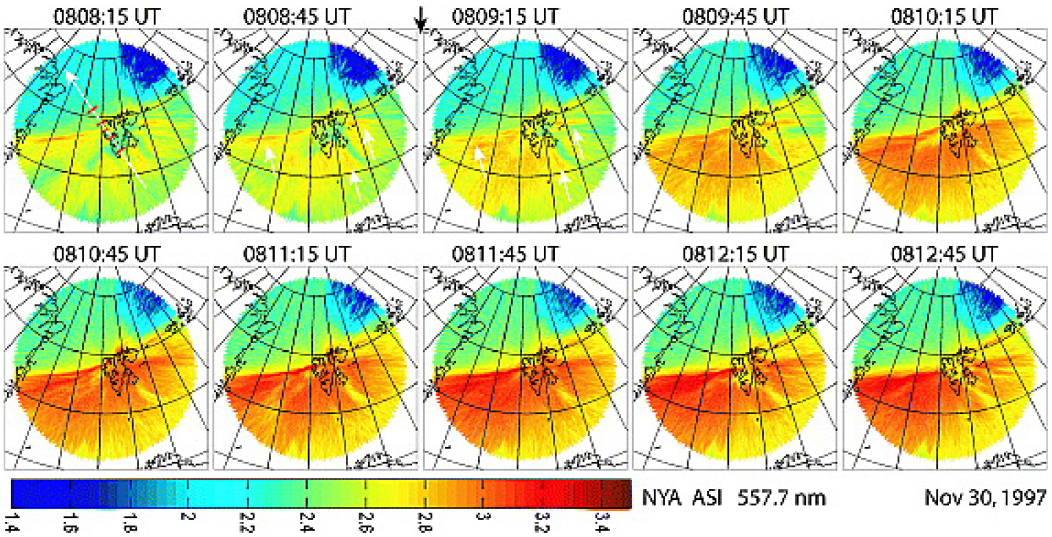

Figure 2.3 Ny Ålesund green-line emissions of the shock aurora on 30 November 1997. Grids in images are in geographic coordinates. The white arrow in the first image points to the magnetic north. The black arrow on top shows that the shock arrival time at Earth was between 0808:45 and 0809:15 UT (Sudden commencement at ~0809 UT). The color bar on the bottom indicates the logarithm (base 10) of the sensor response rate, which is proportional to the auroral emission intensity. [Figure 2 of *Zhou et al*., 2009]

Since foreshock transients and magnetosheath HSJs are able to deform the magnetopause locally and induce magnetosperic disturbances, auroral brightenings are expected to occur associated with such compressions, and if so, their 2D sequences would allow to determine the size, location and propagation of disturbances imposed to the magnetosphere-ionosphere system, and their differences from the responses during IP shocks, both of which are difficult to examine using a limited number of in-situ satellites.

2.3.1 Foreshock-related auroral brightening

Although the previous studies showed that foreshock transients were geoeffective, it has been difficult to accurately detect structure and evolution of the influences on the coupled magnetosphere-ionosphere system because measurements are often limited to several data points or by global imaging with coarse resolution.

Since foreshock transients also induce magnetopause disturbances, auroral brightenings are expected to occur. *Sibeck et al*., [1999] presented auroral brightening followed an HFA. However, their study was not able to identify the type of aurora or its evolution (which was rapid and thus time-aliased) due to limited spatial and temporal resolution of space-based imaging.

The availability of multipoint measurements near the magnetopause from the THEMIS satellites together with high-resolution imaging (spatial and temporal) of the dayside aurora enables far more detailed studies of these phenomena than ever before. In Chapter 6, we demonstrate that this method is able to reveal some of the auroral characteristics associated with the interaction between foreshock transients and the magnetosphere. We present a foreshock transient event that occurred during a conjunction between the THEMIS satellites and an ASI at South Pole on the dayside. This conjunction event provides a simultaneous multipoint observation from interplanetary space to auroral regions through the foreshock, magnetosheath, and magnetosphere. 2D imaging gives us the information of structure and evolution of both diffuse and discrete auroral patterns in its field of view (FOV). By mapping auroral patterns to the equatorial plane in the magnetosphere, the mapped pattern can reveal the size and evolution of the related upstream activities in a 2D perspective.

2.3.2 HSJ-related auroral brightening

Different from foreshock transients, the responses to magnetosheath HSJs are currently poorly understood. In Chapter 7, we address if HSJs affect dayside aurora, and if so, what types of aurora respond to HSJs. Since magnetosheath HSJs are also associated with magnetopause disturbances and compression as described above, corresponding discrete and diffuse auroral responses are expected to occur.

Without auroral observation, due to a limited number of measurement points by satellites and ground magnetometers in the previous HSJ studies, it is difficult to find accurate structure and evolution of the influences of HSJs on the coupled magnetosphere-ionosphere system. However, when discrete and diffuse aurora responses to HSJs can be observed in conjugate to the satellites, ground-based imaging can provide high-resolution 2D measurements of HSJ-driven ionospheric disturbances and corresponding magnetospheric signatures. Such observations can reveal location, size, and propagation of the effects of HSJs in much greater detail than by other types of measurements, in particular in situ, point measurements.

By surveying conjunctions between the THEMIS satellites and an ASI at South Pole on the dayside during 2008 through 2010, eight HSJ events were identified for further studying of their auroral responses, and two of those are presented as case studies in Chapter 7. We also show a multi-event study based on the eight HSJ events.

2.4 Periodic poleward moving east-west arcs as modulated by Pc5 ULF waves

Besides compressing or rarefying the dayside magnetosphere, upstream dynamic pressure variation is also an external resource of magnetospheric Pc5 waves [e.g., *Claudepierre et al*., 2010; *Kepko et al*., 2002; *Shi et al*., 2013; *Zhang et al*., 2010; *Zong et al*., 2009]. Pc5 waves are

the ULF waves with 150-600s period. The Pc5 waves that are driven by upstream dynamic pressure variations include compressional magnetohydrodynamic (MHD) waves and field line resonances (FLRs).

FLRs are resonant shear Alfvenic oscillations on closed magnetic field lines, associated with the frequencies of a few mHz, which are usually within the Pc5 frequency range. FLRs can occur where the compressional wave frequency matches the local field-line eigenfrequency [*Glassmeier*, 1995]. They are considered to be excited by solar wind drivers [*Farrugia et al*., 2000], KHIs at flank magnetopause [*Samson et al*., 1992] or magnetospheric cavity modes [*Harrold & Samson*, 1992; *Kivelson & Southwood*, 1986]. Statistical studies presented a strong dawn-dusk asymmetry of the occurrence rate and amplitude of toroidal Pc5 waves (e.g., FLRs) in both in situ and ground observation [*Engebretson et al*., 1998; *Gupta*, 1975; *Rae et al*., 2012; *Takahashi et al*., 2016]. This asymmetry is probably caused by the asymmetric distribution of the energy sources of toroidal Pc5 waves, and thus the KHIs and the foreshock, which have the same dawn-dusk asymmetry, became most likely candidates of the energy source of FLRs [*Spreiter et al*., 1966; *Takahashi et al*., 2016]. However, whether foreshock transients can drive FLRs in the dayside magnetosphere is still poorly understood. Thus, our study discover whether foreshock transients can be a source of magnetospheric FLRs by in situ and ground-based observation.

On the other hand, theory and simulation showed wave power structure of FLRs in the azimuthal direction on the equatorial plane [*Allan et al*., 1985; *Claudepierre et al*., 2010; *Ellington et al*., 2016; *Gallagher et al*., 2000; *Lee & Lysak*, 1989]. But because of low spatial resolution of ground based magnetometers and limited coverage of in situ observation, it is difficult to determine the azimuthal structure of FLRs in the dayside magnetosphere. However, the 2D information of FLRs, can be obtained by ground-based optical imagers with a larger

spatial coverage and high resolution. Especially, the wavenumber of FLRs can potentially be determined.

The ionospheric features of FLRs have been observed by radars [*Ruohoniemi et al*., 1991; *Samson et al*., 1992], ground-based magnetometers [*Ziesolleck & McDiarmid*, 1994] as well as in optical images [*Milan et al*., 2001; *Rae et al*., 2007; *Rankin et al*., 2005; *Samson et al*., 1991; *Tanaka et al*., 2012; *Xu et al*., 1993]. These ground-based observation, which usually have sufficient azimuthal coverage, can help measure the 2D information of FLRs. They showed the full width at half maximum (FWHM) of FLRs is ~0.6-2° latitude in the ionosphere [*McDiarmid et al*., 1994; *McDiarmid & Allan*, 1990; *McDiarmid & Nielsen*, 1987; *Walker*, 1987]. It is much larger than the theoretical minimum FLR width in the magnetospheric equatorial plane, which was evaluated as 0.005 Re, which was about 0.0002° latitude in the ionosphere [*Newton et al*., 1978]. This difference was interpreted as the damping effect due to ionospheric Joule dissipation, which spreads FLR in the ionosphere.

Shear Alfven waves have been studied extensively in theory and observation about the role they play in forming discrete temporally modulated auroral arcs [*Chen & Hasegawa*, 1974; *Samson et al*., 1971]. The FLR-related arcs behave significantly different from PMAFs as introduced in Section 1.1. They always occurred below the dayside discrete auroral oval and propagate poleward periodically within a few degrees, while PMAFs are generated in the dayside discrete auroral oval and not necessarily with an about constant period. The red-line emission keogram in Figure 2.4 shows the periodic poleward moving auroral arcs below 75°, which was the auroral signature of FLRs. The auroral oval was the red region above 75°, which showed that the arcs were below the auroral oval. The poleward propagation of those east-west arcs was interpreted as the 180° phase difference of the wave electric field across the resonance latitude

[*Knox & Allan*, 1981; *Wright & Allan*, 1996]. This leads to a zero-crossing of the electric field moving across the resonance region, giving a repetitive phase propagation.

However, although ground-based observation is capable of showing spatial distribution of aurora associated with ULF waves, there has been no study examining 2D structure of FLR driven by foreshock transients. Thus, in Chapter 8, we examine 2D structure of Pc5 ULF waves driven by foreshock disturbances by taking advantage of coordinated observation from the solar wind, magnetosphere, to ionosphere on June 29, 2008 for determining the upstream source and auroral responses of two Pc5 waves. The auroral response further allows to measure azimuthal distribution of these foreshock driven FLRs in the dayside magnetosphere and ionosphere, and also the north-south width of their ionospheric signatures.

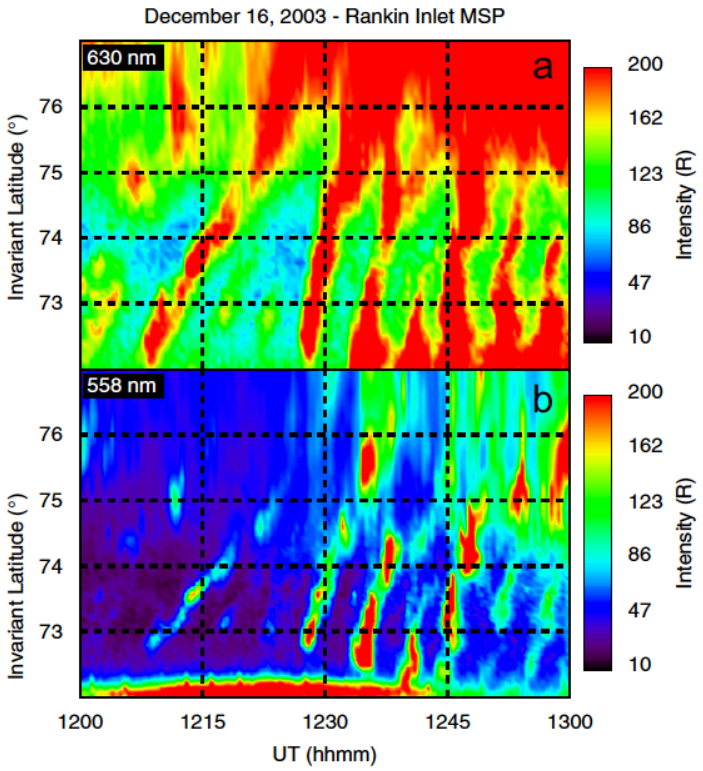

Figure 2.4 Meridian scanning photometer data from Rankin Inlet for the interval 12-13UT 16 December 2003 in: (a) red-line and (b) green-line emissions, mapped onto an invariant latitude, assuming emission heights of 230 and 110 km, respectively. [Figure 5 of *Rae et al*., 2007].

2.5 Goals of this dissertation

This dissertation aims to understand how dayside aurora and airglow respond to upstream disturbances, and to utilize auroral imaging to determine how the coupled magnetosphere-ionosphere system responds to the upstream disturbances in a 2D perspective that cannot be done or is only possible in much lower resolution by any other means of measurements. In order to approach this goal, we address five specific issues:

(1) Identifying the upstream trigger of PMAFs (Chapter 4).

Past case studies have shown that PMAFs can be triggered by IMF southward turnings and can occur spontaneously under steady southward IMF. However, how commonly PMAFs are triggered is still an open question, and accurate IMF observations near the bow shock are critical. The coordinated observations are utilized to examine the role of IMF southward turning and foreshock phenomena in triggering dayside PMAFs. Furthermore, the IMF observed by THEMIS B/C can be compared with that obtained by OMNI (coming from WIND and ACE), in order to see the structures different from those inferred from L1 need to be considered. Additionally, foreshock ions can also be examined as a possible candidate for triggering PMAFs.

(2) Identify the evolution of PMAF in the polar cap (Chapter 5).

Airglow patches are found to be related to magnetopause bursty reconnection, i.e. FTEs, which are the magnetospheric signature of PMAFs. In this dissertation, we will evaluate the relation between PMAFs and polar cap airglow patches, whether the FTE-related meso-scale bursty flows are commonly associated with the airglow patches and whether the flows contribute to the anti-sunward motion of airglow patches over the polar cap. By using coordinated observations by the ASI at the AGO P1 station in Antarctica and the Defense Meteorological

Satellite Program (DMSP) satellites, the evolution of PMAFs, and the relation between airglow patches and meso-scale flows in the dayside polar cap can be investigated.

(3) Determine the M-I coupled responses to foreshock transient in a 2D perspective (Chapter 6).

Recent studies on foreshock transients have shown their significant impacts on the Earth's magnetosphere and ionosphere. However, it has been difficult to trace the impacts driven by foreshock transients in a 2D perspective in the coupled magnetosphere-ionosphere system. In Chapter 6, we take advantage of coordinated observation between the ASI at South Pole and the THEMIS satellites to identify the diffuse and discrete auroral responses to foreshock transients, and furthermore, those auroral responses are utilized to determine the structure and evolution of foreshock transients in a 2D perspective and a high resolution.

(4) Determine the M-I coupled responses to magnetosheath HSJs in a 2D perspective. (Chapter 7)

Magnetosheath HSJs have been found to be geoeffective in recent years. However, whether aurora responds to HSJs is still poorly understood. With the conjunction between the ASI at South Pole and the THEMIS satellites, how diffuse and discrete auroras respond to magnetosheath HSJs are identified. If aurora is found to respond, the linkage between specific auroral activities and magnetosheath HSJs is used to determine the 2D structures of magnetosheath HSJs by mapping auroral patterns to the equatorial plane.

(5) Measure the M-I coupled responses to foreshock-driven Pc5 waves in a 2D perspective (Chapter 8).

Although a few examples of contemporaneous measurements of optical and magnetospheric signatures of FLRs exist, the 2D structure and even the existence of FLR driven by foreshock transients is still poorly understood. In Chapter 8, we identify the 2D structure of foreshock-driven FLR by using the conjunction between the THEMIS satellites and optical imagers by the ASI at South Pole.

CHAPTER 3

Instrumentation

3.1 Satellites

1) THEMIS

The THEMIS spacecraft was launched on 17 February, 2007. It consists of five spacecraft, which are placed in highly elliptical orbits where the spacecraft line up at apogee every four days [*Angelopoulos*, 2009]. The apogee rotates slowly around the Earth to cover the dayside, dawnside, nightside and duskside of the magnetosphere. During 2008-2010, THEMIS B and C (ARTEMIS) had not become moon orbit yet and still orbited the Earth at 20-30 Re away, while THEMIS A, D, E also orbited Earth but mostly in the magnetosphere. It provided an advantage to observe solar wind conditions near the Earth (by THEMIS B and C) and the concurrent magnetospheric conditions (by THEMIS A, D and E) during these years, which are benefit to study the interactions between the solar wind and magnetosphere.

The instruments onboard THEMIS are electric field instruments (EFI), fluxgate magnetometers (FGM), search coil magnetometers (SCM), electrostatic analyzers (ESA), solid state telescopes (SST) and mechanical drawings, which are used to measure magnetic field, electric field, energy flux of electrons/ions, plasma speed, and electron pitch angles.

2) DMSP

The DMSP satellites consist of multiple spacecraft, which are polar orbiting, Sun synchronous (i.e., fixed local time) and axis stabilized (since DMSP 5A/F1). They orbit Earth

every ~101 minutes with an inclination of 98.9° and an altitude of about 830 km [*Gussenhoven et al*., 1981; *Hardy et al*., 2008].

DMSP satellites (F13, F15, F16, F17 and F18) provide measurements of plasma density, flow and particle precipitation using the ion scintillation monitor (SSIES) and precipitating electron and ion spectrometer (SSJ/4). Compared to radars, whose echo coverage is generally sparse, low-altitude satellite observations can provide density, velocity and precipitation across the polar cap along their track. The precipitating particle data are used to validate the optical auroral poleward boundary location along the satellite tracks. The DMSP satellites enter the FOV of AP1 several times per day, providing a high chance of conjunctions with airglow patches.

3) WIND and ACE

In order to measure IMF in the undisturbed solar wind and also contribute to 3D IMF structure calculation, WIND and ACE data are also utilized in this dissertation.

The WIND is a spin stabilized spacecraft launched on November 1, 1994. Since 2004, WIND have been placed in a halo orbit around the L1 Lagrange point, which is more than 200 Re upstream of Earth. The instrument of Magnetic Field Investigation (MFI) onboard WIND is used to measure IMF around L1 point. The ACE satellite, which was launched on August 25, 1997, also orbit around L1 point. The magnetometer instrument onboard ACE can measure the IMF there.

3.2 All sky imagers (ASIs)

1) ASI at AGO station

The monochromatic ASIs of the AGO network in Antarctica acquire images in two different wavelengths: 630.0 (red line) and 427.8 nm (blue line) [*Mende et al*., 1999]. Among the AGO stations, the P1 (83.86°S, 129.61°E in geographic; 80.14°S, 16.87°E in magnetic) station, which has the longest record and stays in the polar cap for almost all times on the dayside, is used to identify PMAFs and dayside airglow patches in this dissertation (Chapter 4 and 5). This ASI records imager data every minute with two different exposure times. We used the long-exposure mode (8s) for maximizing the chance of detecting faint airglow patches. Data of red-line emission are mapped to 230 km altitude and are used to observe both auroral and airglow emissions. Since blue-line emission is only sensitive to energetic electron precipitation, these two wavelengths can be used to distinguish auroral and airglow emissions. Images are digitized and scaled between 0 and 255 in arbitrary intensity units. Poleward boundaries of the auroral oval are deduced from the blue-line emission and are checked using the electron precipitation data from the DMSP conjunctions.

We assume that the altitude of images observed by red-line emissions is 230 km since the most significant red emissions occur at this altitude. Similarly, we map blue-line emission snapshots to 110 km. These are typical mapping altitudes at these wavelengths [*Axelsson et al*., 2014; *Gulledge et al*., 1968; *Sakai et al*., 2014]. However, there are some errors associated with this mapping. To estimate the errors, we use intensity profiles for airglow red emission presented by *Sakai et al*., [2014], which showed that the airglow emission of polar cap patches is peaked at ~280 km altitude during disturbed time. The errors from the 230 km altitude mapping can be estimated as:

$$W_{280} - W_{230} = W_{230} \times (280 - 230)/230 \approx 0.21 \times W_{230}$$

where W_{230} and W_{280} denote the horizontal lengths at different altitudes.

Thus, the uncertainty of W_{230} is about 20%. This is not negligibly small but indicates that W_{230} gives a reasonable estimate of a horizontal length. For most of the airglow patches in this dissertation (Chapter 5; ~300 km width), the uncertainties are approximately a few tens of kilometers.

2) ASI at South Pole station

The monochromatic ASI at South Pole station in Antarctica [*Ebihara et al*., 2007] is used to identify dayside discrete and diffuse aurora in this dissertation (Chapter 6, 7 and 8). Local noon of South Pole station is at ~1530 UT. This ASI records imager data every ~40 s in the 557.7 (green line) and 630.0-nm (red line) wavelengths. The pixels of the imager are 512×512, giving a spatial resolution near the zenith of ~360 m. The sensitivity of the imager is ~35 Rayleigh in green-line emission and ~40 Rayleigh in red-line emission. Red-line emissions are sensitive to soft (<~1 keV) electron precipitation and can be used to observe discrete aurora commonly seen near the dayside open-closed field line boundary [*Lorentzen et al*., 1996]. Red-line data are mapped to 230-km altitude as a representative altitude of emission due to low-energy precipitation [*Solomon et al*., 1988]. Green-line emissions equatorward of red-line emissions can be used to identify diffuse aurora, which comes from high-energy (>~1 keV) precipitation on closed field lines [*Lorentzen et al*., 1996; *Lorentzen & Moen*, 2000; *Meng et al*., 1979; *Sandholt et al*., 2002]. Green-line emission data are mapped to 110-km altitude as a representative altitude of emission due to a relatively higher energy precipitation [*Mende et al*., 1993].

3.3 Ground-based magnetometers

The ground-based magnetometers at high latitudes in the northern hemisphere can be utilized to calculate the horizontal currents, which can help examine the existence of TCVs (Chapter 6). Besides, southern hemisphere magnetometers at B10 (-77.32° in geographic latitude; 39.71° in geographic longitude) and B23 (-88.02° latitude; 316.13° longitude) stations, and the conjugate location of the northern hemisphere magnetometers at IQA (63.75° latitude; 291.48° longitude), and STF (67.02° latitude; 309.28° longitude) stations have good conjunction with the ASI at South Pole. They provides an opportunity to compare ionospheric wave signatures with optical images (Chapter 8).

CHAPTER 4

The role of IMF southward turning in triggering PMAFs

In this chapter, the upstream trigger of PMAFs is identified, by using the coordinated observation by the ASI at the AGO P1 station and the THEMIS satellites. The criteria and date set are desciebed in Section 4.1; four events, including three cases with IMF southward turning in the solar wind and one case with foreshock disturbances, are shown in Section 4.2; an superposed epoch analysis is presented in Section 4.3; and Section 4.4 gives a discussion and summary.

4.1 Criteria and data set

THEMIS B and C flew close to the bow shock in 2008, 2009 and 2011, and their 2 and 4-day orbital periods are favorable for conjunctions with the Antarctic ground-based ASIs. And PMAFs are identified by one of the monochromatic ASIs of the AGO network in Antarctica [*Mende et al*., 1999].

To investigate how often PMAFs are triggered by IMF changes, we have surveyed coordinated observations between the AGO ASI and the THEMIS satellites in all the southern winter months (from April to September) during 2007-2011. We focused on dark and clear sky conditions within the ASI FOV during ~1230-1930 UT (~0800-1600 MLT). PMAFs were identified in the red-line emission as >~20 intensity units above background (2-hour average

intensity) for at least 5 minutes, propagating poleward from the dayside auroral oval. Here the choice of 20 intensity unit is arbitrary but is empirically set to be substantially larger than small intensity fluctuations and to select large PMAFs that can be identified in keograms.

To identify IMF structures, at least one of the THEMIS satellites should be in the solar wind within ±3 h in MLT of the central meridian of the ASI FOV. During 2008-2009, THEMIS B and C were located within 30 Re from the Earth, and thus provided solar wind measurements close to the bow shock. THEMIS B and C became ARTEMIS and provided solar wind measurements at ~50 Re since 2011. The AGO AP1 data became unavailable starting in 2012. Thus the THEMIS B/C-AP1 combination in the southern winter seasons of 2008, 2009 and 2011 provides an ideal set of observations in the solar wind and auroral oval. We also referred to OMNI data for comparison. Based on these criteria, we found a total of 60 PMAFs with THEMIS conjunction observations for our analysis.

Additionally, we check foreshock phenomena for PMAFs that are not associated with IMF southward turning. Detection of foreshock ions needs stricter criteria in distance from the Earth. To identify potential cases in conjunction with reflected ions, we require THEMIS should not only be located with ~0800-1600 MLT but also no farther than 20 Re from the Earth.

4.2 Case Study

4.2.1 First Event: 5 June, 2008

Figures 4.1a-4.1c show magnetic field data obtained from THEMIS B, C and OMNI, respectively, from 1550 to 1800 UT on June 05, 2008. The conjunction period of this case is from 1600 to 1800 UT, selected by the criteria shown above. The blue, green and red curves present the Bx, By and Bz components of the magnetic field, respectively. THEMIS C was

located in the magnetosheath, detecting large fluctuations of the magnetic field (as expected in a turbulent sheath) that are not seen by THEMIS B or OMNI, while the overall trend is similar to the THEMIS B measurements. In this study, we focus on the IMFs that were obtained from THEMIS B and OMNI.

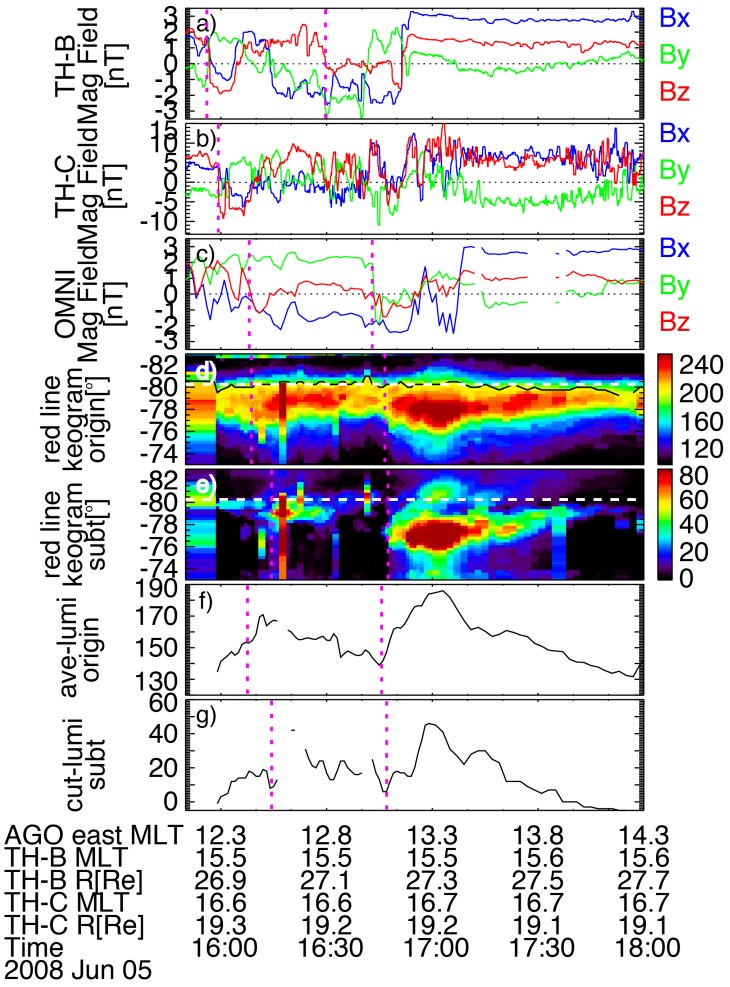

Figure 4.1 Time series of (a) magnetic field observed by THEMIS B, (b) magnetic field observed by THEMIS C, (c) OMNI IMF, (d) keogram made from red-line emission, (e) background-subtracted keogram made from red-line emission, (f) average luminosity from 73° to 84° south magnetic latitude using original keogram (Panel [d]), (g) the luminosity of background-subtracted keogram (Panel [e]) along the dashed line shown in Panel (e) on 5 June 2008. Magenta dashed lines in Panels (a-c) indicate southward turnings of the IMF and magenta dashed lines in the keograms show PMAFs. The solid line in Panel (d) shows the poleward boundary of auroral oval. The dashed lines in Panels (d) and (e) are chosen to present luminosity profile shown in Panel (g).

THEMIS B was at ~27 Re from the Earth and at ~15.5 MLT. Two substantial southward turnings occurred as indicated by magenta dashed lines. Considering propagation of the solar wind (~370 km/s), these two IMF southward turnings would reach the Earth's bow shock nose at ~1600 and ~1634 UT. The IMF at THEMIS B turned northward at 1652 UT, and then became steady northward. OMNI also detected two substantial southward turnings at ~1609 and ~1642 UT. Here the timings of IMF southward turning are identified by major sign changes of Bz for comparison with optical data, quantitative correlations being described below. During this period, the similarity between THEMIS Bz and OMNI indicates that the IMF Bz structures at the L1 point and the THEMIS B location are essentially the same. There are some differences in IMF By, however, particularly before the second southward turning.

The keogram shown in Figure 4.1d is from the eastern portion of the imager FOV at ~13 MLT. The dayside auroral oval is centered at ~-79° MLAT. To show variations clearly, we show a detrended keogram in Figure 4.1e, where the background is defined as an averaged luminosity at each pixel within ~1 h from each observation time. The black solid curve in Figure 4.1d presents the poleward-most contour of 200 intensity units as a proxy of the poleward boundary of the dayside auroral oval. The white dashed line is drawn 1 degree poleward of the equatorward-most magnetic latitude of the poleward auroral oval boundary in order to cut through PMAFs. Two brightenings occurred at ~1600 and ~1645 UT, indicated by two magenta dashed lines in Figure 4.1d. These were followed by small auroral structures that propagated poleward, identified at ~1614 UT and 1647 UT by magenta dashed lines in Figure 4.1e. While the first poleward propagation is faint, the second poleward propagation can be seen clearly up to ~-83° MLAT. These can be considered as PMAFs. These two PMAFs appeared within ~20 min after the two southward turnings of the IMF. The intensity of the dayside auroral oval decreased

without PMAFs after the northward turning. Although the IMF By at THEMIS B turned positive twice, PMAFs did not occur at the same time lag relative to the By turnings. The relatively good correspondence between the IMF Bz and PMAFs indicates that the southward turnings of the IMF may be associated with those PMAFs.

To quantify the correlation between IMF Bz and PMAFs, Figure 4.1f shows average luminosity of the original keogram between -73° and -84° MLAT at each time (hereinafter called "average-luminosity profile") and Figure 4.1g shows the luminosity along the white dashed line shown in the background subtracted keogram (hereinafter called "line-luminosity profile"). In this case, the white dashed line cuts at -80° MLAT. The average-luminosity profile primarily shows luminosity in the auroral oval, while the line-luminosity profile indicates PMAF intensity. These two line plots show the auroral oval brightenings that occurred soon after these two southward turnings of the IMF and were then followed by two PMAFs.

4.2.2 Second Event: 19 August, 2008

Figures 4.2a–4.2c show magnetic field data obtained from THEMIS B, THEMIS C, and OMNI, respectively, from 1150 to 1330 UT on 19 August 2008. The conjunction period on this day is from 1200 to 1330 UT. THEMIS B was ~28 RE from the Earth and at ~11.7 MLT, while THEMIS C was at ~11.6 MLT and ~19.4 RE from the Earth. In Figure 4.2a, three southward turnings are identified by THEMIS B at 1152, 1216, and 1246 UT (propagation time to the bow shock is ~3 min under the solar wind speed of ~560 km/s). Similarly, from Figure 4.2b, three southward turnings are also identified by THEMIS C at 1153, 1217, and 1248 UT (propagation time to the bow shock is ~1–2 min). In contrast, OMNI data show substantially different IMF variations. As shown in Figure 4.2c, the southward IMF at ~1200 UT lasted longer than

measured by THEMIS. The southward turning detected by THEMIS at ~1216–17 UT was not seen in OMNI, and the southward IMF starting at 1245 UT was much shorter. The differences between OMNI and THEMIS suggest that the IMF near the bow shock measured at THEMIS was different substantially from the IMF around the L1 point because of localized structures that missed the L1 point or time evolution of solar wind structures during their propagation.

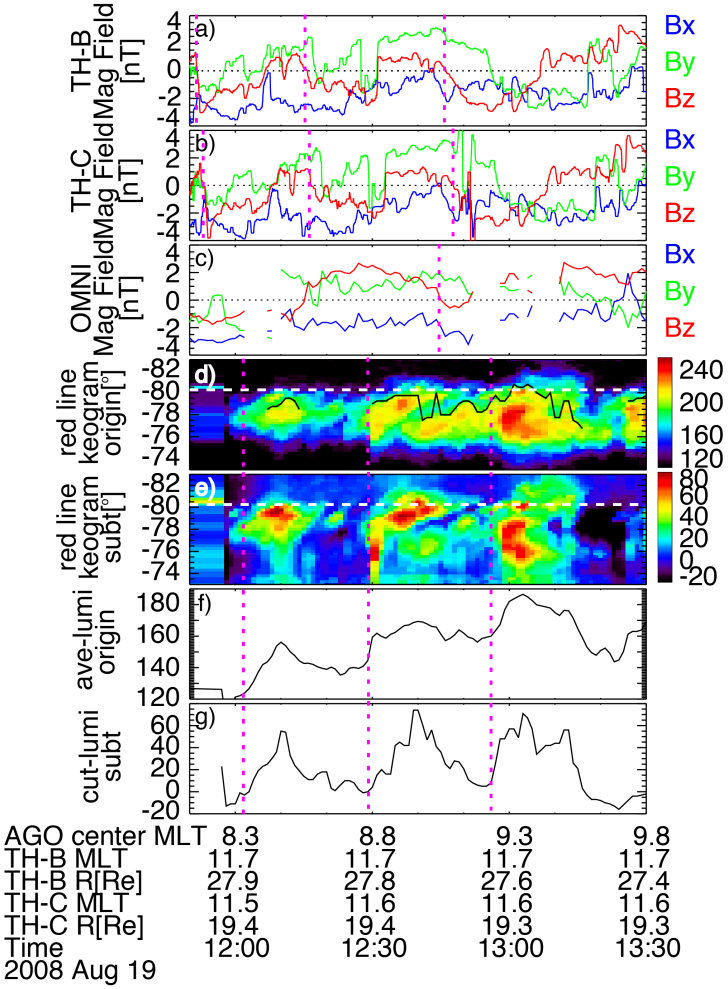

Figure 4.2 Same format as in Figure 4.1 but for the 19 August 2008 event.

Figures 4.2d and 4.2e present original and background-subtracted detrended keograms along the central meridian of the red-line imager data. The auroral oval brightened at 1200, 1228, and 1255 UT, and at almost the same time, the auroral structures propagated poleward (i.e.,

PMAFs). These three oval brightenings and PMAFs are observed a few minutes after the three IMF southward turnings identified by THEMIS B/C, respectively. These indicate the important role of IMF southward turnings in auroral oval brightening and the following poleward moving auroral structures.

However, the IMF Bz data obtained from OMNI is substantially different from that obtained from THEMIS B/C. Three PMAFs during this period were not correlated with IMF Bz by OMNI. Without THEMIS observation, those three PMAFs would be identified as "spontaneous" PMAFs. Thus, the IMF measurements at THEMIS near the bow shock are important for identifying the IMF Bz variations that triggered the PMAFs.

Additionally, although the IMF By also showed three small negative turnings, the timings relative to the PMAFs were not the same, giving lower correlations than the IMF Bz.

4.2.3 Third Event: 2 May, 2011

Figures 4.3a-4.3c show magnetic field data obtained from THEMIS B, THEMIS C, and OMNI, respectively, from 1410 to 1830 UT on 2 May, 2011. The conjunction period on this day is from 1410 to 1830 UT. THEMIS B was at ~11.2 MLT and ~52 RE from the Earth, while THEMIS C was at ~11.6 MLT and ~52 RE from the Earth. Three major southward turnings of the IMF are identified at 1428, 1513, and 1530 UT by THEMIS B (~6–7 min propagation time to the bow shock under the solar wind with speed of ~650 km/s). Similarly, in Figure 4.3b, we see three southward IMF turnings at 1416, 1517, and 1532 UT in THEMIS C data (~6–7 min propagation time). However, for the OMNI data shown in Figure 4.3c, only one major southward IMF turning is identified at 1442 UT. Note that the IMF in this period is highly fluctuating. The

timings mentioned above select representative southward turnings, and there exist many other rapid changes in IMF.

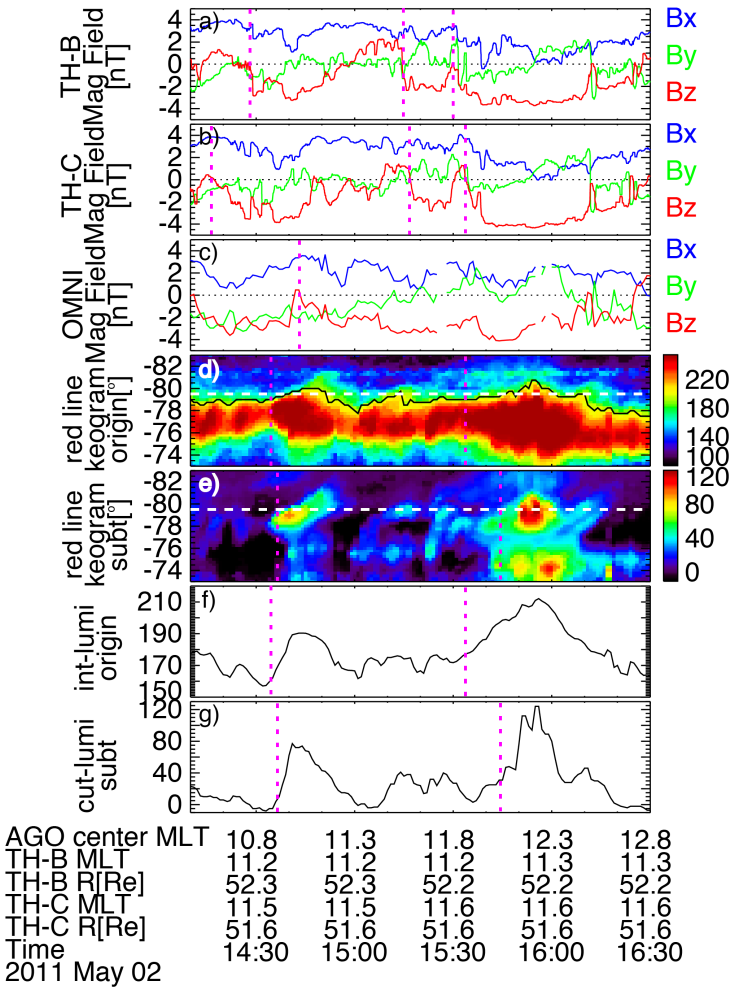

Figure 4.3 Same format as in Figure 4.1 except for the May 2, 2011 event.

The original (Figure 4.3d) and detrended (Figure 4.3e) keograms are obtained from the central meridian of the red-line imager data. A few minutes after the first and third major IMF southward turnings that were identified from the THEMIS B/C data, two major auroral oval brightenings are identified in the original keogram at 1433 and 1532 UT, and two PMAFs are identified soon afterward as indicated at 1435 and 1543 UT by the magenta dashed line in Figure 4.3e. The corresponding response time is within 20 min (including ~6–7 min propagating time).

There was also a weaker brightening and weaker PMAF after the second southward turning, but these were not large enough to stand out in Figures 4.3f and 4.3g. The IMF By did not show consistent changes around the brightening times. The correspondence between the IMF at THEMIS and PMAFs indicates that the southward turnings are responsible for triggering the auroral brightenings and subsequent PMAFs. Although the southward IMF turning identified in the OMNI data and the southward IMF enhancement at 1534 UT may explain the first and the last PMAFs, OMNI missed the second southward turning of the IMF. This also emphasizes the importance of having solar wind measurements near the bow shock in order to detect solar wind structures that may have not reached other solar wind monitors.

4.2.4 Fourth Event: 26 June 2008

Figures 4.4a and 4.4b show magnetic field data obtained from OMNI and THEMIS C, respectively, from 1720 to 2000 UT on 26 June 2008. THEMIS C was at ~14 MLT and at ~15 RE from the Earth. Four southward turnings are identified at 1729, 1811, 1927, and ~1945 UT by THEMIS C, and three southward turnings are identified at 1729, 1810, and 1942 UT by OMNI data.

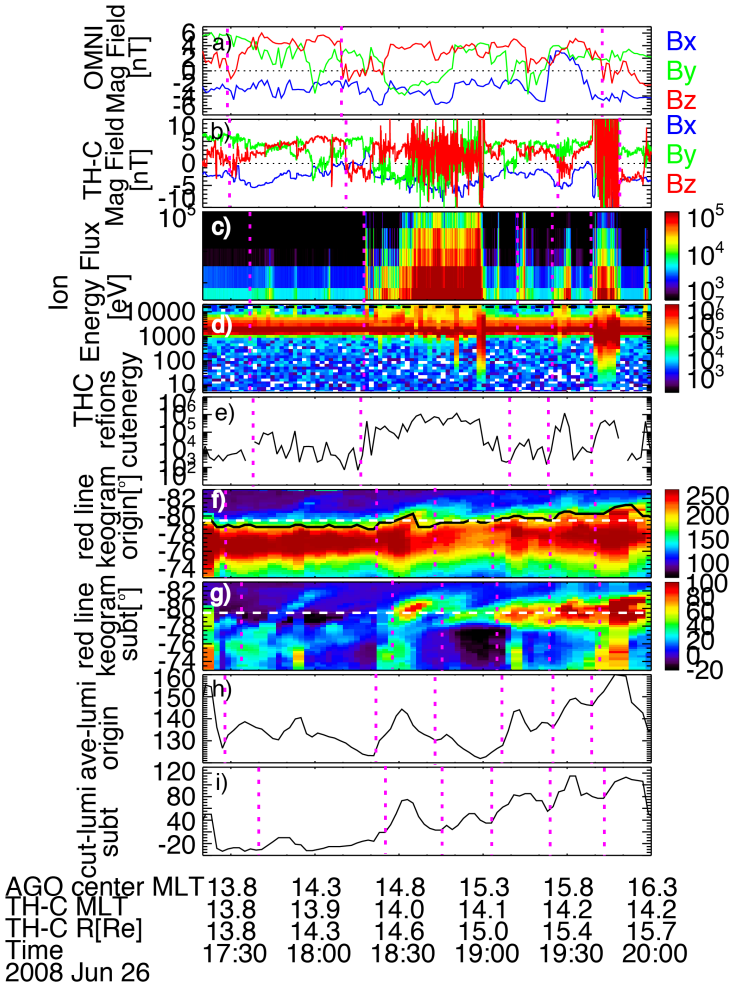

Figure 4.4 Time series of (a-b) magnetic field obtained from OMNI and observed by THEMIS C; (c-d) energy flux of ions observed by THEMIS C; (e) ion flux at 6918 eV (shown by the dashed line in panel (d); (f) keogram made from red emission; (g) background subtracted keogram made from red emission; (h) average luminosity of original keogram (panel [f]) from 73° to 84° south magnetic latitude; (i) the luminosity of background subtracted keogram (panel [g]) at the dashed line shown in panel (g) on June 26, 2008. The solid curved line in panel f shows the poleward boundary of auroral oval. The dashed lines in panels f and g are chosen to present luminosity profile shown in (i). Magenta dashed lines in panel (b) show southward turnings observed by THEMIS C. Magenta dashed lines in panel (c) show reflected ions. Magenta dashed lines in panel (g) show PMAFs.

We also show ion energy fluxes with energy channels from 5 eV to 100 keV in Figures 4.4c and 4.4d. Five major foreshock ion events are identified at 1740, 1818, 1912, 1925, and 1940 UT. They are associated with suprathermal ions in the foreshock region and during two

strong foreshock ion events (the second and the last ones), the magnetic field in the foreshock became strongly fluctuating.

Figures 4.4f and 4.4g present the original and detrended keograms obtained from the central meridian of the red-line imager data. Six auroral brightenings and subsequent PMAFs are identified at 1733, 1828, 1845, 1903, 1925, and 1945 UT during the brightening of auroral oval, indicated by magenta dashed lines in Figure 4.4g. Unlike the three periods shown above, only three PMAFs that were identified during this period followed substantial IMF southward turnings. In contrast, all the five foreshock ion events are observed within 9 min of each PMAF. Here the second and the third PMAFs are both during the second ion event, which is the largest one of those five ions events. Although both IMF southward turnings and ion events are observed in conjunction with three out of those five PMAFs, the other two PMAFs are observed in conjunction with ion events. That indicates the possible connection between foreshock disturbances and PMAFs.

However, we found that the foreshock ion events that were identified during the first (5 June 2008) and second (10 August 2008) periods are uncorrelated with PMAFs occurrence, and foreshock ion events cannot be observed during the third (2 May 2011) period because the satellites were out of the foreshock region on this day.

4.3 Superposed Epoch Analysis Results

The case study indicates the important role of IMF southward turnings in triggering PMAFs and the response time of PMAFs to those IMF southward turnings is about 8 min. To investigate how IMF southward turnings contribute to triggering PMAFs and to obtain the general response time, we searched the data during 2008, 2009, and 2011 and identified 60

PMAFs that satisfy the criteria mentioned in section 4.1. The events are listed in Table 4.1. The first column of Table 4.1 shows the onset times of the identified PMAFs; the second column shows the maximum luminosity increases of the PMAFs relative to the background luminosity; the third column shows the lifetimes of those PMAFs.

Table 4.1 All PMAFs Observed and Selected Based on the Images of AGO ASI Imagers During 2008, 2009, and 2011[a]

PMAF Onset Time[b]	**Maximum Luminosity Increase (lumi units)**	**PMAF Lifetime (min)**
2008/5/28; 17:20	31	12
2008/5/28; 18:26	26	6
2008/6/1; 18:34	20	6
2008/6/1; 20:02	33	6
2008/6/5; 16:14	28	5
2008/6/5; 16:46	29	7
2008/6/25; 16:21	77	11
2008/6/25; 17:26	54	16
2008/6/25; 18:05	93	6
2008/6/26; 18:21	79	90
2008/6/26; 18:50	82	46
2008/6/28; 14:50	36	5
2008/6/28; 15:37	65	16
2008/6/28; 16:26	49	14
2008/6/29; 14:40	76	11
2008/6/29; 17:09	49	68
2008/6/29; 17:40	29	6
2008/7/2; 16:45	40	5

PMAF Onset Time[b]	Maximum Luminosity Increase (lumi units)	PMAF Lifetime (min)
2008/7/2; 18:44	68	14
2008/7/3; 14:42	44	6
2008/7/3; 16:49	68	6
2008/7/3; 18:30	51	8
2008/7/3; 19:20	46	6
2008/7/4; 13:07	49	8
2008/7/4; 13:32	54	20
2008/7/23; 15:36	20	13
2008/7/23; 16:08	74	37
2008/7/23; 16:56	8	26
2008/7/23; 17:41	68	34
2008/7/23; 18:49	123	88
2008/7/24; 16:20	99	47
2008/7/26; 12:34	52	8
2008/7/26; 14:07	47	15
2008/7/27; 14:38	50	11
2008/7/27; 15:36	79	5
2008/7/27; 16:29	47	10
2008/7/27; 17:47	59	30
2008/7/28; 15:31	71	28
2008/7/28; 16:45	78	39
2008/7/29; 11:55	67	54
2008/7/29; 13:42	54	11
2008/7/29; 15:34	18	32
2008/7/29; 17:29	92	92

PMAF Onset Time[b]	Maximum Luminosity Increase (lumi units)	PMAF Lifetime (min)
2008/8/19; 11:59	68	17
2008/8/19; 12:28	60	10
2008/8/19; 12:56	43	6
2008/8/22;,11:50	91	51
2008/8/22; 12:22	41	18
2008/8/26; 15:03	63	108
2008/9/2; 12:14	84	23
2009/6/24; 18:41	118	6
2011/5/2; 14:35	72	15
2011/5/2; 15:49	99	10
2011/5/4/; 13:52	42	7
2011/5/4; 16:45	84	23
2011/5/4; 19:25	73	6
2011/6/2; 13:44	24	7
2011/6/2; 14:38	40	12
2011/6/2; 17:09	32	8
2011/6/2; 17:49	27	10

- **a** The first column shows the onset time of the selected PMAFs. The second column shows the maximum luminosity increases of the PMAFs from the background luminosity. The third column shows the lifetime of the selected PMAFs. Here the luminosity values are from line luminosity profile.
- **b** Dates are formatted as year/month/day; Hour: Minute.

The method to obtain the PMAF intensity is the same as that in Figure 4.1g except that the background level is defined as an average of the luminosity over 20 min before the onset time of a PMAF to ensure that selected PMAFs are isolated from preceding activity. As mentioned in section 4.1, we required that the intensity should increase by more than 20 intensity units and last for more than 5 min. For superposing events with different IMF Bz or auroral intensity before PMAFs, we subtracted the median IMF Bz and luminosity values from 15 to 20 min before PMAF onset. The IMF Bz observed at THEMIS is shifted to the bow shock using the measured solar wind speed.

Figure 4.5a shows superposed epoch analysis of PMAF intensity. Figures 4.5b-4.5d show superposed epoch analyses of IMF ΔBz calculated from the IMF Bz data obtained from THEMIS B, THEMIS C, and OMNI, respectively. Zero epoch time is also the onset time of each PMAF. The color, dashed lines, and solid lines show constant percentiles.

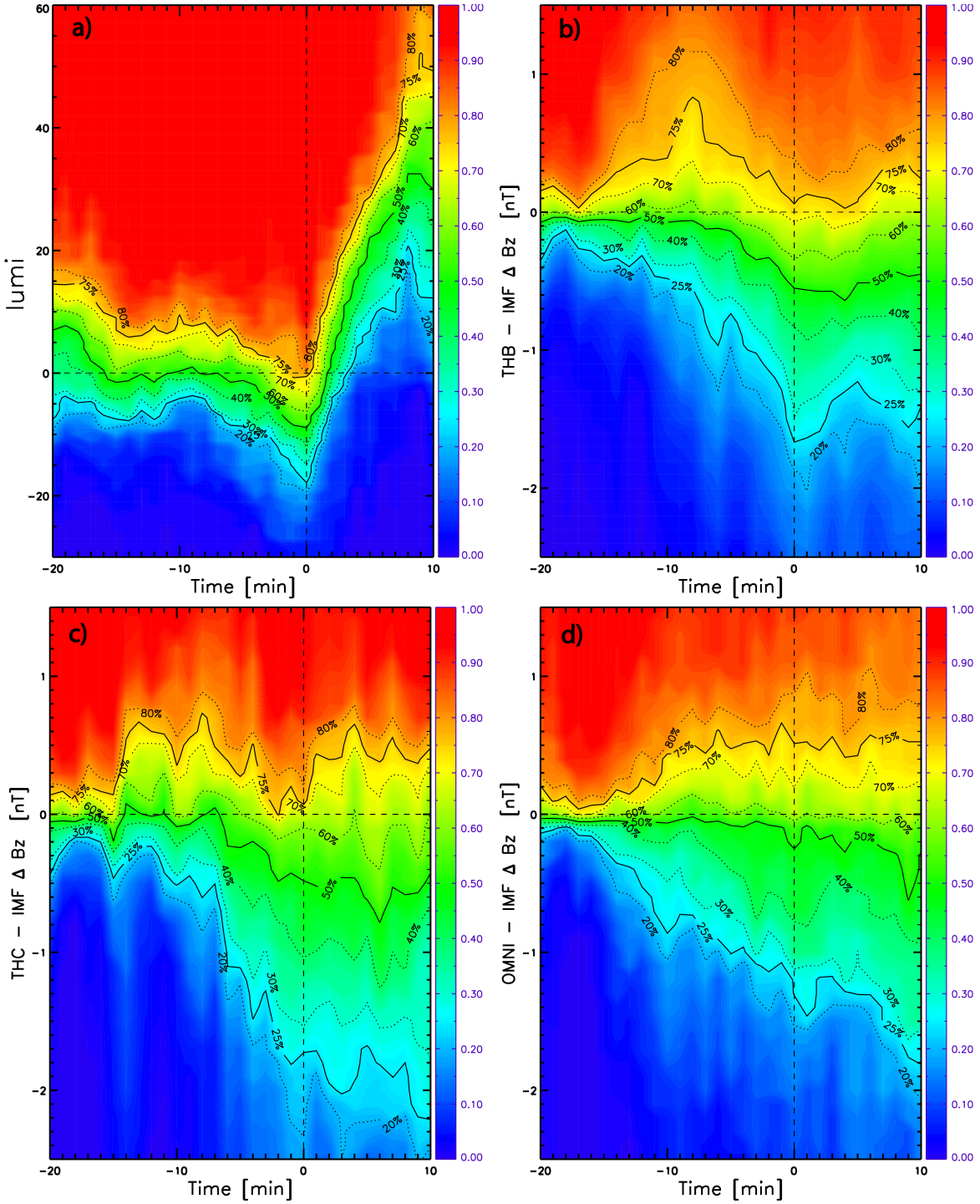

Figure 4.5 Superposed epoch analyses of ΔBz calculated from IMF Bz obtained from (a) THEMIS B, (b) THEMIS C, and (c) OMNI. The zero epoch times are PMAF onset times that are shown in Table 4.1. The color, dashed, and solid lines show the percentages of total cases.

Figure 4.5a shows that intensities of all the PMAFs increase over 20 luminosity units after the onset time and last for more than 5 min, satisfying the criteria of selecting PMAFs described in section 4.1.

In Figures 4.5b and 4.5c, superposed epoch analyses of IMF ΔBz obtained from THEMIS B and C both show that almost all events show a decreasing trend of the IMF Bz after ~ -8 min. For THEMIS B, ~70% of events show a reduction of the IMF Bz relative to the reference level (Bz at -20 to -15 min). For THEMIS C, ~65% of events show a reduction of the Bz. The Bz reduction started ~8 min before the PMAF onset time.

On the other hand, in Figure 4.5d, the superposed epoch analysis of IMF ΔBz obtained from OMNI shows that the Bz reduction magnitude was smaller and seen in a slightly smaller percentage of events (~60%) than in THEMIS B or C. If we limit to times before the PMAF onset times (~ -8 to 0 min), only ~40% of cases have a reduction of IMF Bz, and a magnitude of Bz reduction comparable to the median lines in THEMIS B and C was only seen in ~40% of events.

Such differences in percentages between THEMIS and L1 measurements (OMNI) indicates that the IMF far away from the bow shock could be quite different from the IMF near the bow shock. If a solar wind monitor is far from the bow shock, the satellite may miss IMF changes that trigger PMAFs, and those PMAFs would be classified as spontaneous events. Thus, it is important to have a solar wind monitor near the bow shock for examining IMF trigger of PMAFs. Based on our analysis, at least 10% more PMAFs would be classified as associated with IMF southward turnings by using THEMIS B/C than by using the OMNI data.

Besides the superposed epoch analyses, we also evaluated each case and listed correlating parameters in the last column of Table 4.1. Out of the 60 PMAFs, 40 cases (67%) of PMAFs

occurred within 15 min after IMF southward turning. Those cases are marked as "ΔBz" in Table 4.1. In the cases without IMF southward turnings over 15 min before PMAF onset, we found one case occurring during a substorm, three cases By dominated, five cases Bx dominated, three cases with Parker spiral IMF, and two cases with Ortho-Parker IMF. Although those are also not likely to be major processes for triggering PMAFs, this indicates that processes other than IMF Bz turnings may have minor contributions to triggering PMAF. Although we have also looked at dynamic pressure data, none of our events are correlated with dynamic pressure changes. Thus, the correlation between PMAFs and dynamic pressure changes found by [*Mende et al*., 2009a] may be a minor contribution when considering them in the context of a statistical database.

4.4 Discussion and Conclusion

To examine how often solar wind parameter changes play a role in triggering PMAFs, we compared aurora and solar wind measurements from the AGO AP1 imager and THEMIS. Case studies show that PMAFs occurred soon after brightening of the dayside auroral oval. Moreover, based on 60 conjunction cases in 2008, 2009, and 2011, the superposed epoch analysis shows that ~70% of events are preceded by IMF southward turnings by ~8 min, indicating their important role in triggering PMAFs. We also found that the superposed epoch analysis of the IMF Bz obtained from OMNI data shows that only 40% of PMAFs onsets occur ~8 min after IMF southward turnings. This indicates that the measurements at the L1 point may miss small-scale structures that reached the subsolar bow shock or that the solar wind may evolve between the two measurements. If we compare the OMNI solar wind and PMAFs, those cases would indicate spontaneous PMAFs without correlation with solar wind changes. However, the THEMIS measurements, closer to the bow shock, show that PMAFs are associated with IMF

southward turnings. Thus, measurements near the bow shock are critically important for evaluating the trigger of PMAFs.

With the advantages of THEMIS B/C being close to the bow shock, we also examined correlations between foreshock phenomena and PMAFs. One PMAF in 26 June 2008 and two PMAFs in 28 July 2008, which did not follow substantial IMF southward turnings, were found in correlation with foreshock ion events, indicating that foreshock disturbances may be a contributor but not a major one to trigger PMAFs. However, the small number may be because the satellites are not close enough to foreshock regions, a possibility that warrants further evaluation.

Among the other cases, three are dominated by steady IMF By. Such an IMF condition is known to be related to pulsed flows around the cusp [*Moen et al.*, 2012] and may indicate that spontaneously activated, pulsed reconnection may be responsible for PMAFs during such an IMF polarity. We also found five cases with Bx domination, three cases with Parker spiral IMF, two cases with Ortho-Parker spiral cases, and one case that occurred during substorms. In Bx- and By-dominated cases, bow shock instabilities may evolve in the quasi-parallel foreshock region and may create additional disturbances that do not exist in the solar wind. This may also be the case for the events showing a correlation with foreshock ions. IMF By turnings and dynamic pressure changes do not appear to play a dominant role in triggering PMAFs.

CHAPTER 5

The evolution of PMAFs as dayside polar cap airglow patches with flow channels

In this chapter, the evolution of PMAFs as polar cap airglow patches are examined. Moreover, the relation between airglow patches and meso-scale fast flow channels in the dayside polar cap are evaluated. Section 5.1 presents the criteria to select the events for this study; Section 5.2 shows two cases with airglow patches and one case over quiet polar cap as a comparison; Section 5.3 presents the statistical analysis; and a summary is shown in Section 5.4.

5.1 Criteria and data set

While radar backscatter echo regions are generally not sufficiently large to investigate flow structures around polar cap patches (including the events in our studies), low-altitude satellite observations can provide both density and velocity over a wider region along their trajectories, and their conjunctions with imagers occur routinely, allowing us to perform a statistical study of airglow patches and related flow structures in the dayside polar cap. In this study, the conjunction between ASI at the AGO P1 station and DMSP satellites (F15, F16, F17 and F18) will be utilized.

Due the trajectories of DMSP satellites, most conjunctions with the imager at the AGO P1 station occurred during ~11:00 through 18:00 UT, which corresponds to the dawn to post-noon regions (~07:00 to 14:00 MLT). We have surveyed the southern winter months (from

April to September) during 2007–2011. We focused on dark and clear sky conditions and large patches that lasted for at least 10 min inside the FOV of ASI images during ~1030 to 2130 UT (~0600 to 1800 MLT) when the ASI FOV covers a broad area over the dayside polar cap. Airglow patches were identified in red-line emission as >~15 intensity units above background (surrounding intensity) with no substantial blue-line emission. From a comparison to DMSP density data, this intensity threshold corresponds roughly to a factor of 2 increase in density at the DMSP altitude. To identify polar cap flow structures around airglow patches, we required that the satellites fly over the patches identified in the ASI data within ±6 h MLT from magnetic noon. Since we only use the cross-track velocity component, we required the angle between the track of the airglow patch and the track of the corresponding DMSP satellite to be between 40° and 130° for measuring the dominant velocity component. Based on these criteria, we obtained 50 cases for analysis during the southern winter seasons of 2007–2011, the conjunctions being primarily in the pre-noon sector due to the MLT of the satellite orbit.

5.2 Case study

5.2.1 First Event: June 10, 2008

The first two rows of Figure 5.1 present a case on June 10, 2008. The auroral oval lies at ~−75°-−80° magnetic latitude (MLAT). While the red-line emission detects both aurora and airglow patches, the poleward boundary of the auroral oval can be identified as the poleward-most blue-line emission as visually traced by magenta lines in the blue-line emission snapshots (the left half of the blue-line emission images are contaminated by artificial light). Those lines are also drawn in the red-line emission snapshots at the corresponding times. While much of the red-line emission is equatorward of the magenta lines, meaning auroral emission, the top right

portion of the red-line emission within the blue-line image FOV can be seen to extend 3-4° poleward, indicating that this emission is polar cap patches. DMSP 15 crossed this region as shown by the blue arrow.

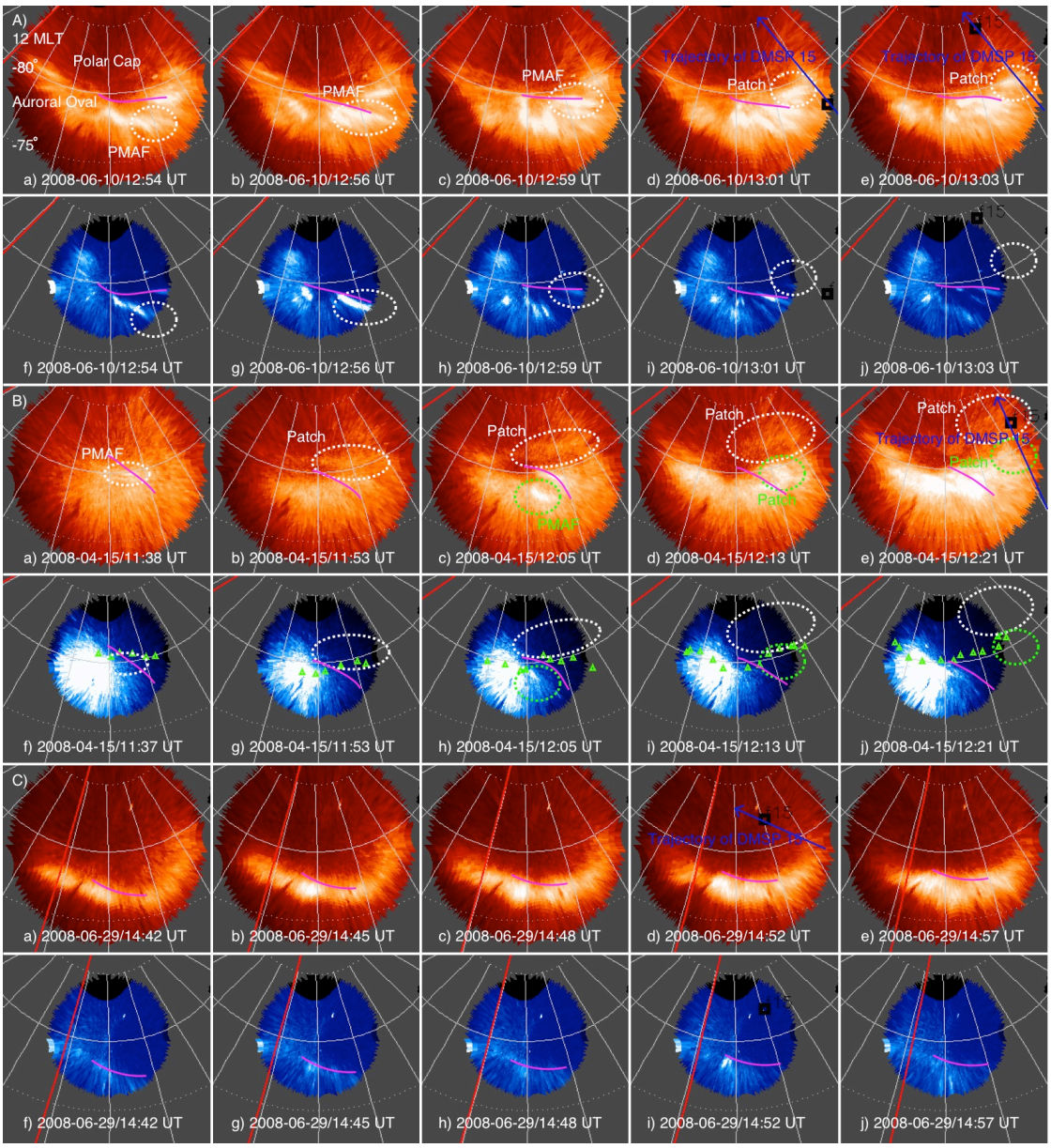

Figure 5.1 Snapshots of ASI data at AP1 on (Aa-Aj) June 10, 2008, (Ba-Bj) April 15, 2008, and (Ca-Cj) June 29, 2008. Snapshots in red and blue are in red- and blue-line emissions, respectively. Magenta curves indicate the poleward auroral oval boundary. The dashed circles highlight the PMAFs and airglow patches that we focus on and the black squares show the footprints of DMSP satellites, of which trajectories are indicated by blue arrows. The red line marks the magnetic noon meridian.

The optical emissions were not steady but included anti-sunward propagation. This optical sequence started with a new auroral brightening within the imager FOV at ~8 MLT and ~12:54 UT (Figure 5.1Aa and 5.1Af, white dashed circle). This can be identified as a PMAF because both wavelengths detected the formation and slight poleward propagation of this structure within the auroral oval. This PMAF also propagated azimuthally away from noon (Figures 5.1Ab and 5.1Ag), and was observed in blue-line emission clearly until it faded after 13:00 UT. In contrast, the red-line emission images showed this emission to propagate further poleward and azimuthally. When DMSP 15 entered AP1's FOV, no discernible blue-line emission was detected over a large portion of this structure as seen in red-line emission (Figure 5.1Ad and 5.1Ai). Thus, this optical sequence can be interpreted as the PMAF evolving to a polar cap airglow patch that propagated mainly along the auroral poleward boundary without detaching from it. This red-line luminosity is not due to low-energy precipitation but high-density plasma, because, as shown by the DMSP data in Figures 5.2c and e, a distinct plasma density enhancement was seen without substantial electron precipitation.

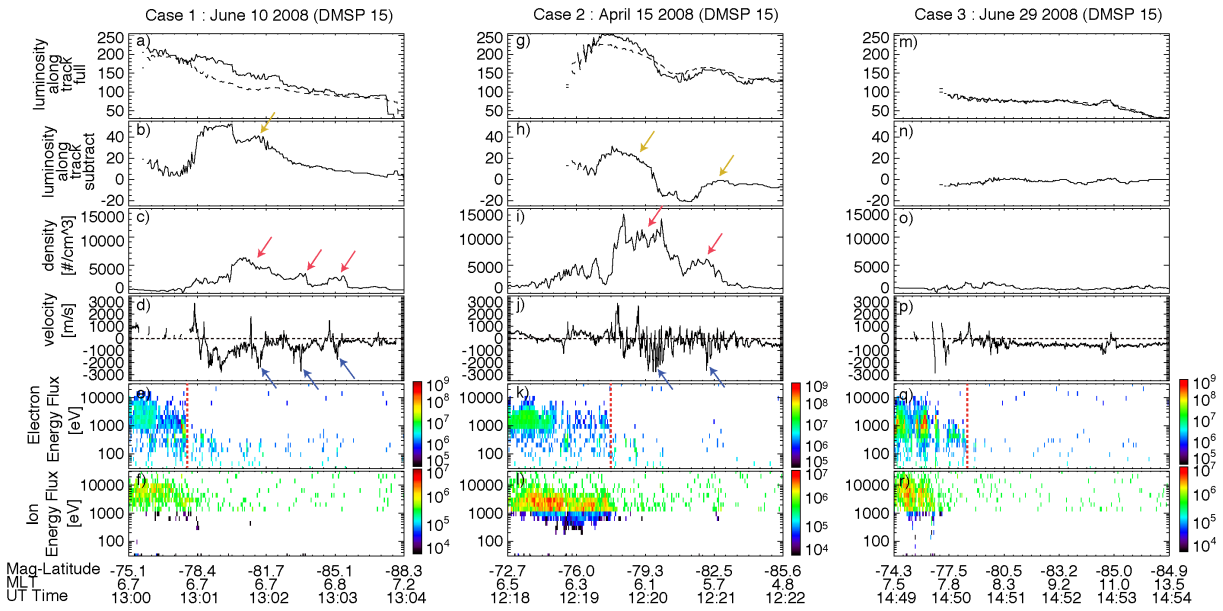

Figure 5.2 Time series of a luminosity of ASI images along DMSP track, b luminosity of ASI images along DMSP track subtracting the background luminosity, c plasma density, d cross-track velocity, e electron energy flux and f ion energy flux by DMSP 15 for Figure 5.1Aa–Aj event. g-i and m-r, which also show the data from DMSP 15, are given in the same format as a-f for Figure 5.1Ba-Bj event and Figure 5.1Ca-Cj events, respectively

The left column of Figure 5.2 displays, from top to bottom, the optical luminosity along the satellite's track (both the original and after background subtraction), and the density, velocity, electron energy flux, and ion energy flux measured by DMSP 15 around the time of the conjunction with AP1 for the June 10, 2008 case. The background-subtracted data in Figure 5.2b shows two enhanced luminosity regions, although the second peak is not clearly seen in the Figure 5.1Ae snapshot. The poleward boundary of electron precipitation in Figure 5.2e is seen at ~1300:50 UT based on a sharp drop of electron fluxes at several hundred eV, and this latitude (~−78°) is consistent with the boundary location identified in the blue-line emission shown in Figure 5.1A. The luminosity enhancement at ~1300:50-1302:10 UT is not associated with significant electron precipitation but coincides with an electron density enhancement in Figure

5.2c. This indicates that the red emission intensity enhancement within the polar cap region just poleward of the auroral oval corresponds to airglow patches.

Interestingly, the horizontal cross-track plasma velocity (Figure 5.2d, positive sunward) showed remarkable anti-sunward flow bursts localized around the peaks of the enhanced density (~600 km width along the track). Since DMSP 15 passed over the optical airglow patch at ~1300:50-1302:10 UT almost perpendicular to the azimuthal patch propagation direction, measured velocities are approximately along the propagation direction. The maximum anti-sunward velocity reached ~2800 m/s, and this is almost an order of magnitude larger than the large-scale background flow seen deep in the polar cap later in this time interval (~300 m/s). At the same time, fast sunward flows (>1000 m/s) are also identified at 1300:50, 1301:47 and 1302:55 UT. Although these sunward flows are much more localized than anti-sunward fast flows, they and the large anti-sunward flows around indicate the large flow shears in this flow pattern. The optical sequence of the azimuthal motion of the detectable airglow patch suggests that the enhanced density and flow bursts are spatial structures moving anti-sunward rather than temporal variations.

5.2.2 Second Event: Aril 15, 2008

Similar to the previous case, much of the red-line emission of the April 15, 2008 (Figure 5.1B) case is found at ~−75°-−80° MLAT. Similarly, as Figure 5.1Af-5.1Aj, the magenta lines in Figure 5.1Bf-5.1Bj also indicate dayside auroral oval boundary based on the blue-line emissions. Since no blue-line emission was found above these lines, the red-line emission poleward of this can be identified as airglow emission. There are more than one auroral/airglow structures moving azimuthally and poleward. Two of those are marked by the white and green

dashed circles. In both red (Figure 5.1Ba) and blue (Figure 5.1Bf) emission snapshots, a brightening structure with poleward and azimuthal motion, highlighted by white dashed circles, is identified at ~1138 UT at 7.5 MLT both in red and blue wavelengths, indicating that initially this is a PMAF in the dayside auroral oval. This PMAF shows a large azimuthal propagation in addition to poleward propagation and then evolves into a polar cap airglow patch, since there is no enhanced intensity inside the white dashed circle in subsequent blue emission snapshots in Figure 5.1Bg-5.1Bj. Another similar sequence started at 1205 UT. These events indicate that PMAFs can occur quite far away from noon and involve substantial azimuthal motion before connecting to polar cap patches.

DMSP 15 crossed these two airglow patches at ~1220 UT (green dashed circle) and ~1221 UT (white dashed circle). Much of the luminosity enhancements in Figure 5.2h is poleward of the electron precipitation boundary marked in Figure 5.2k, confirming that these optical structures are polar cap airglow patches. The first enhancement of optical intensity at 1220 UT shown in Figure 5.2g-h indicates the airglow patch that we identified in Figure 5.1B by green dashed circles. Figure 5.2i shows the first density enhancement to be rough association with this airglow patch. Within this significant enhancement of density, narrow anti-sunward flows (Figure 5.2j) are identified. The maximum velocity of anti-sunward flow is ~2800 m/s, which is much faster than the large-scale background velocity of ~500 m/s that can be seen toward the end of this time interval. There is also a fast sunward flow (>1000 m/s) that is identified at 1219:55 UT near the anti-sunward flow. This indicates a large anti-sunward flow shear in this flow pattern although the sunward flow is much more localized than the anti-sunward flow.

The second enhancement of optical intensity at 1221 UT shown in Figure 5.2g-h indicates the airglow patch that we identified in Figure 5.1B by white dashed circles. DMSP 15 crosses this airglow patch at ~5.8 MLT, which is slightly out of our criterion for MLT of conjunction (6-18 MLT), thus this airglow patch is not included in our conjunction database. Even though, it evolved similarly to the first PMAF and patch, and was later measured by DMSP adjacent to the first airglow patch. The density of this airglow patch (Figure 5.2i) reaches to ~6100 #/cm^3, which is much larger than the background density after this density enhancement (~1000 #/cm^3). At the same time, a narrow anti-sunward flow with similar size to that of the airglow patch is identified. The maximum velocity of this flow is ~2600 m/s, which is much faster than the background anti-sunward flow (~600 m/s in this case). The satellite track is almost perpendicular to the patch propagation direction, and thus the cross-track velocity detects the major component of the flow channel. This indicates that this flow channel structure is collocated with the airglow patch.

5.2.3 Third Event: June 29, 2008

In previous two cases, dayside airglow patches are found to be associated with localized fast anti-sunward flows. To show that the fast flows are associated with the airglow patches, we here show a case during a quiet time without airglow patches (June 29, 2008).

The red-line emission is confined to ~–75° to 80° MLAT, and unlike in the previous two cases, no substantial red-line emission is found poleward of the blue-line emission, at least within the meridians where the blue-line poleward boundary can be seen. DMSP 15 crossed the FOV of red emission images from 1451 to 1454 UT. During the conjunction period, the luminosity along the trajectory of DMSP 15 is much less than in the previous two cases (Figure

5.2m). Correspondingly, Figure 5.2o shows ~1000 #/cm3 plasma density without significant enhancements. At the same time, the velocity of the anti-sunward flow pattern in this case is ~600 m/s throughout the conjunction period in the polar cap (except for short-lasting disturbances with a peak velocity of ~1000 m/s). Such slower and wider flow is generally known as large-scale two-cell convection, which is relatively steady and uniform during the quiet condition of polar cap.

5.3 Statistical study

We identified 50 conjunctions between polar cap airglow patches and DMSP satellites. In these cases, we compared the poleward boundary identified in the blue-line emission and DMSP precipitation boundary. At least along the satellite trajectories, those boundaries agree with each other better than the boundary identified in the red-line emission. Based on those identified boundaries, PMAFs are observed to propagate inside the auroral oval and then evolve to airglow patches in the polar cap.

From the identified 50 conjunctions between airglow patches and DMSP satellites, mesoscale flow enhancements in the vicinity of airglow patches were found in 45 cases. The flow enhancements were defined as enhancements with a peak at least 500 m/s larger than the flows in the surrounding region and a flow channel width less than 1000 km, which is typical size of background polar cap convection pattern. We used these 45 cases to obtain statistical properties of polar cap airglow patches and related fast flows. The airglow patches for the 5 cases without localized fast flows were nearly stationary at the conjunction times, consistent with the lack of fast flows. It is possible that these few patches were carried into the polar cap by fast

flows that dissipated prior to the satellite conjunction; however, this possibility cannot be tested with the present data set.

5.3.1 Quantifying patch and flow channel properties

To quantitatively characterize the 45 cases that we found, we determined density and flow structures by calculating the maximum magnitude and widths around conjunction periods. Figures 5.3a and 5.3b illustrate how those calculations were performed. The vertical lines in Figure 5.3a indicates the time period of the conjunction of the optical patch identified in the Figure 5.1Be. The density and velocity maxima within this time period are identified by the red dots. We only consider the conjunction time periods to avoid including density enhancements associated with other patches that cannot be seen clearly in the images due possibly to their weaker airglow emissions and imager spatial resolution. The minimum density and anti-sunward velocity magnitude are identified during the interval from 2 minutes before to 2 minutes after the conjunction period. Those values are drawn as blue horizontal lines in Figures 5.3a and 5.3b. We consider these minimum values as background density and velocity. The red lines mark $(A_{max} - A_{min})/e + A_{min}$, where A denotes the density and velocity magnitude and e is the Euler's number. While the red lines cross the data points more than twice, we use the distance between the first and last crossing points during the conjunction period as in Figure 5.3a and define this distance as the width of density. Similarly, we use the distance between the first and last points within the interval from 2 min before to 2 min after the conjunction period and define this distance as the width of the anti-sunward velocity enhancement. The two-minute longer window is used to ensure that flow enhancements wider than the density enhancements can be identified

appropriately. If no flow channel exists, the width will be the size of the whole-time window (a few thousand km).

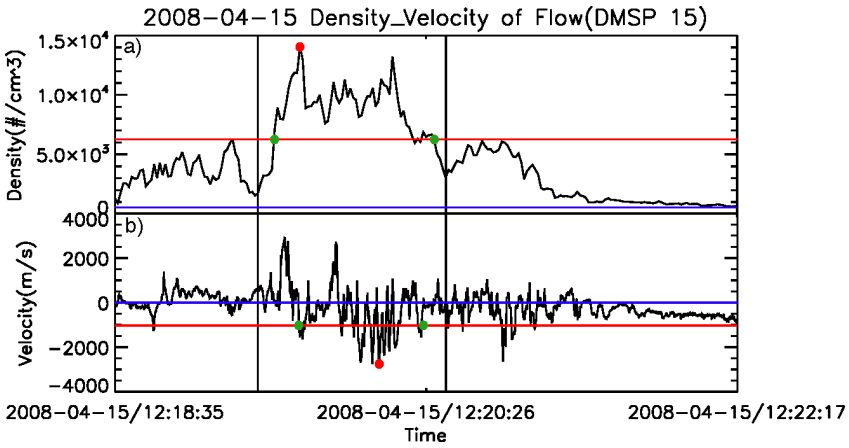

Figure 5.3 Panels (a) and (b) are blowups of Figure 5.2i and j. The red- and green points indicate the maximum density/velocity and the threshold values (see text) of density/velocity enhancements, respectively. The blue and red lines show background density/velocity and threshold values of density/velocity enhancements, respectively.

Our choice of e results from a trial of several different values. Our width definition somewhat differs from that by *Coley & Heelis*, [1995], who identified density widths as two edges in which the plasma density is enhanced above 40% in 140 km, and the overall enhancement is larger than 100% above the background. When a density enhancement only has a single peak, we checked that the edges obtained by our method and Coley and Heelis's method give essentially the same result. However, in cases where the enhanced density has multiple peaks, multiple sharp slopes meet their criteria, and hence, it becomes difficult to uniquely define density widths. Thus, our method can quantitatively find two edges that characterize density enhancements, and we confirmed the calculated widths by comparing to optical patch sizes from the AGO image data.

5.3.2 IMF By and Bz dependence

To find IMF conditions during our events, we took the median value of the OMNI 1-min resolution IMF data from 20 min before until the time of PMAF occurrence. Here, the 20-min threshold considers the timescale to change the large-scale current system in response to IMF variations [Anderson et al. 2014]. This averaging removes short-lasting fluctuations and gives median IMF conditions that are expected to affect large-scale convection during our events. In this subsection, we removed 3 of the 45 cases because we cannot identify their corresponding PMAF within the FOV of images and another 2 cases without OMNI 1-min resolution IMF data, and thus, we investigated IMF dependence of airglow patches and related fast flows based on 40 cases. While most cases have steady IMF conditions during the 20-min IMF averaging period, three cases have IMF Bz sign changes of more than ±1 nT and thus these cases may involve large changes in background convection. Here, the threshold is based on the earlier study by [*Drury et al.*, 2003]. These cases are marked in red when they appear in the panels of Figure 5.4.

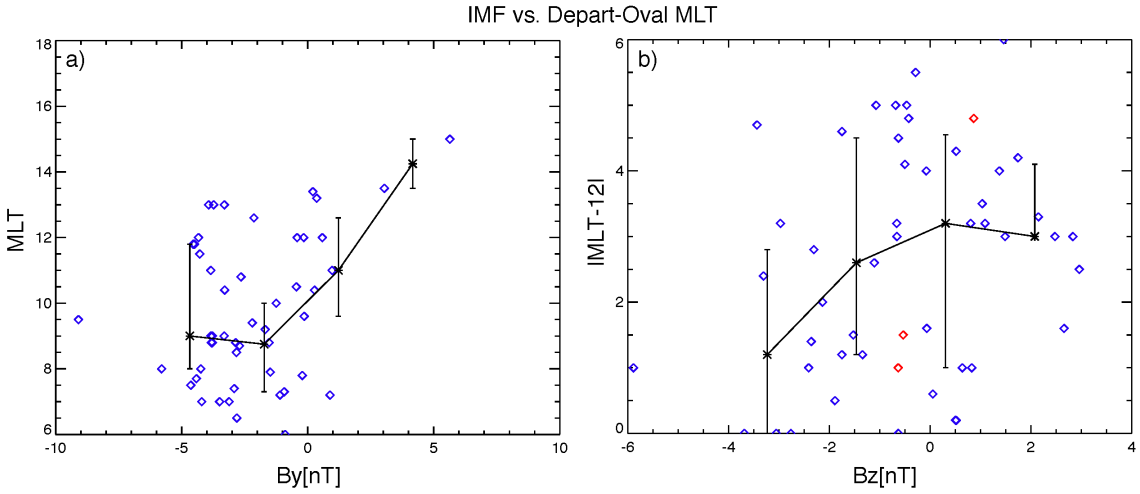

Figure 5.4 IMF Bz and By dependence of depart-oval MLT is shown by a and b. The black stars and error bars indicate the medians and upper and lower quartiles every 1.4 nT. Blue and red diamonds represent cases with stable and fluctuating IMF Bz condition, respectively.

Figure 5.4a and b shows the IMF By and Bz dependence of the MLT when patches depart from the poleward boundary of the auroral oval (hereinafter we call it depart-oval MLT). Here, we use |MLT−12| hours as the y-axis value of Figure 5.4b, presenting the MLT separation between the patch departures from the poleward boundary of the auroral oval and magnetic noon. Plotted in black are the median and upper and lower quartiles every 1.4 nT. Here, the 1.4-nT number is obtained by splitting the Bz range into four segments, which gives more than three data points in each segment. Despite other limited number of events and the relatively large error bars, the figures give trends of the parameters shown.

Figure 5.4a shows the IMF By dependence of depart-oval MLT. Although the data points in Figure 5.4a are scattered, the patches tend to depart to the polar cap on the dawnside when the IMF By is negative and on the duskside when the IMF By is positive. There is also evidence for a trend for patches to depart further toward the dawnside/duskside with increasing magnitude of IMF By. While the IMF By dependence is qualitatively consistent with the tilt of the two-cell convection pattern [e.g., Weimer 2005], the patches are often seen to exit before 9 MLT under large negative IMF By (~−5.0 nT). The patch departures can be found as early as ~6 MLT, which is much farther away from noon than previously studied by [*Drury et al*., 2003], while the qualitative trend is consistent with their study. Since the throat of two-cell convection is not generally expected at such MLT, the patch motion likely involves substantial azimuthal propagation from initial PMAF locations closer to noon to the patch departure location.

The data points in Figure 5.4b, which shows the IMF Bz dependence of depart-oval MLT, are much more scattered than those in Figure 5.4a, and no depart-oval MLT dependence on IMF Bz is discernible.

5.3.3 IMF clock angle dependence

Figure 5.5a-d shows the IMF clock angle dependence of the maximum density, flow channel width and maximum flow speed associated with the polar cap patches. Clock angle is the angle between GSM north and the projection of the IMF vector onto the GSM y–z plane and is determined as the arctangent of By/Bz. In these figures, clock angles are from 0° to 180° clockwise from top to bottom. Figure 5.5a shows that most maximum densities of airglow patches are relatively small for small ratio of IMF |Bz| and |By|. Although the flow channel widths shown in Figure 5.5c do not show a clear trend, since all measured widths are less than 1000 km (~300 km on average), these are all localized flow channels rather than larger-scale convection, which would extend over a few 1000 km. Interestingly, a notable IMF By effect is shown in Figure 5.5d, where fast flows of >~1500 m/s are predominantly seen during large |By| and small |Bz|. Under a large IMF By condition, it has been observed that mesoscale flows in the cusp region propagate poleward, and this has been suggested to be due to large tension force in dayside reconnection under large IMF |By| [*Lockwood et al.*, 2005; *Rinne et al.*, 2010; *Sandholt et al.*, 2004a; *Zhang et al.*, 2011]. Combining with our observation, these mesoscale flows may move far away from the noon meridian and then propagate into the polar cap. The bias toward negative By is due to the conjunctions (DMSP within ASI FOV) occurring preferentially at pre-noon MLT. The average flow speed is ~1100 m/s.

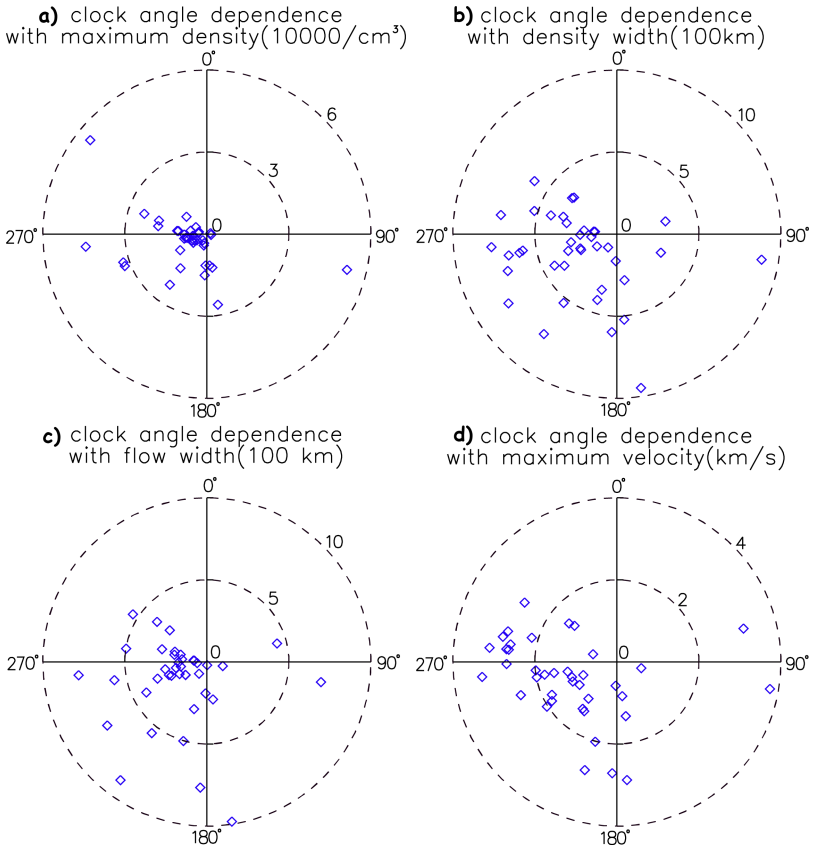

Figure 5.5 IMF clock angle dependence of a maximum density, b density width, c flow width and d maximum velocity. The angle between By and Bz is from 0° to 180° clockwise from top to bottom.

5.4 Conclusions

To understand the propagation relations between, and characteristics of, dayside polar cap patches and related flow structures, we traced airglow patches and investigated density and flow structures under different IMF conditions using coordinated observations of the AGO ASI and DMSP satellites in the southern hemisphere.

We showed that polar cap patches are often (45 out of 60 events) collocated with longitudinally narrow flow enhancements. Flow velocities over the patches are substantially larger than in the surrounding regions that would represent large-scale background convection,

and the flow channel widths are comparable to the enhanced density widths. We thus conclude that dayside polar cap patches are associated with localized polar cap flow enhancements rather than patches being carried by large-scale convection. Since the patches emanated from PMAFs within the dayside auroral oval, we suggest that the flow channels may originate in the dayside auroral oval and propagate into the polar cap. Dayside reconnection could be a trigger of the fast flows that bring enhanced density from the dayside auroral oval to the polar cap by maintaining the flow channel characteristics over substantial distances. Furthermore, the dayside flow channels could be the source of those measured in the nightside polar cap.

We also found that many PMAFs move azimuthally away from noon over a few hours of MLT and then leave polar cap patches behind just poleward of the auroral oval. The departure into the polar cap can be found as early as 6 MLT. These patches away from noon tend to be measured when the IMF By is large. Thus, we also investigated the IMF clock angle dependence of properties of the airglow patches and related fast flows. The flow channel speeds average 1100 m/s over the observed patches, and the average width is 300 km. More broad density enhancements and flow channels (>~500 km) occur during southward Bz. It is also interesting that large enhancement of density (>~30,000 #/cm3) are By dominated. Fast flows of >~1500 m/s are predominantly seen during large IMF-By and small |Bz|, consistent with enhanced thermospheric cusp heating with increasing |By| [*Carlson*, 2012], and the flow speed decreases with increasing-Bz.

The -By preference is consistent with the duskside convection cell extending toward dawn and giving a higher possibility of a flow channels being seen on the dawnside FOV. It is known that for large, negative By, the boundary between dawn and dusk convection cells is shifted toward dawn in the southern hemisphere [*Lyons*, 1996; *Reiff & Burch*, 1985] and toward

dusk in the northern hemisphere [*Weimer*, 2005]. Additionally, the previous case studies have shown the IMF By-related formation of polar cap patches [*Lockwood et al*., 2005; *Zhang et al*., 2011, 2013]. In our study, we statistically showed that the departing points of these patches from the poleward boundary of auroral oval are associated with IMF By, and moreover, the airglow patches that depart at <9 MLT are with strong negative By. Thus, our observations suggest that patches and flow channels with high flow speeds are guided by the asymmetric By flow pattern, bringing them toward dawn in the southern hemisphere.

CHAPTER 6

Magnetospheric and ionospheric responses to a foreshock transient in a 2D perspective

In this chapter, the magnetospheric and ionospheric responses to a foreshock transient on June 25, 2008 are identified in a 2D perspective, by the coordinated observation of the THEMIS satellites and the ASI at South Pole. Section 6.1 presents the instruments used in this study; Section 6.2 shows the observation by the THEMIS satellites; Section 6.3 and 6.4 show the observations by the ASI at South Pole; and a discussion and a conclusion are shown in Section 6.5 and 6.6, respectively.

6.1 Instrument locations for the conjunction events

This study uses the THEMIS satellite to observe the upstream activities and their corresponding responses in the magnetosphere, and the monochromatic ASI at South Pole station in Antarctica to identify dayside discrete and diffuse aurora.

During 1530 through 1555 UT on June 25, 2008, THEMIS B and C were in the dayside solar wind, near the bow shock, while THEMIS A, D, E stayed in the dayside magnetosphere. The THEMIS satellites observations are thus used to observe the upstream activities and their corresponding responses in the magnetosphere. As shown by the mapping to equatorial plane through the T01 model in Figure 6.1C, the ASI at South Pole covered an area that swept across noon during the same period. It is clear that the FOV has a good conjunction with all the

THEMIS satellites, which is benefit to identify the auroral responses to the upstream disturbances.

We also utilize the ground-based magnetometers at high latitudes in the northern hemisphere to calculate the horizontal currents and geosynchronous GOES and interplanetary ACE spacecraft measurements.

6.2 THEMIS Satellite Observations

6.2.1 A Foreshock Transient

Figure 6.1 summarizes the THEMIS satellite observations and also shows red- and green-line imager keograms. Figures 6.1Ad and 6.1Ah show that during 1536-1541 UT and 1537-1545 UT, a foreshock transient, which appears to propagate toward the bow shock with suprathermal particles, is identified to cross THEMIS-B and C, respectively. Both satellites observed two discontinuities and suprathermal ions within them. The first discontinuity was observed by THEMIS-B and C at 1534:40 and 1536:58 UT, respectively. The second discontinuity was observed by THEMIS-B and C at 1540:45 and 1544:18 UT, respectively.

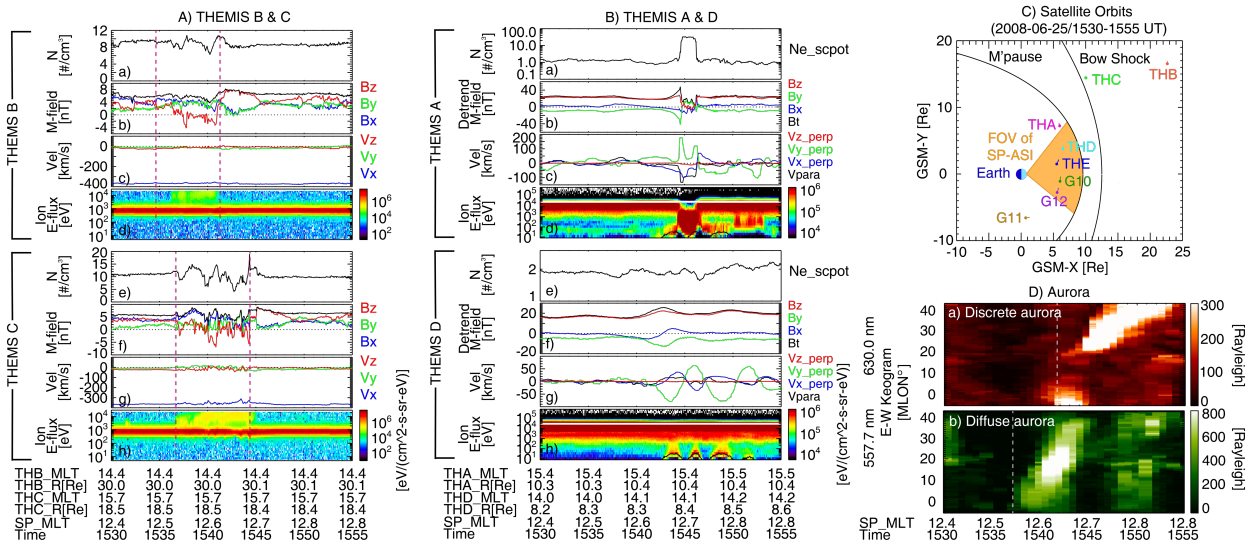

Figure 6.1 (Aa–Ad) The plasma density, magnetic field, flow velocity, and ion energy flux observed by THEMIS B during 1530 UT through 1555 UT. (Ae–Ah) The same format as (Aa)–(Ad), except for THEMIS C. The magenta dashed lines in (Aa)-(Ad) present the IMF discontinuities. (Ba-Bd) Plasma density, detrended magnetic field, flow velocity, and ion energy flux observed by THEMIS-A during 1530 UT through 1555 UT. (Be-Bh) The same format as (Ba)-(Bd), except for THEMIS-D. The black lines in (Bd) and (Bh) show the kinetic energy by the bulk flow moment. (C) shows the orbits of the THEMIS satellites and the field of view of the all-sky imager at South Pole station during 1400 UT through 1600 UT. The positions of magnetopause and bow shock are obtained by the models described in *Shue et al.*, [1998] and *Wu et al.*, [2000], respectively. (Da and Db) The keograms of red-line emission and green-line emission, respectively, during 1530 UT through 1555 UT. Here in order to show variations clearly, the background is subtracted in original snapshots (Ba-Bh and Da-Db) and east-west keograms (Ad), where the background is defined as the median luminosity at each pixel within±10 min from each observation time. The white dashed lines show the initial timings of auroral brightening.

To identify the normal of the discontinuities, the timing method based on ACE and THEMIS B and C satellites is utilized. The first discontinuity was observed by ACE at 1420:48 UT. Based on those three satellites, the normal of this discontinuity is about (0.37, –0.93, –0.06) in GSM coordinates. It would arrive at the dawnside first and sweep duskward. The second discontinuity was observed by ACE at 1425:06 UT. The calculation shows that the normal of this discontinuity is about (0.37, –0.87, –0.34) in GSM. It would also arrive at the dawnside first and sweep duskward. The second and third columns of Table 6.1 show the timings of arrival of these

two discontinuities at the locations of five satellites. The magnetic fields in the normal direction of those two discontinuities were less than ~0.1 of the total magnetic field, and their normals calculated from the cross-product method [*Hudson*, 1970] were consistent with those from the timing method. This indicates that these two discontinuities were tangential discontinuities.

Table 6.1 Timings of the Signatures in the Upstream and Downstream

Location [MLT]	**First discontinuity contacted the bow shock [UT]**	**Second discontinuity contacted the bow shock [UT]**	**Magnetospheric signatures [UT]**	**Diffuse auroral pattern [UT]**
10.3	1527:55	1531:11	1533:00 [G12]	1536:00
11.3	1529:11	1533:25	1534:00 [G10]	1538:20
13.2	1531:45	1537:49	1539:00 [THE]	1542:40
14.0	1533:01	1539:55	1541:00 [THD]	1544:30
15.5	1536:00	1544:41	1544:00 [THA]	1548:00

Note: The first column shows the MLTs of five satellites (Geotail12 and 10 and Time History of Events and Macroscale Interactions during Substorms E, D, and A from top to bottom) in the magnetosphere; the second and second columns show when the first and second discontinuities contacted the bow shock at those locations, respectively; the fourth column shows the magnetospheric signatures observed by the five satellites; the last column shows when the diffuse auroral patterns arrived in those five locations.

The cone angles of the magnetic field within the two tangential discontinuities at THEMIS-B and C are ~45°and ~26°, respectively, which are relatively lower than in the background solar wind (~60°). The lower cone angles indicate that the magnetic field within these two discontinuities were connected to the bow shock and therefore the ions are reflected and accelerated, forming the foreshock region within the discontinuities. In addition, the depression of magnetic field and the density, small compressions at the edges but no significant flow deflection is found in both satellite data. Those signatures indicate that this foreshock

transient is probably a foreshock cavity. In addition, during the foreshock observations, the magnetic field became more fluctuating than the background (Figures 6.1Ab and 6.1Af). The foreshock region was also associated with two density reductions sandwiched by density increases (Figure 6.1Aa). THEMIS-C observed essentially the same structures with a-few-minute propagation delay, except that the amplitudes were larger and the disturbance lasted longer. Figure 1Af presents a significant Bz reduction (~1537 UT) followed by an increase in Bz (~1545 UT), associated with low-frequency fluctuation. Although velocity changes were small, the foreshock region was associated with small decreases in |Vx| (Figure 6.1Ag). Those transient foreshock signatures are consistent with a proto-HFA by *Zhang et al*. [2010] though the velocity reduction is small. The small velocity change at the satellite location could be because the bulk of the structure may be localized near the bow shock and the satellites only detected an early stage or a portion of the structure.

At the same time, there was no appreciable change in the pristine solar wind density and velocity before and after the foreshock transient, and the dynamic pressure in the ACE data during this period was almost constant. Thus, it cannot be an interplanetary shock, so that this foreshock transient is probably a foreshock cavity or possibly an HFA, which was sandwiched by two tangential discontinuities.

6.2.2 Magnetosheath and Magnetospheric Signatures

During the same period, THEMIS-A was located at ~15.5 MLT and ~9.5 Re away from the Earth in the magnetosphere. Figures 6.1Ba-6.1Bd show THEMIS-A observation of the density, detrended magnetic field, flow velocity, and ion energy flux, respectively. Here Figure 6.1Bb shows the magnetic field that is detrended by the T01 model. During 1544-1546 UT, high

energy (>1 keV) particles almost disappeared, while low-energy particle fluxes (<1 keV) became higher, and the magnetic field decreased. Those signatures indicate a magnetopause crossing, and THEMIS-A was in the magnetosheath during that 2 min. Thus, at the position of THEMIS-A, there was a brief magnetopause compression at ~1544 UT. Additionally, the GSM-X component of velocity in the magnetosheath approached to ~100 km/s, which was fast compared with the background flow (~30-40 km/s in this case). This magnetosheath fast flow was identified as a magnetosheath high speed jet (HSJ) by *Dmitriev & Suvorova*, [2012]. It could be due to the impact of the foreshock transient [*Archer et al*., 2014] and can also cause magnetospheric compression and fast channels in ionosphere [*Archer et al*., 2013; *Hietala et al*., 2012].

The observation by THEMIS-D, which was located at ~14.0 MLT and ~7.5 Re away from the Earth in the magnetosphere, is shown in Figures 6.1Be-6.1Bh with the same format as Figures 6.1Ba-6.1Bd. Starting from ~1540 UT, THEMIS-D observed a gradual increase in the GSM-Z component of detrended magnetic field followed by ULF waves that are observed in both magnetic field and velocity. Those two signatures, which are generally considered to be the responses to magnetopause compressions [*Lysak & Lee*, 1992; *Takahashi et al*., 1988], also occurred soon after the occurrence of the observed foreshock transient. *Shen et al*., [2018] shows that the compressional waves induced oscillations perpendicular to the magnetic field and that those are a field line resonance (FLR). The black line in Figure 6.1Bh shows the kinetic energy of the bulk flow moment and demonstrates that the energy variation apparent in the spectra is due to the flow velocity oscillations caused by the impact of the transient.

Other satellites, that is, GOES-12 and 10 and THEMIS-E (not shown), located at ~10.3, 11.3, and 13.2 MLT, respectively, also observed compressional signals in magnetic field (Bz increase and ULF waves) at ~1533, 1534, and 1539 UT, respectively. The timings when all five

satellites (GOES-12 and 10 and THEMIS-E, D, and A) observed magnetospheric compressional signatures are listed in the fourth column of Table 6.1. Both the foreshock transient and the magnetospheric signatures took 11-14 min to propagate from 10.3 to 15.5 MLT. This indicates that the magnetospheric compression is most likely driven by the foreshock transient and that the magnetosphere took ~10 min to respond to the foreshock transient.

6.3 Evolution of Diffuse Auroral Brightening

Figures 6.1Da and 6.1Db show east-west keograms of red- and green-line emission, respectively, from the South Pole imager data (at -74° MLAT). The green-line emission shows that diffuse aurora began to brighten at ~1537 UT and started to propagate duskward. At ~1542 UT, the red-line emission shows that the discrete aurora began to brighten and also propagated duskward, a pattern similar to that of the diffuse aurora.

Figure 6.2 shows snapshots of background-subtracted green-line emission observed by the ASI at South Pole station in magnetic coordinates. In order to quantify a characteristic size and speed of auroral structures, we identify an area above 1/e of the maximum luminosity above the background for each snapshot in each wavelength. Here the background is defined as a median luminosity at each pixel within ±10 min from each observation time. Since the auroral brightening of interest lasted less than 10 min, this background gives a representative value of luminosity before/after the event at each pixel. The choice of 1/e threshold is made because latitudinal and longitudinal profiles of emission often show roughly Gaussian-like distributions.

The yellow contour lines in Figure 6.2 present the characteristic boundary of emission using the method described in section 6.1. The FOV was dark until 1536:14 UT. A bright pattern showed up at the western edge of the FOV at 1538:23 UT. The position of this initial pattern is at

~4° MLON and ~-73° MLAT, at ~10 MLT in the ionosphere. The following snapshots show that the structure became larger and brighter until 1541:59 UT. The pattern extended in size to at most ~25° in MLON and ~5° MLAT in width. Those correspond to ~900 and ~590 km in the east-west and north-south directions, respectively, at the altitude of ~110 km in the ionosphere. Then, the brightening pattern started to become dimmer, smaller, and disappeared near the eastern edge of the FOV at 1545:35 UT. During the entire process, this diffuse auroral structure propagated duskward by ~3 hr MLT.

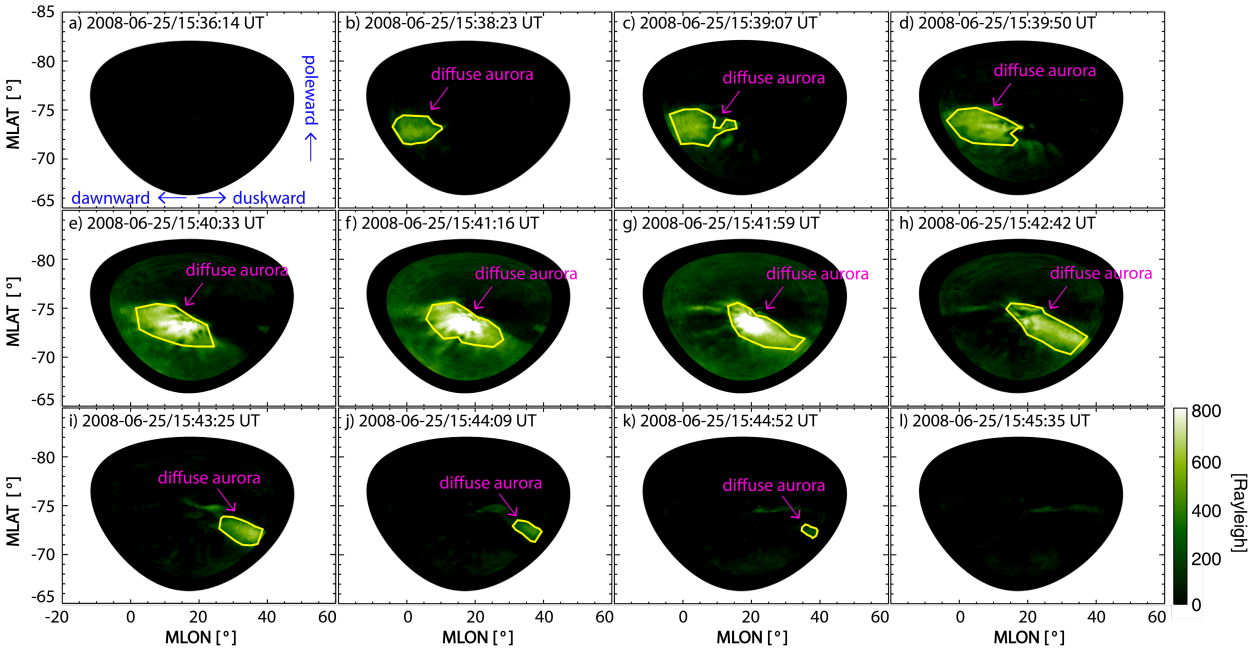

Figure 6.2 Snapshots of green-line emission observed by the all-sky imager at South Pole station during 1536:14 UT through 1545:35 UT on 25 June 2008. The x axis is magnetic longitude, and the y axis is magnetic latitude. The yellow contour lines identify patterns of diffuse aurora.

The initiation of the diffuse aurora occurred 2 min after the foreshock transient measurement by THEMIS-C. Although this time lag is somewhat short compared to a signal propagation from the satellite to the ionosphere, as shown later, it should be noted that the auroral signature was detected first in the prenoon sector and propagated to postnoon, while the

satellite was in the postnoon sector. This propagation indicates that the satellite did not detect the earliest signature in the prenoon sector but encountered the signal later when the structure reached the postnoon sector. This is also consistent with the THEMIS-A observation that the magnetopause crossing in the postnoon sector was later than the initiation of aurora in the prenoon sector and that the plasma flow at the magnetopause was predominantly duskward.

The diffuse auroral structures shown in Figures 6.2b-6.2k are mapped to the equatorial plane by the T01 model [*Tsyganenko*, 2002]. The red star in each panel of Figure 6.3 shows a mapped position of the centroid of the diffuse auroral structures seen in the ionosphere. The mapped patterns show a more significant expansion in the GSM-Y direction than in the GSM-X direction: The pattern was initially centered at ~[8.2, -2.7] Re in GSM with a width of 1.4 Re in the X direction and 2.2 Re in the Y direction (Figure 6.3a). Figures 6.3b-6.3j show that the mapped pattern expanded to at most 6.3 Re in GSM-Y at 1540:33 UT and then decayed to 0.8 Re in GSM-Y at 1544:52 UT. The range of 0.8-4.3 Re is overall comparable to the azimuthal size of foreshock transients [a few Re; [*Lin*, 2002; *Parks et al*., 2006; *Plaschke et al*., 2016a; *Turner et al*., 2013; *Zhang et al*., 2010]. The mapped pattern also shows a duskward propagation to ~[8.2, 2.7] Re in GSM.

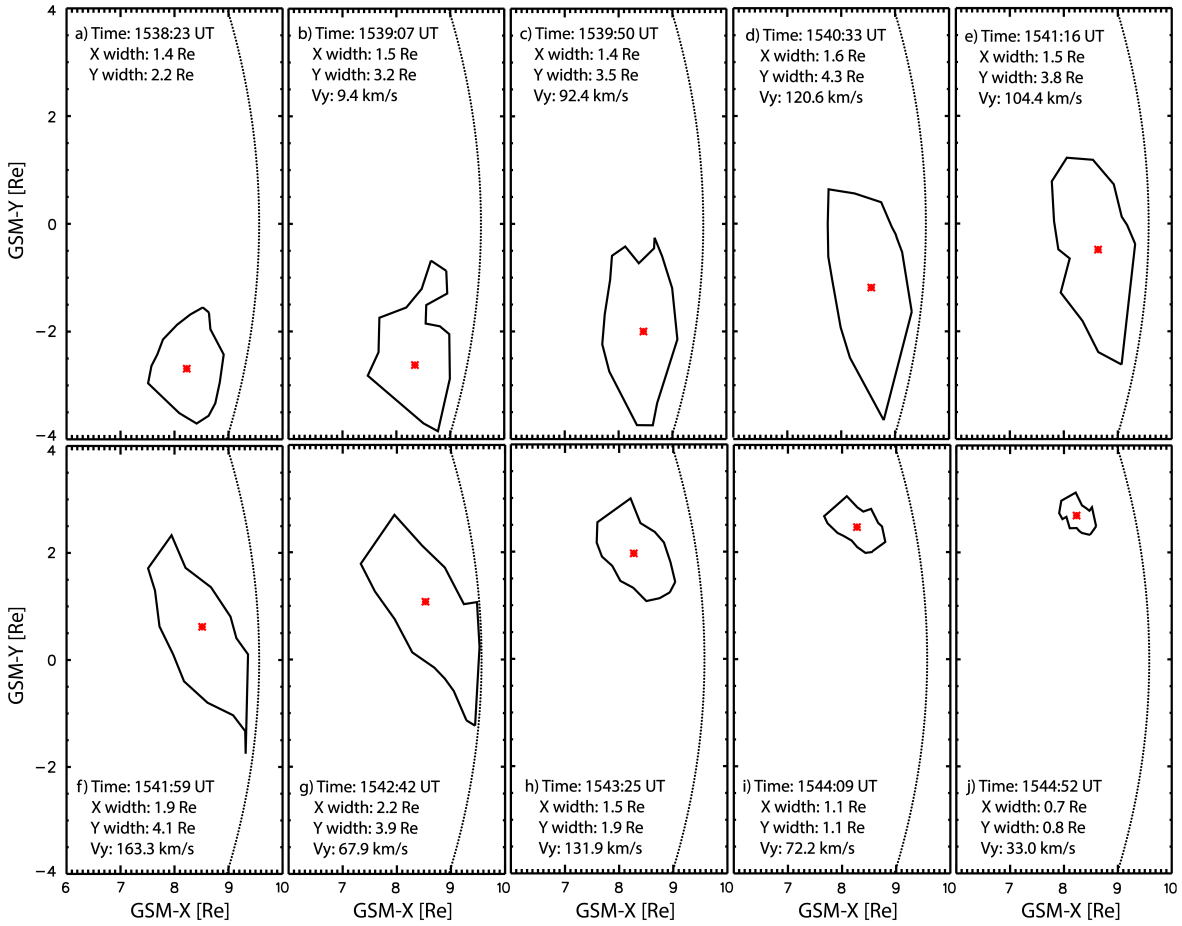

Figure 6.3 Mapped patterns of diffuse auroral brightening on the equatorial plane by the T01 model during 1539:50 UT through 1544:52 UT on 25 June 2008. The red stars show mapped position of the centroid of diffuse auroral brightening patterns. The dashed curves show the position of magnetopause *Shue et al*., [1998].

Figures 6.4a-6.4c plot the magnetic longitudes, GSM-Y position, and MLT, respectively, of the centroids of the mapped diffuse auroral patterns (shown as the larger blue squares). The smaller squares show the corresponding maximum and minimum values of each mapped patterns, corresponding to their leading and trailing edges, respectively. We also did linear fitting on each sets of data (shown as magenta and orange lines). Since the diffuse auroral structures in the first two (in Figures 6.2b and 6.2c) and the last two (in Figures 6.2j and 6.2k) snapshots were close to the edge of the FOV, the linear fitting of centroids was done on the six points from 1539:50 to

1943:25 UT. Similarly, since the leading edges of those patterns are only shown in the first eight snapshots (Figures 6.2b-6.2i), the linear fitting of the leading edges was done on the first eight points. And since the trailing edges of those patterns are only shown in the last eight snapshots (Figures 6.2d–6.2k), the linear fitting of the trailing edges was done on the last eight points.

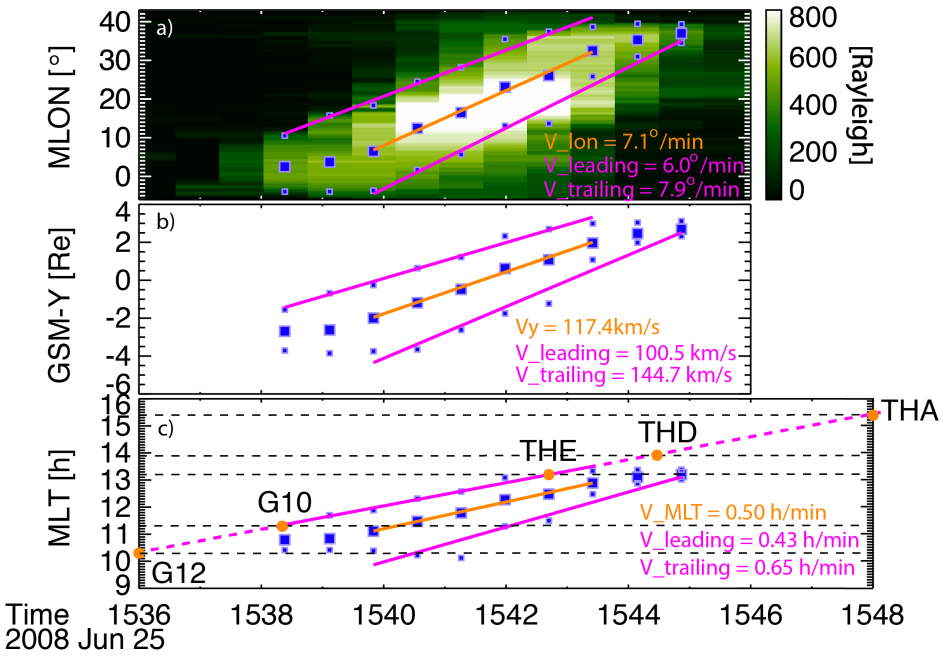

Figure 6.4 (a) The keogram of the green-line emission. The larger blue squares present the centroids of the patterns of diffuse auroral brightening in the ionosphere. (b and c) The geocentric solar magnetospheric Y and MLT positions of the mapped centroids by the T01 model to the equatorial plane. The smaller blue squares present the edges of the patterns of diffuse auroral brightening. The orange and magenta lines describe the linear fitting of those points. The orange dots show the MLT position of GOES 12 and 10 and Time History of Events and Macroscale Interactions during Substorms A, D, and E.

From Figure 6.4a, the average velocity in the ionosphere that is obtained by the linear fitting is ~7.1°/min or ~235 km/min in the ionosphere. The speeds of the leading and trailing edges are ~6.0 and ~7.9°/min, respectively or ~198 and ~261 km/min, respectively, in the ionosphere. Figure 6.4b shows that the average velocity of the mapped patterns in GSM-Y direction on the equatorial plane is ~117.4 km/s. The speeds of their leading and trailing edges

are ~100.5 and ~144.7 km/s, respectively. Figure 6.4c shows that the average velocity of MLTs of the mapped patterns on the equatorial plane is ~0.50 hr/min. The speeds of their leading and trailing edges are ~0.43 and ~0.65 hr/min, respectively.

While the numbers mentioned here depend on mapping altitudes, the structures measured near zenith (~1540-1542 UT) should be most reliable. The size and propagation speed are nearly constant except in the first and last couple of snapshots as shown in Figure 6.4 where edge effects are significant. Thus, the numbers we obtained reasonably represent the ionospheric size and speed of the diffuse aurora induced by the foreshock transient.

Based on the results shown above, we obtain the timings when the diffuse auroral brightening arrived at the MLTs of the five satellites and listed them in the last column of Table 6.1. Similar to the foreshock transient and the magnetospheric signatures, diffuse aurora also took ~12 min to propagate from 10.3 to 15.5 MLT. This indicates that the diffuse aurora traces the upstream motion well. It is also noted that the diffuse aurora took ~3-4 min to respond to the magnetospheric signatures. This time delay is reasonable to include the response time of kinetic processes in magnetosheath, wave-particle interaction to the magnetosphere compression, M-I communication time, and the imager time resolution (~44 s).

6.4 Evolution of discrete auroral brightening

Figure 6.5 shows snapshots of red-line emission data observed by the ASI at South Pole station. Much of the emissions is seen a few degrees poleward of the diffuse aurora. As introduced in Chapter 1, red-line emission mainly sees discrete aurora due to low energy precipitation near the open-closed boundary. Faint emissions are also seen in the region of the green-line diffuse aurora and propagate duskward (Figures 6.5a-6.5f). Those are likely due to

low-energy portion of precipitation from the dayside closed field lines despite small fluxes. The red-line signature of the diffuse aurora helps us compare diffuse and discrete aurora evolution.

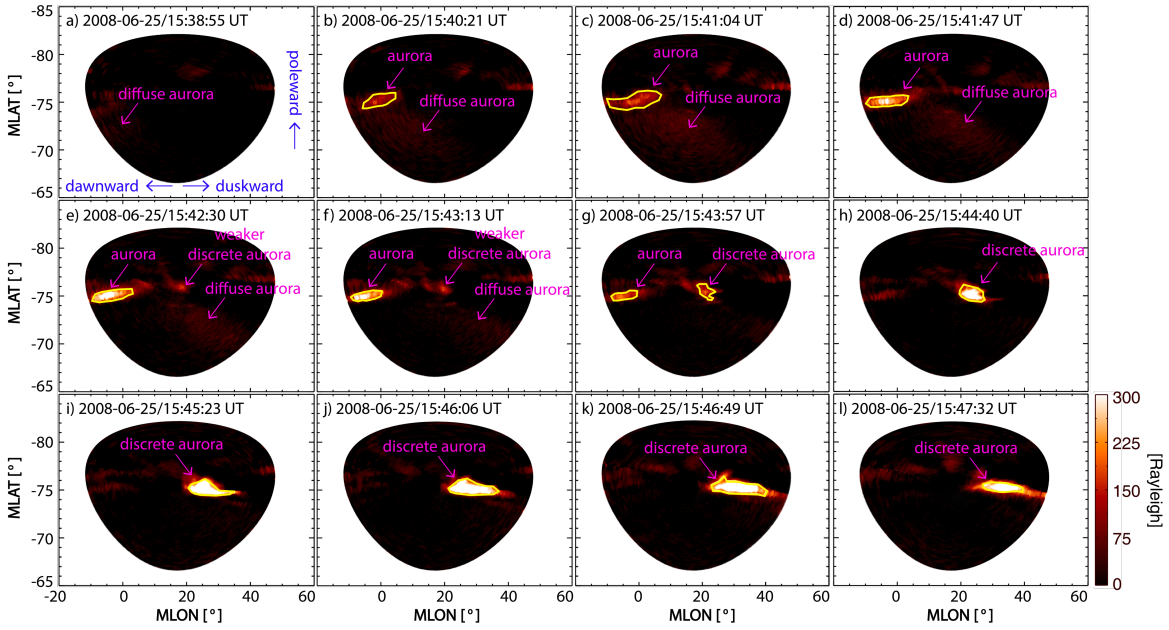

Figure 6.5 Snapshots of red-line emission observed by the all-sky imager at South Pole station during 1538:55 UT through 1547:32 UT on 25 June 2008. The x axis is magnetic longitude, and the y axis is magnetic latitudes. The yellow contour lines identify patterns of discrete/diffuse aurora.

The red-line emission started to brighten at 1540:21 UT at ~-75° MLAT, 2 min after the green-line aurora. This pattern became brighter until 1542:30 UT, and it then decayed and disappeared at 1544:40 UT. This structure was located near the dawnside edge of the imager FOV, and it is hard to examine whether it is discrete or diffuse aurora. Unlike the green-line diffuse aurora, this pattern essentially stayed at the initial position.

At 1542:30 UT, ~4 min after the emergence of the green-line diffuse aurora, another auroral brightening emerged near the center of the imager FOV. At this time, the brightening was at the similar magnetic longitude, but higher magnetic latitude than the diffuse aurora in the same snapshot. Then it became brighter, larger, and also extended and propagated duskward. It had

sharp edges and small structures, indicating that this is a discrete aurora. As shown in Figure 6.1D, the discrete aurora had a similar dawn-dusk extent to that of the diffuse aurora and propagated duskward at a slightly smaller rate. We did not examine equatorial mapping because the T01 model predicts that these structures are on open field lines.

Since discrete aurora is formed by electron precipitation that carries upward FACs, FACs are expected to be associated with the discrete auroral brightening. In fact, Shen et al., [2018] shows that dayside high-latitude ground magnetometers in the northern hemisphere had transient oscillations in the ULF frequency range. We calculated equivalent horizontal current distributions using magnetometer data available through SuperMAG. The method is described in Nishimura et al. [2016]. Here generators of FACs are in the magnetosphere, and the two ionospheres are the load of the electrical circuit. The sense of FACs relative to the ground is thus the same in the both hemispheres (upward FACs are present on roughly the same field line in the two hemispheres). This allows us to compare the upward FAC in the northern hemisphere and aurora in the southern hemisphere.

Figure 6.6 shows equivalent horizontal currents in green-lines, and positions of the magnetometers are shown by green dots. To see the current variances better, we subtracted the currents at 1534 UT as background, when both solar wind and aurora were steady. At ~1536 UT, the upward FAC shown in the prenoon sector and another current shear in the postnoon sector indicate the existence of a region-2 (R2)-sense current. This timing corresponds to the initiation of the diffuse aurora. Then this R2 sense current disappeared quickly. At 1541 UT, a pair of the R1-sense current emerged near the noon. The counterclockwise horizontal current vortex, which corresponds to an upward FAC of this R1-sense current, became more intense and propagated duskward (~13 MLT at 1541 UT in Figure 6.6c; ~15 MLT at 1546 UT in Figure 6.6d). The

positions of this current vortex are consistent with the positions of the high-latitude red-line auroral pattern shown in Figure 6.5, supporting the inference that the discrete auroral location and propagation display evolution of upward FACs due to the foreshock transient-magnetopause interaction. Here the consistency of the initiation times of the horizontal currents and the auroral brightenings observed by the ASI at the south-pole also suggests that the interhemispheric comparison is reasonable.

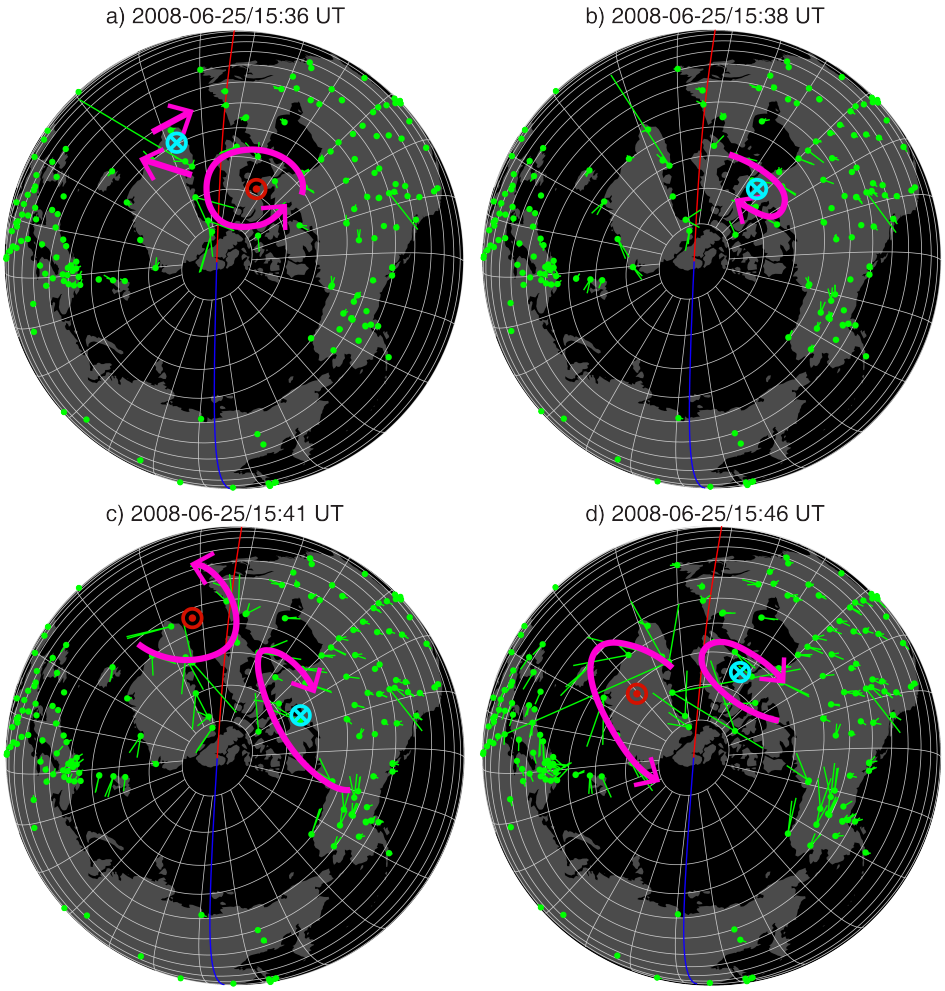

Figure 6.6 Horizontal equivalent currents that are calculated from the magnetic field observed by ground-based magnetometers in the northern hemisphere during 1536 UT through 1546 UT on 25 June 2008. The green dots show the position of the magnetometer, and the green-lines present the direction and magnitude of horizontal current. The red and blue lines indicate the noon and midnight meridians, respectively. The magenta circles schematically indicate current vortexes.

6.5 Discussion

In this event, the green-line diffuse aurora was detected a few minutes before the red-line discrete aurora and was located equatorward of the discrete aurora, both of which propagated duskward. Ground-based magnetometers also show a pair of R2-sense FACs during the diffuse aurora followed by a clear duskward-moving anticlockwise horizontal current vortex (upward FAC) associated with the discrete aurora. These signatures are analogous to auroral and ionospheric current responses during dynamic pressure pulses except that the scale size is smaller: *Nishimura et al*., [2016] observed a pair of R2 and then R1-sense currents associated with a discrete auroral brightening after a diffuse auroral brightening and identified this as the response to primary and main impulses of sudden commencement (SC) events. This similarity indicates that the magnetospheric and ionospheric responses to the foreshock transient possibly follow the same physics as during SCs in a smaller scale size, namely, magnetospheric compression and enhanced R2 and R1-sense FACs. Also, the association between the red-line aurora and ground magnetic field is analogous to that during TCVs [*Vorobjev & Zverev*, 1993]. TCVs have been shown as a response of upstream foreshock transients [*Murr & Hughes*, 2003; *Sitar et al*., 1998], consistent with what we found in this study.

This interpretation is also consistent with the magnetopause compression observed by all five satellites in the magnetosphere. However, the magnetopause crossing only lasted for a few minutes, and the solar wind dynamic pressure measured by THEMIS B and C did not change before and after the foreshock transient. Thus, the measured magnetospheric and ionospheric responses are not due to an interplanetary shock but due to the foreshock transient.

The time delay between the in-situ and ionosphere signals would arise from a finite response time of wave-particle interaction to the magnetospheric compression, M-I

communication time, and the imager time resolution. [*Chi et al*., 2006] showed that the dayside signal propagation time is about a minute. The time delay we found is roughly a full bounce period of Alfven waves between the two hemispheres, as possibly a time scale for the (R2-sense) current system to develop.

Figure 6.7 shows a schematic illustration of magnetospheric and auroral responses to the foreshock transient on 25 June 2008. The foreshock transient locally compresses the magnetopause and launches ULF waves in the magnetosphere and FACs. Energetic electron precipitation associated with upward FACs and enhanced wave-particle interaction drives localized discrete/diffuse auroral brightening. The auroral location and size (~4.3 Re as maximum) indicate the MLT and finite azimuthal extent of the foreshock transient interacting with the magnetopause. The duskward propagation of aurora reflects the duskward propagation of the foreshock transient as it swept through the magnetosheath while impacting the magnetopause.

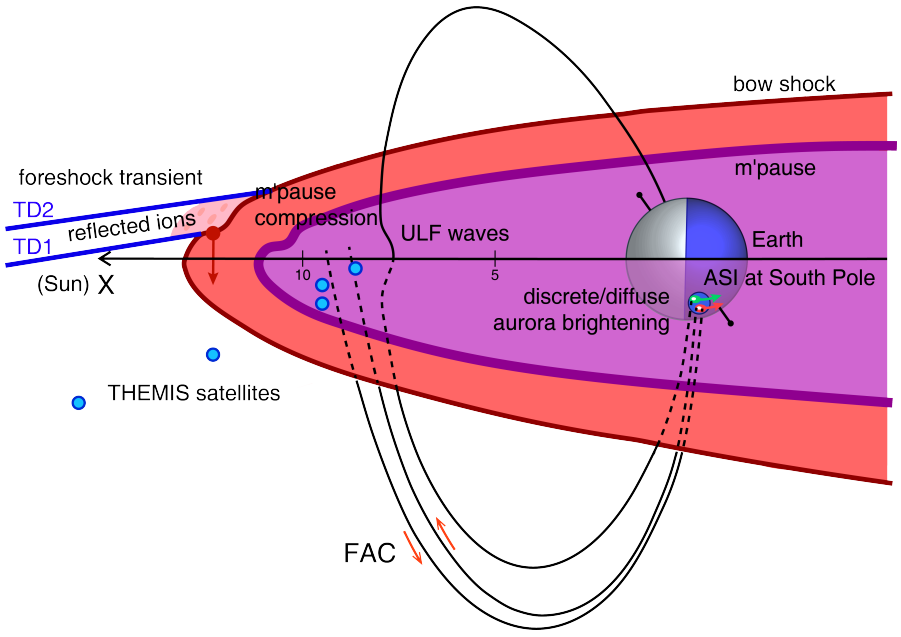

Figure 6.7 Schematic illustration of magnetospheric and auroral responses to the foreshock transient on 25 June 2008.

6.6 Conclusion

This work provides the analysis of the foreshock transient evolution/propagation in a 2D perspective on 25 June 2008, based on the observation by the THEMIS and GOES satellites, ASI at South Pole station, and magnetometers in Greenland and Canada. Although it is generally difficult to identify 2D evolution of interaction between a foreshock transient and magnetospheric responses due to limited observation points, the present study shows that the foreshock transient is geoeffective and their interaction with the magnetosphere can be imaged using dayside aurora more precisely in a 2D perspective than by other means of measurements.

1. A foreshock transient was observed by THEMIS B and C to propagate toward the Earth. The transient is probably a foreshock cavity or possibly a proto-HFA, which was sandwiched within two tangential discontinuities and swept through the magnetosheath from dawnside to duskside. A magnetopause crossing and ULF waves were detected in the subsequent ~10 min.
2. Diffuse aurora brightened soon after the foreshock transient observation. The mapped pattern of diffuse auroral brightening on the equatorial plane shows a width of ~4.3 Re in GSM-Y direction, which is slightly larger but similar to the typical size of foreshock transients. The average velocity of the mapped pattern is ~100.0 km/s in GSM-Y direction, similar to the motion of the upstream foreshock transient. The diffuse aurora also brightened in coincidence with the occurrence of R2-sense FAC.
3. Discrete aurora brightened soon after diffuse aurora brightened. The discrete auroral brightening also shows a localized signature and propagated duskward. The equivalent

current pattern shows that the discrete auroral brightening is associated with the upward FAC portion of the R1-sense FAC.

The substantial geophysical impacts, including magnetospheric compression, auroral brightening, and FACs, which are driven by foreshock transients, are analogous to those during SCs except at a smaller scale size. A statistical perspective study of this phenomenon is warranted for the future.

CHAPTER 7

Magnetospheric and ionospheric responses to magnetosheath HSJs in a 2D perspective

Besides foreshock transients, in this chapter, the ionospheric and magnetospheric responses to HSJs in the magnetosheath are presented in a 2D perspective, by a coordinated observation between the THEMIS satellites and optical imagers at South Pole. Section 7.1 shows the instruments and data set in this study; Section 7.2 shows two case studies; Section 7.3 presents a multi-case study; a discussion and a conclusion are shown in Section 7.4 and 7.5, respectively.

7.1 Instrument locations for the conjunction events

This study uses the THEMIS satellites to measure plasma and fields in the solar wind, magnetosheath, and the dayside magnetosphere, and the monochromatic ASI at the South Pole station in Antarctica to identify dayside discrete and diffuse aurora.

We use a conjunction between the THEMIS satellites and ASI imager at South Pole station during 2008 through 2010, during which *Plaschke et al*., [2013] identified 1010 magnetosheath HSJs by the THEMIS satellites. In order to examine auroral responses to HSJs accurately, we selected HSJs or groups of HSJs, each of which is preceded by a steady magnetosheath without HSJs in the preceding 15 min. If the time interval between two HSJs is less than 15 min, those two HSJs are grouped as one HSJ event. We also require that each HSJ

should last for longer than ~1 min, which is about the time resolution of the ASI at South Pole. To find imager conjunction, we require that HSJs should be observed not only on the dayside (9–15 MLT) but also within ±1 MLT from the aurora of interest in the FOV of the ASI of South Pole station. Moreover, in order to obtain magnetospheric observation, at least one of the THEMIS satellites should be in the magnetosphere and its T01-footprint should be within ±3 MLT from the center of the FOV of the ASI.

The sky condition is required to be favorable, where clouds and light contamination should not cover more than half of the FOV. Additionally, to remove the noise and star lights in the FOV, we smooth each snapshot with a 5-pixel window. The size of discrete and diffuse auroral brightenings is identified as 1/e of the peak luminosity above the background. Here the background is defined as a median luminosity at each pixel within ±30 min from each observation time.

Based on those criteria, eight HSJ events are selected by surveying the data during 2008 through 2010. Two out of those are presented in the next section in detail.

7.2 Case Study

7.2.1 First Case: 15 July 2009

The first HSJ event included two HSJs, which were identified at 1723:27 and 17:28:29 UT on 15 July 2009 in the dayside magnetosheath by THEMIS C by *Plaschke et al*., [2013]. In this event, the center of the South Pole station imager FOV was at ~14.5 MLT and the THEMIS satellite probes were located in the solar wind, the magnetosheath, and the magnetosphere in the postnoon sector (Figure 7.1A), which was ideal to investigate solar wind-magnetosheath-magnetosphere interaction during this event.

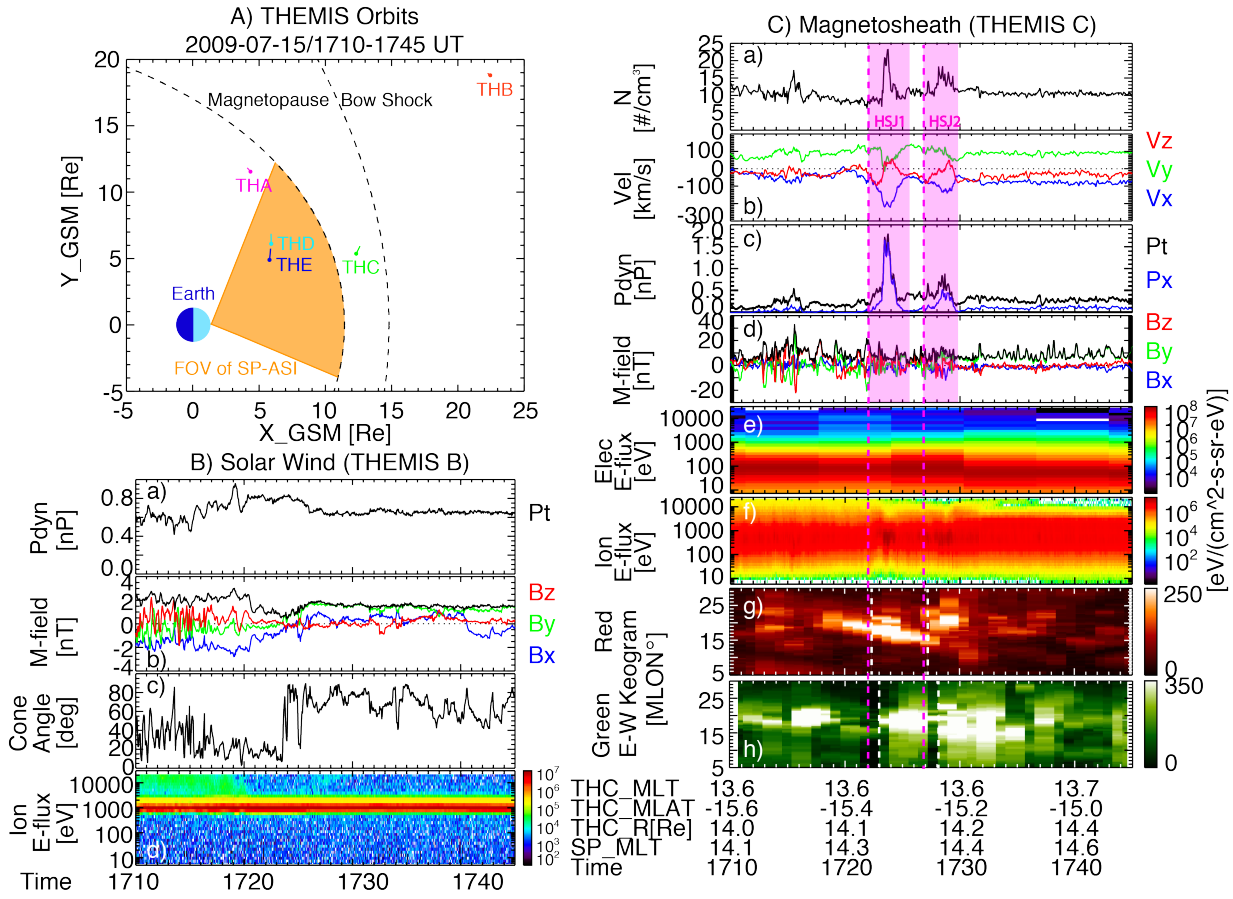

Figure 7.1 Panel (A) shows the orbits of the THEMIS satellites during 1600-1800 UT on 15 July 2009. The orange shade shows the longitude coverage of the field-of-view of the all-sky imager at South Pole station. The positions of magnetopause and bow shock are obtained from the *Shue et al.*, [1998] and *Wu et al.*, [2000] models. Panel (b) shows solar wind observation by THEMIS B during 1710–1750 UT. The panels shown are (Ba) dynamic pressure, (Bb) IMF in the GSM coordinates, (Bc) IMF cone angle, and (Bd) ion energy flux. Panel (C) shows the magnetosheath observations by THEMIS C during 1710-1750 UT. The panels shown are (Ca) plasma density, (Cb) flow velocity, (Cc) total (black) and GSM-X component (blue) of dynamic pressure, (Cd) magnetic field, (Ce) electron energy flux, (Cf) ion energy flux, and east-west keograms of (Cg) red-line and (Ch) green-line emissions. The magenta shades indicate two high-speed jets identified by *Plaschke et al.*, [2013] and the magenta dashed lines indicate their initiation times. The white vertical dashed lines show the beginning of auroral brightening.

Figure 7.1B shows solar wind conditions observed by THEMIS B during 1710-1745 UT. THEMIS B was ~29.3 Re away from the Earth, and the propagation time to the model bow shock was ~3 min. The variance of dynamic pressure was within 0.6 nPa without interplanetary

shocks around this period. IMF Bx increased negatively during 1715-1722 UT, and the corresponding IMF cone angle decreased to ~20°, which was in favor of the occurrence of magnetosheath HSJs [*Plaschke et al*., 2013].

Figures 7.1Ca-7.1Cf show magnetosheath observations by THEMIS C during 1710–1745 UT. Two HSJs were identified during ~1722-1726 UT and ~1727-1730 UT, which are indicated by magenta shades, and the magenta dashed lines show their initial times. They were both associated with increases in plasma density, antisunward flow velocity, and dynamic pressure. The dynamic pressure in the magnetosheath prior to the HSJs was ~0.2 nPa, while the dynamic pressure approached to 1.8 and 0.9 nPa, respectively, during the two HSJs. There were no HSJs or other notable disturbances for the preceding 15 min, and thus, this event allows us to examine if corresponding magnetospheric and auroral responses occur without contamination by other phenomena.

To compare to auroral activity, east-west keograms of red- and green-line emissions are shown in Figures 7.1Cg and 7.1Ch, respectively. There were two red-line auroral brightenings as indicated by the white dashed lines in Figure 7.1Cg, occurring around the two HSJs, respectively. The green-line emission keogram presents that the two most intense brightenings occurred within a minute after two HSJs. The green-line aurora also showed subsequent brightenings with ~5-min recurrence periods. This signature may indicate ULF waves excited by magnetospheric compression. The red-line emission keogram shows that the discrete aurora also brightened ~5 min after the first HSJ. Both discrete and diffuse auroral brightenings present eastward (duskward) motions. It is noted that there was another small increase in magnetic field and dynamic pressure at ~1712-1716 UT. This may be related to the preceding discrete and diffuse

auroral brightenings. This event, however, did not satisfy the HSJ criteria by *Plaschke et al.*, [2013] because of the small magnitudes.

THEMIS A and E were at ~12.9 and 8.4 Re away from the Earth in the dayside magnetosphere. Figure 7.2Ba shows two intensifications of whistler mode waves at 1723 and 1732 UT, which occurred a few minutes after the 2 HSJs. Considering that whistler mode waves can scatter plasma sheet particles into the loss cone, those waves are likely responsible for diffuse aurora observed in the ASI at South Pole (see below). Both THEMIS A and E observed significant increase in the GSM-Z component of the magnetic field soon after the occurrence of HSJs, in a similar manner to magnetospheric compression during an interplanetary shock. THEMIS A also observed significant ULF waves in both velocity and magnetic field. Those signatures indicate the magnetopause compression as the response of those two HSJs and support the inference from the green-line aurora data mentioned above. It is noted that THEMIS A, which was located at ~16.7 MLT, observed compressional signatures from ~1726 UT, which was ~3 min later than the similar signatures observed by THEMIS E, which was located at ~14.8 MLT. The longer delay at THEMIS A may be caused by duskward signal propagation lag. This is also indicated by the duskward motions of discrete and diffuse aurora. In addition, it is noted that the increase of detrended Bz at THEMIS E was much weaker than that at THEMIS A and significant ULF waves can only be observed at THEMIS A. This indicates that only a small portion of energy propagated earthward to the THEMIS E location and thus that HSJ effects predominantly occurred in the outer magnetosphere.

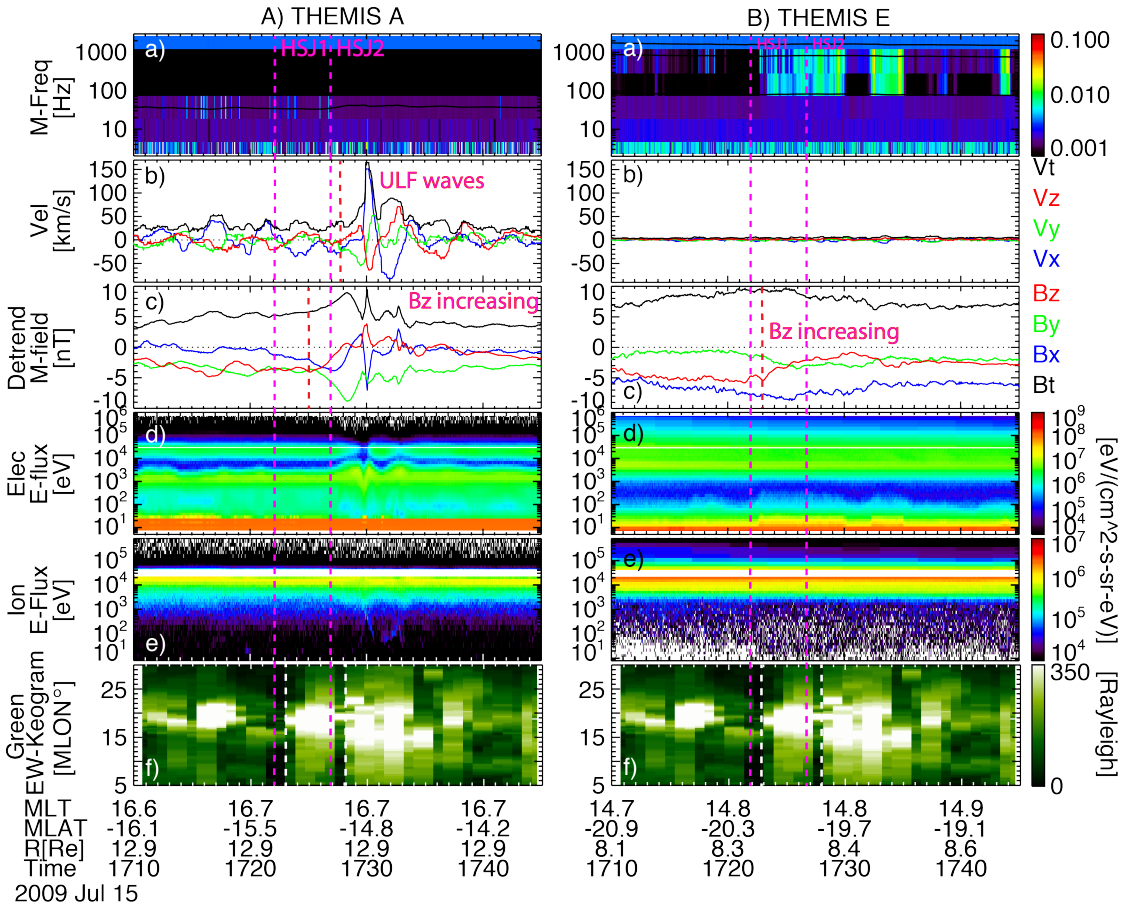

Figure 7.2 Magnetospheric observation by (A) THEMIS A and (B) THEMIS E during 1710–1750 UT on 15 July 2009. Panels (Aa-Ae) show magnetic field wave spectra, flow velocity, magnetic field after subtracting the T01 model, and electron and ion energy fluxes observed by THEMIS A. Panels (Ba-Be) are the same format as Panels (Aa-Ae) except for THEMIS E. Panels (Af) and (Bf) show the east-west keogram of green-line emission during the same period.

Figure 7.3 combines the observation in the magnetosheath, magnetosphere, and aurora. It is clear that magnetospheric compression seen in the GSM-Z component of the detrended magnetic field occurred during 1723 through 1735 UT, starting within 2 min after the occurrence of the two HSJs. A secondary increase in detrended Bz may exist at ~1729 UT as a response to the second HSJ. Here the secondary increase is not clearly seen. It is possible that at the location of THEMIS-E, two compressional signals, which were generated by two HSJs, were overlapped with each other and formed one increase in Bz. Within 3 min of the occurrence of the HSJs, both

diffuse aurora and discrete aurora brightened. Here the responses of magnetosphere and aurora are highlighted by the blue arrows in Figure 7.3. The brightening in red-line emission appears to have started slightly (~1 min) before the brightening in green-line emission, but this may not be significant due to the limited time resolution of ASI (~44 s). The clear correlated signals present a significant response sequence in the magnetosphere and aurora to HSJs.

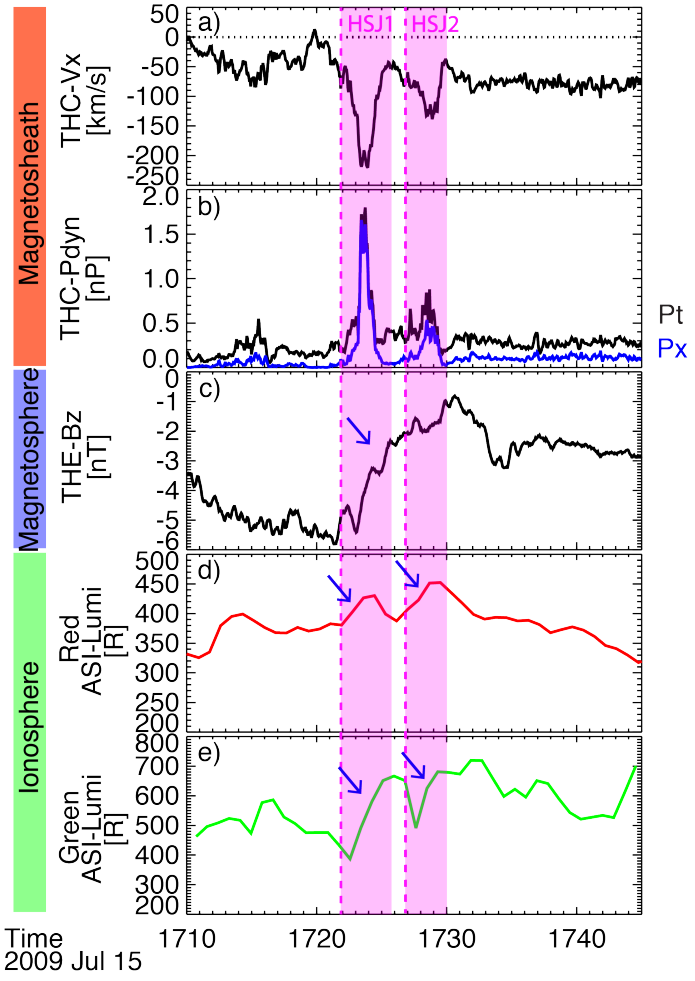

Figure 7.3 Combined observation data from THEMIS C, THEMIS E, and South Pole. Panels (a) and (b) show the GSM-X component of flow velocity and dynamic pressure in the magnetosheath by THEMIS C. Panel (c) shows the GSM-Z component of detrended magnetic field in the magnetosphere by THEMIS E. Panels (d) and e show the auroral luminosities averaged over 10–30° MLON of the keograms shown in Figure 7.1g and 7.1h, respectively. Here the magenta dashed lines and shades highlight the same signatures as seen in Figure 7.1.

Since the auroral responses have been identified in keograms, we can further take advantage of 2D optical observation of discrete and diffuse auroral brightening patterns. Figure 7.4 shows the first brightening of diffuse aurora. Figures 7.4a-7.4d present the green-line snapshots. The FOV was dark at 1725:06 UT (Figure 7.4a), and then a localized brightening appeared near the center of the imager FOV at 1724:15 UT (Figure 7.4b). The lack of arcs or rays suggests that this was diffuse aurora. This aurora propagated duskward (Figures 7.4b-7.4d). To quantify the size and propagation, we identified the boundary of the auroral structure and plotted it in Figures 7.4e-7.4g. The boundary of the structures is identified as 1/e of the peak luminosity above the background, indicated by the yellow contour lines. The east-west width of the brightening pattern varied from 474 to 488 km. The pattern propagated duskward with an average east-west velocity of 1.5 km/s. Here the velocity of the brightening pattern is defined as the velocity of the centroids of the identified patterns. Figures 7.4h-7.4j show the mapped patterns of the identified brightening patterns on the equatorial plane by the T01 model. The azimuthal size (in GSM-Y direction) of the pattern varied from 2.0 to 2.7 Re, which was larger but still comparable to the size of the HSJs, which was ~0.93 Re [*Plaschke et al*., 2016]. The duskward velocity of the pattern was 43.5 and 52.6 km/s at 1725:06 and 1725:57 UT, respectively. It is noted that both the magnitude and the direction of the velocity were consistent with background velocity of the magnetosheath flow (Figure 7.1Cb), indicating that the motion of the magnetopause compression that drove the diffuse aurora is probably controlled by background magnetosheath flows.

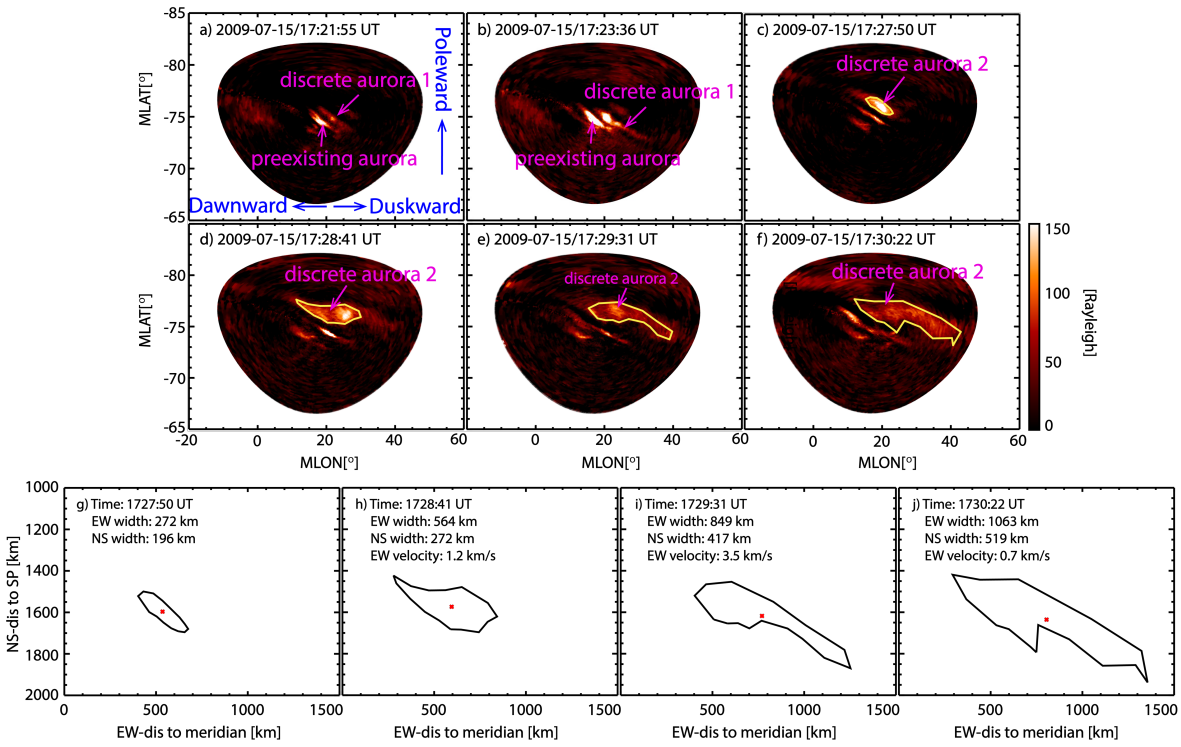

Figure 7.4 Panels (a-d) show the first brightening pattern of diffuse aurora in green-line emission at 1722:34, 1724:15, 1725:06, and 1725:57 UT on 15 July 2009. The x and y axes show magnetic longitude and latitude. The yellow contour lines identify the first brightening pattern of diffuse aurora. Panels (e-g) show the shapes of the contour lines at the altitude of ~110 km at 1724:15, 1725:06, and 1725:57 UT, respectively. The x axis shows the distance to an arbitrary reference meridian, and the y axis shows the distance to magnetic South Pole. Panels (h-j) show the mapped patterns on the equatorial plane by the T01 model at 1724:15, 1725:06, and 1725:57 UT, respectively. The dashed curves indicate the position of the model magnetopause calculated by the *Shue et al*., [1998] model.

It is noted that in Figures 7.4b-7.4d, the peak intensity is confined between 15° and 20° MLON and did not propagate substantially, although the entire diffuse auroral pattern propagated eastward as described above. The east-west keograms in Figure 7.1Ch also show that the duskward front of this brightening pattern had a clear duskward motion, while the peak intensity was nearly stationary. An implication of this result is that the peak intensity probably corresponds to the initial contact longitude of the HSJ to the magnetosphere, which stays most intense, while the signal spreads azimuthally over time with the magnetosheath background

flows and fast mode waves in the magnetosphere. Thus, the entire brightening pattern propagated eastward.

Figures 7.5a-7.5f show 2D red-line snapshots. The arc-like extended structures indicate that this was discrete aurora. The magenta arrows marked two discrete auroral patterns, which were probably related to the two HSJs. The discrete auroral pattern, which is marked by "discrete aurora 1", occurred near the preexisting red-emission aurora, right after the occurrence of the first HSJ at ~1722 UT (Figure 7.5a). It extended duskward in the next snapshot (Figure 7.5b). "Discrete aurora 2" occurred at ~1727 UT, right after the second HSJ, and extended duskward significantly in the subsequent snapshots. Since no auroral structures exist poleward of those, these were likely located near the open-closed boundary. In fact, the T01 model put those auroral patterns on open field lines. Since discrete aurora 1 may not be fully distinguishable from the preexisting red-emission aurora, we mapped discrete aurora 2 to the ionosphere, and Figures 7.5g-7.5j show that the east-west width of the second discrete auroral patterns in the ionosphere varied from 272 to 1,063 km. The discrete aurora also had a clear duskward motion with a velocity of ~0.7 km/s in the ionosphere. The direction of the motion was consistent with both the motion of diffuse auroral brightening pattern and GSM-Y component of magnetosheath background flow. The propagation of the localized discrete aurora was seen for a longer duration over a longer distance than was the diffuse aurora.

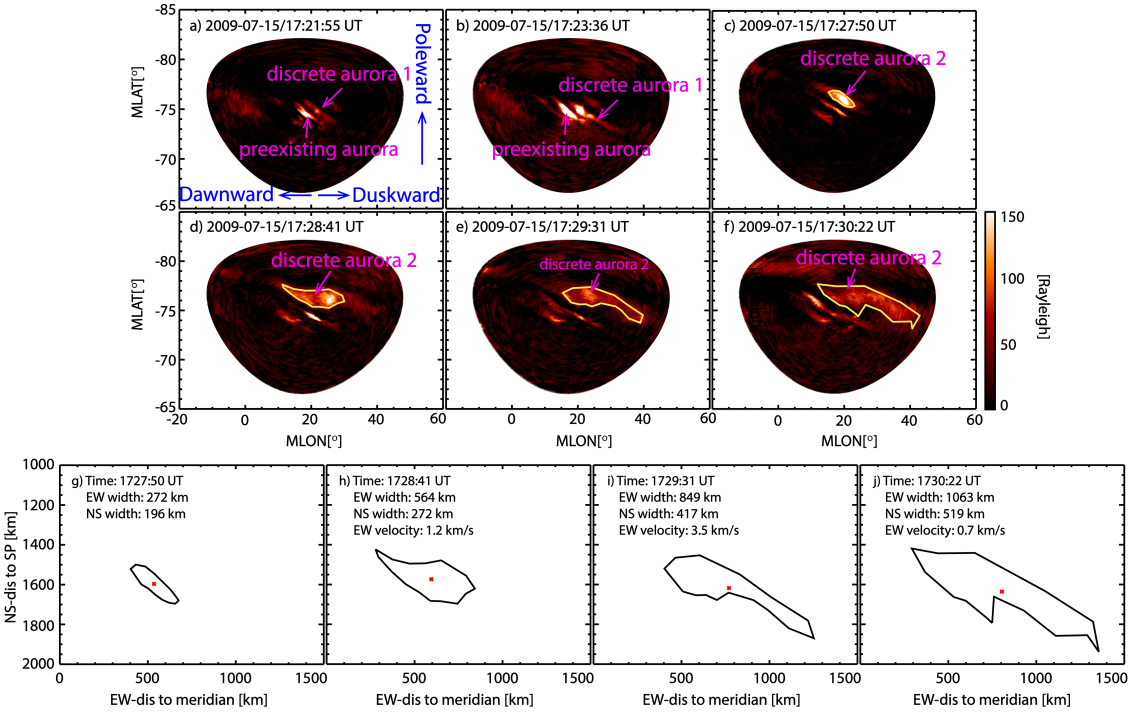

Figure 7.5 Six snapshots at (a) 1721:55, (b) 1723:36, (c) 1727:50, (d) 1728:41, (e) 1729:31, and (f) 1730:22 UT of green-line emission data highlighting discrete aurora. The x and y axes show magnetic longitude and latitude. The yellow contour lines identify the brightening pattern of discrete aurora. Panels (g-j) show the corresponding patterns in the ionosphere at ~230 km at 1728:41, 1728:41, 1729:31, and 1730:22 UT, respectively. The x and y axes show their distance to magnetic South Pole and to the reference meridian, respectively.

7.2.2 Second Case: 17 July 2009

Another event period, which contains two identified HSJs during 1710–1800 UT on 17 July 2009, is different from the previous case in that both brightening and dimming are observed in diffuse auroral intensity.

During this period, the center of the South Pole station imager FOV was at ~14.5 MLT. The THEMIS satellites were located in the solar wind, the magnetosheath and the magnetosphere within the longitude range of the FOV of the ASI at South Pole station on the dayside (as shown in Figure 7.6a). This is also an ideal configuration to examine the solar wind-magnetosheath-magnetosphere interaction during HSJs.

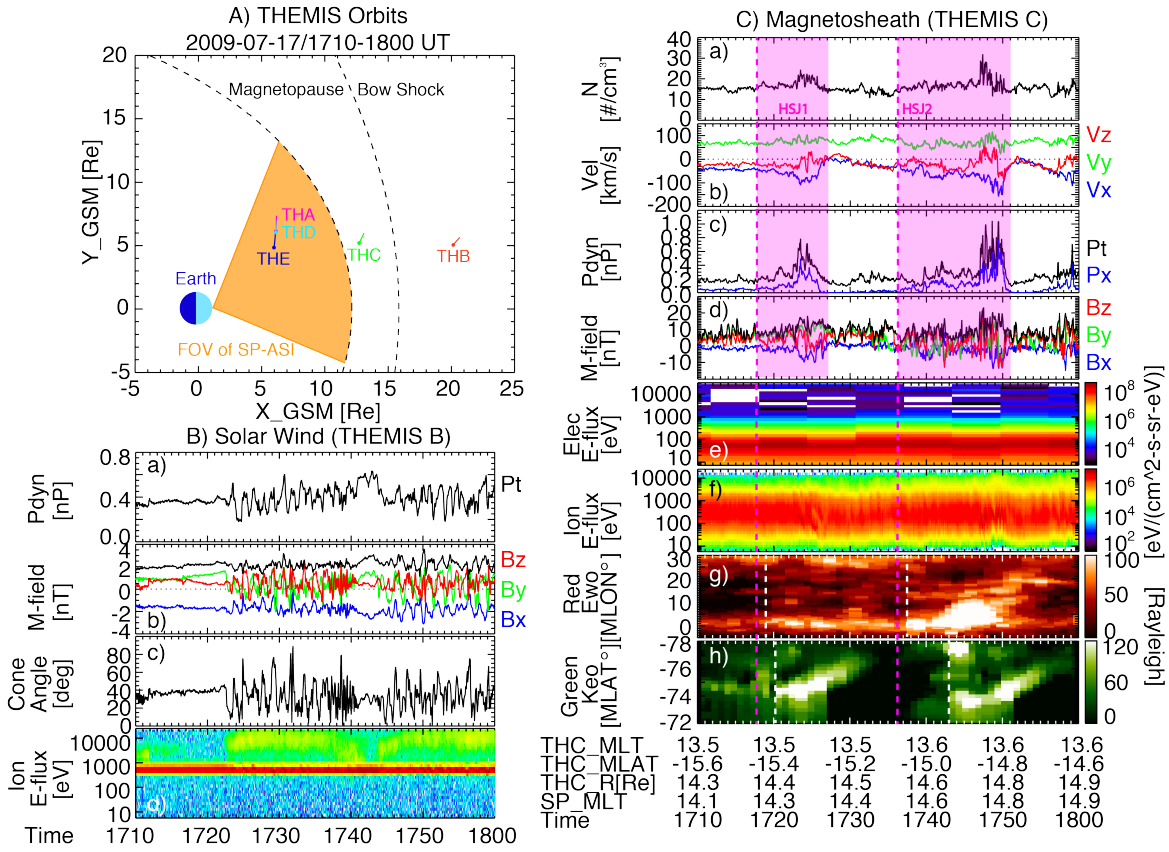

Figure 7.6 The same format as in Figure 7.1, except that the high-speed jet event is during 1710-1800 UT on 17 July 2009 and Panel (h) shows east-west keogram of green-line emission.

Figures 7.6B and 7.6C present the information in the same format as Figure 7.1. THEMIS B was ~21 Re away from the Earth in the foreshock, and the propagation time of the observed solar wind structure to the model bow shock was ~1 min. The variance of dynamic pressure was within 0.5 nPa without interplanetary shocks. And the averaged magnetic field almost unchanged. The periodic oscillation of the dynamic pressure and magnetic field during this time period was due to the backstream superthermal ions interacting with solar wind in the foreshock. The cone angle was on average less than 40° during this period, which was favorable for occurrence of HSJs.

In the magnetosheath, THEMIS C observed two HSJs during ~1718-1727 UT and ~1736-1751 UT, respectively. They were both associated with enhancements of the plasma density, enhanced GSM-X component of flow velocity and dynamic pressure. The background dynamic pressure in the magnetosheath during this period was ~0.1 nPa, while due to these two HSJs, dynamic pressure approached 0.8 and 1.0 nPa. Interestingly, the X component of the dynamic pressure after each HSJ decreased to below the pre-HSJ level, approaching nearly 0 nPa. Such dynamic pressure reductions were not seen in the solar wind, and thus, those may be an after-effect of HSJ creations at the bow shock.

The auroral activity is shown by the east-west red-line and north-south green-line keograms in Figures 7.6Cg and 7.6h, respectively. The red-line keogram presents a significant brightening and duskward motion of discrete aurora occurring within ~1 min after the second HSJ. There was also a weak brightening of discrete aurora following the first HSJ, although it was too dim to identify its propagation. The green-line keogram presents two diffuse auroral brightenings within ~4 min following the occurrence of the HSJs. These two diffuse auroral brightenings both propagated poleward significantly, which is different from the first case shown above. The poleward propagation indicates that the diffuse aurora is not caused simply by enhanced pitch angle scattering by fast-mode compression (which should propagate equatorward) but is analogous to motion of FACs associated with Alfven waves converted from fast-mode waves. As shown by [*Chi et al*., 2006], the *Tamao* [1964a; 1964b] propagation paths lead to poleward propagation of Alfven waves (FACs) as a result of travel-time effects. Precipitating electrons carrying the upward FAC portion of this current system would explain the measured poleward propagation. The reason for being diffuse rather than discrete aurora is because the density at low L-shells is generally high enough to carry FACs without requiring parallel

potential drop [Lee et al., 2011]. It is also noted that these two diffuse auroral brightenings were both followed by dimmings compared to auroral intensity during the pre-HSJ interval, which were consistent with decreases of the x component of the dynamic pressure after the HSJs. This indicates that the magnetosheath pressure controls the intensity of dayside diffuse aurora through magnetopause compression and that the magnetosheath pressure variations can be substantially different from the solar wind.

Since the first brightening of discrete aurora is difficult to identify, we focus on the second brightening of discrete and diffuse aurora. The green-line 2D snapshots in Figures 7.7a-7.7d show the patterns of the second diffuse auroral brightening. The FOV was dark at first, and then an intense brightening of diffuse auroral pattern showed up at 1749:27 UT (Figure 7.7b) and the brightening was centered at ~6° MLON. The following snapshots show a poleward motion of this diffuse auroral brightening with an azimuthal extension in both the dawnward and duskward directions. Westward propagation existed, but it is not clear how the eastern edge of the brightening evolved because of the limited size of the FOV.

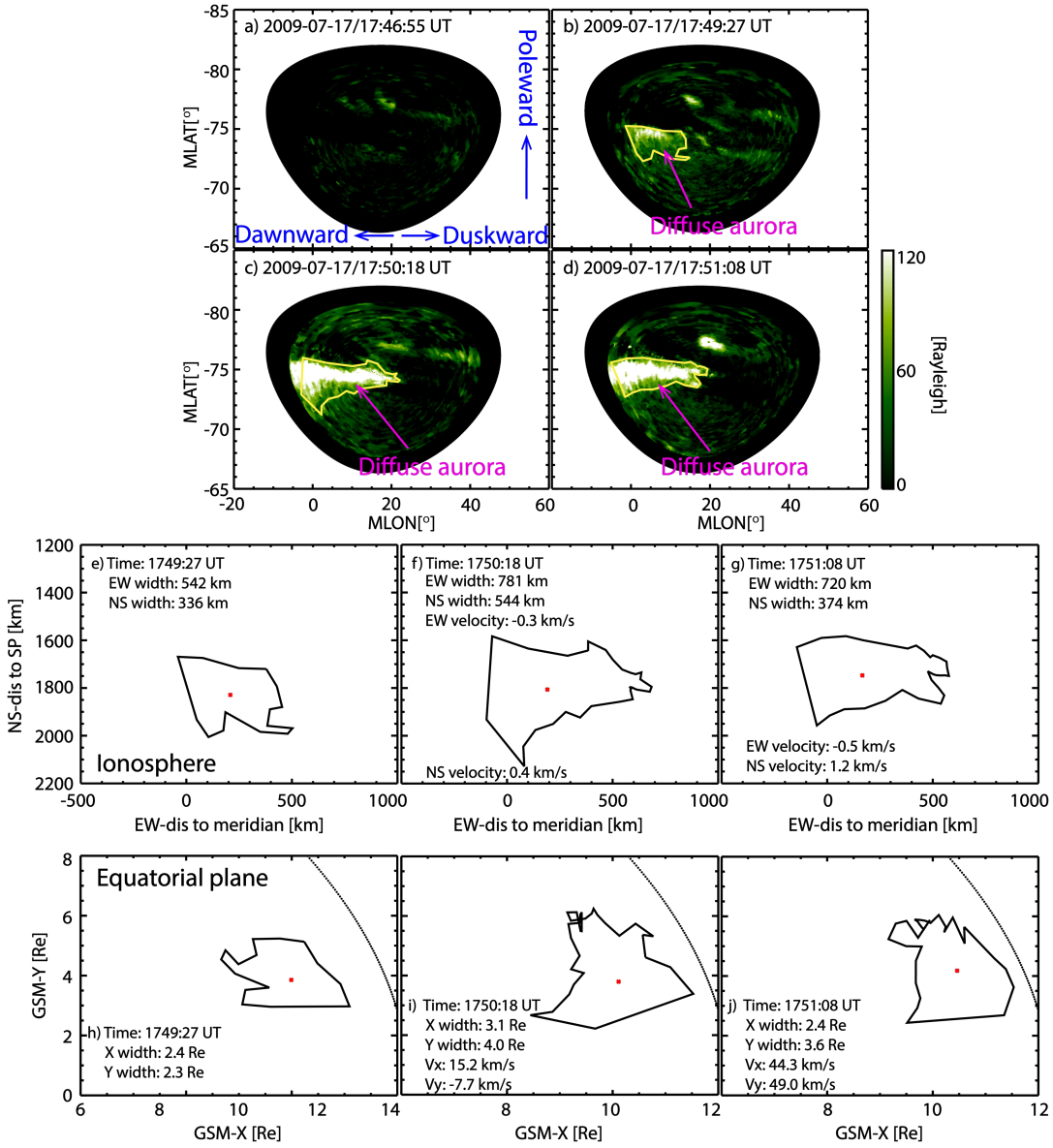

Figure 7.7 The same format as in Figure 7.4, except for the 17 July 2009 event.

Figures 7.7e-7.7g present the diffuse auroral shape in the ionosphere, showing that the east-west width of the identified pattern extended from ~542 to ~781 km. It propagated poleward at 0.4 and 1.2 km/s at 1750:18 and 1751:08 UT, respectively, while the estimate of the east-west propagation is not accurate due to the limited FOV. Figures 7.7h-7.7j show that the azimuthal

size (in GSM-Y direction) of the auroral shape mapped to the equator extended from ~2.3 to ~4.0 Re, which may be slight underestimate due to the limitation of the FOV.

Figures 7.8a-7.8f present the snapshots of the red-line emission. The FOV of the ASI at South Pole station was dark at first and then a bright discrete auroral pattern showed up at ~9° MLON and propagated duskward for ~5 min. The east-west widths of these brightening patterns in the ionosphere are ~245–253 km (Figures 7.8g-7.8i). The duskward motion is seen at a speed of ~0.4 km/s. An additional discrete aurora with smaller intensity was presented at ~35° MLON at 1747:58 UT. It merged with the existing discrete auroral brightening and continued to extend duskward. Similar to the previous case, this azimuthal motion is consistent with the GSM-Y component of magnetosheath background flow.

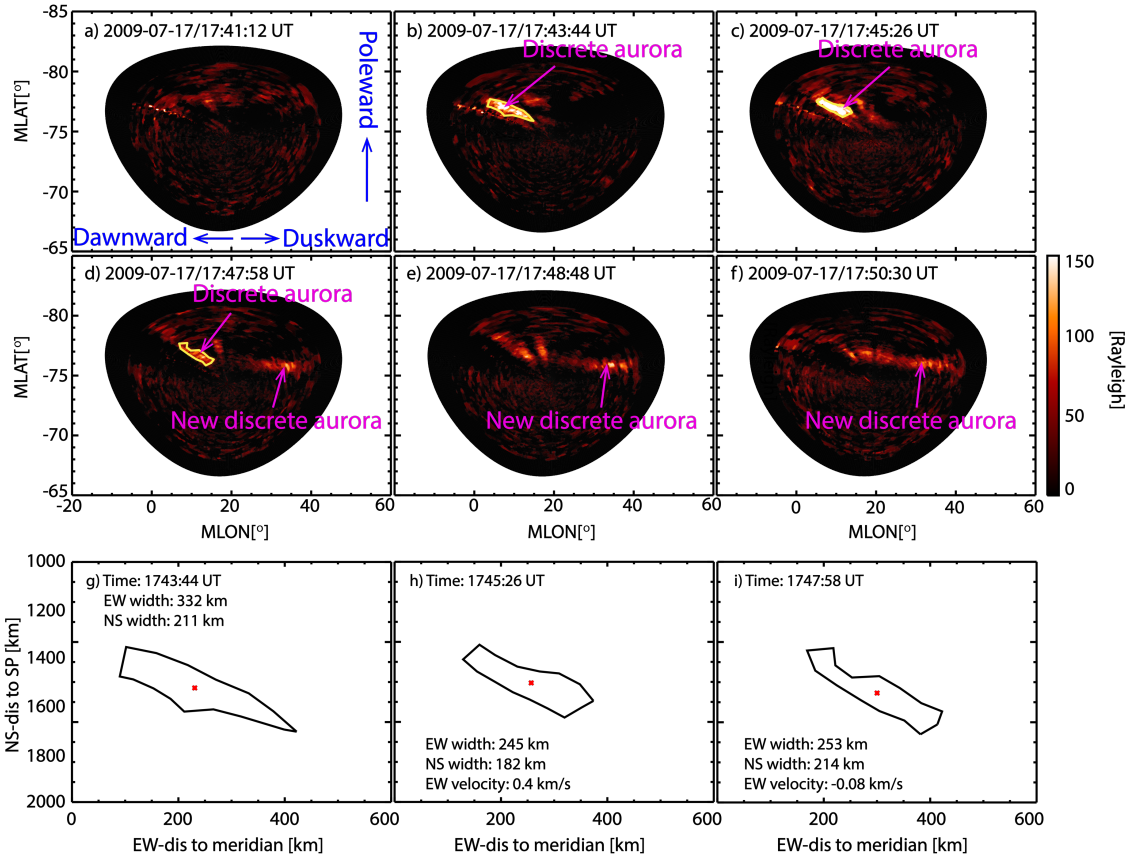

Figure 7.8 The same format as in Figure 7.5, except for the 17 July 2009 event.

7.3 Multicase Study

In order to examine the average 2D properties of HSJ effects on M-I coupling system, a multicase study is done based on the eight HSJ events identified according to the selection criteria mentioned in section 7.1. The details of these events are listed in Table 7.1. It presents that the THMEIS satellites in the magnetosphere observed significant ULF waves in five cases, indicating magnetospheric compression. Furthermore, all those ULF signatures were only identified by one of the satellites. This indicates that, unlike SC-induced magnetospheric compression, the HSJ-related compression is localized. Thus, to capture the compression signature, satellites need to be close enough to the HSJ. This may explain that ULF signatures are not observed in the other six cases due to satellite location.

Table 7.1 Eleven Selected HSJ Events

Date	Timing of HSJs [UT]	Ave Vy of flow in M' sheath [km/s]	Initial time of diffuse auroral brightening [UT]	Max size (diffuse aurora) in ionosphere [km]	Average Vy in the ionosphere [km/s]	Max size on the equatorial plane [Re]	Average Vy on the equatorial plane [km/s]	ULFs	Localized ULF
2008-06-30	1526:14 - 1552:36	86.7	1533:13	1275	0.1±0.8	6.5	5.0±19.1	no	-
			1545:27	904	1.1±1.9	5.5	42.2±65.6	no	
2009-07-01	1535:32 - 1539:50	55.6	1535:13	1162	1.7±1.9	6.7	71.3±74	Yes	Yes
			1542:08	855	3.6±0.1	4.0	174.1±7.9		
2009-07-01	1642:02 - 1642:58	62.2	1642:08	746		3.6	-	-	-
2009-07-	1635:48 -	83.2	1641:59	367	0.1±0.1	2.1	10±15.6	Yes	Yes

15	1639:48								
2009-07-15	1723:27 - 1728:29	89.1	1724:15	488	1.5±0.7	1.7	48.1±4.6	Yes	Yes
			1728:29	845	1.0±1.0	2.1	43.6±14.9	Yes	Yes
2009-07-17	1723:30	67.8	1723:15	980	1.0±2.1	5.4	41.0±45.5	Not fou-nd	-
2009-07-17	1749:28 - 1759:07	67.8	1748:36	720	2.3±1.1	4.0	70.0±23.0	Not fou-nd	-
2009-07-23	1634:28 - 1649:14	53.2	1641:12	871	0.7±0.5	3.0	16.8±14.6	Yes	Yes
			1653:53	463	-	2.6	-	-	
Ave		71	-	806	1.3	3.7	+52.3		

Note: The columns show the date and periods of HSJs in each events, the GSM-Y component of magnetosheath flow, initiation time of diffuse auroral brightening, maximum size of the diffuse aurora mapped to the equator, average GSM-Y component of optical propagation velocity in the ionosphere and the equatorial plane, the propagation direction of the diffuse auroral brightening patterns, the existence of ULF waves, and the existence of localized ULF waves.

Table 7.1 also shows that HSJs are associated with both diffuse and discrete aurora in all of eight events. The average size of the diffuse auroral brightening patterns in the ionosphere is ~800 km in the east-west direction, and the corresponding average velocity is ~2.4 km/s eastward (duskward). The average azimuthal width of these diffuse auroral brightening patterns on the equatorial plane is ~3.7 Re, and the average velocity in the GSM-Y direction is ~57 km/s. For comparison, the GSM-Y component of magnetosheath background flows is calculated as the average velocity of a 10-min period near the HSJs. The average background Vy in the magnetosheath is ~71 km/s in these cases, which is close to the average Vy of the diffuse auroral brightenings. The consistency between the auroral propagation and the magnetosheath background flow indicates that the background flow in the magnetosheath probably pushes the compressed region of the magnetopause to propagate azimuthally.

The only exception is that no diffuse aurora was seen in the ASI at South Pole in the HSJ event on 4 July 2008, and there were no significant compression signals shown by the satellites in the magnetosphere. However, similar to other HSJ events, the discrete aurora significantly brightened associated with the HSJs in this event. While it is not clear why the diffuse auroral signal was absent, it is noted that the HSJ property was different from the other events. The enhanced dynamic pressure of the HSJ in this event was due to a density enhancement, while Vx decreased. The difference in the HSJ property may affect how the magnetopause is affected by the enhanced pressure.

In Table 7.1, optical velocity is not estimated for three diffuse auroral brightening events (1 July 2009, the second case on 17 July 2009 and 23 July 2009). In the case on 1 July 2009, it is because the brightening only lasted for one snapshot. In the other two cases, one of the boundaries of the diffuse auroral brightening was out of the FOV, which made the optical velocity to be unreliable. However, similar to what described about the case on 17 July 2009 in the case study section, on 23 July 2009, a significant duskward propagation and extension also showed up in the red-line emission, which was consistent with the direction of the corresponding magnetosheath flow.

7.4 Discussion

In most cases, we have examined that both discrete and diffuse aurora respond to magnetosheath HSJs. This auroral behavior is similar to the "shock aurora", which is the response to interplanetary shocks/sudden commencements (SCs). For "shock aurora", the diffuse aurora and discrete aurora are considered to be signatures corresponding signatures of the currents during preliminary impulse and main impulse [*Motoba et al.*, 2009; *Nishimura et al.*,

2016]. Recent studies have shown that the foreshock transients can provide geospace effects similar to interplanetary shocks/SCs [*Engebretson et al*., 2013]. While the lack of magnetosheath measurements in those studies did not allow evaluation of how foreshock disturbances affect the magnetopause. The magnetosheath observations in the present paper show the direct triggers of these similar magnetospheric and auroral responses. Based on the multicase analysis, the localized magnetospheric compression and shock-aurora-like auroral brightenings are probably related to the magnetosheath HSJs, which are modified by the foreshock disturbances.

HSJ-related flow shears or traveling convection vortices (TVCs) caused by the magnetopause compressions can build up FACs near the magnetopause [*Crowley et al*., 2000; *Fujita et al*., 2003]. Upward FACs are associated with enhanced electron precipitation, forming localized discrete auroral brightening. HSJs in the magnetosheath can compress the magnetopause, inducing ULF waves in the magnetosphere [*Hietala et al*., 2012]. Magnetospheric compression is expected to increase electron's anisotropy and energy, thus potentially enhancing the growth rate of whistler mode waves that scatter electrons from the plasma sheet to the ionosphere. Those two processes are shown in Figure 7.9. Since diffuse auroral brightening highlights the compression region in the magnetosphere, the boundary of the brightening pattern probably extends outward due to the radial propagation of the compressional wave signals. Thus, the azimuthal sizes (~3.7 Re) of their mapped patterns on the equatorial plane may be slightly larger than the widths of the corresponding HSJs (~1 Re; *Plaschke et al*., 2016). Instead of measuring the azimuthal size of HSJs, the azimuthal size of diffuse auroral patterns describes the localized geoeffective regions that are triggered by HSJs.

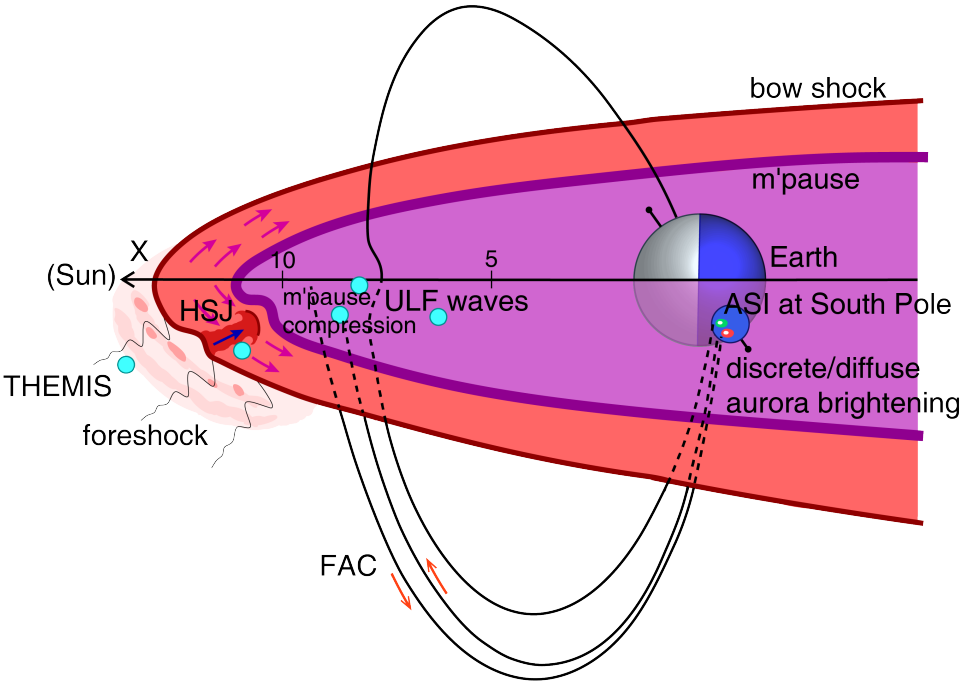

Figure 7.9 Illustration of the HSJs' impacts on the dayside magnetosphere and aurora.

The azimuthal propagation of aurora indicates that the upward FACs and compression signature have a corresponding azimuthal motion. Based on the multicase analysis, most cases show good agreement between magnetosheath background flows and the propagation of the HSJ-related diffuse/discrete auroral brightening patterns. This may indicate that the GSM-Y component of magnetosheath flow (shown by the magenta arrows in the magnetosheath in Figure 7.9) pushes the magnetopause deformation to propagate azimuthally.

Recently, *Han et al.*, [2016, 2017] showed that dayside throat aurora, which is a type of discrete aurora that penetrates from the dayside auroral oval to lower latitudes, also prefer to occur under the condition of low cone angle. They suggested that HSJs are a likely cause of throat aurora. However, in our HSJ events, throat aurora was absent, and instead, the discrete auroral responses to the HSJs were the brightenings within the auroral oval without penetrations toward lower latitudes. While the connection between HSJs and throat aurora is not observed in

our data set, it could be interesting to examine how throat aurora relates to the features we have observed.

7.5 Conclusion

This study presents magnetospheric and auroral responses to magnetosheath HSJs based on the coordinated observation between the THEMIS satellites and the ASI at South Pole station during 2008 through 2010. All of eight HSJ events exhibited clear association between magnetosheath HSJs and discrete/diffuse auroral brightenings, and in five events, the magnetosheath HSJs were accompanied by magnetospheric compressions. Using those auroral responses, we were able to determine location, size, and motion of HSJ-magnetosphere interaction that are difficult to measure by other means. The discrete and diffuse auroral brightenings occurred in a similar manner to shock aurora, except for a smaller size: The patterns of the diffuse auroral brightenings mapped to the equatorial plane show an azimuthal width of ~3.7 Re, which characterizes the geoeffective scale of HSJs. In addition, the azimuthal velocities of those mapped patterns show good consistency with the GSM-Y components of the magnetosheath background flows. This indicates that the compressed region of the magnetopause propagates azimuthally following the background magnetosheath flows.

Furthermore, it is noted that the intensity variance of diffuse aurora shown in the second case in the case study section is positively correlated with the GSM-X component of the dynamic pressure in the magnetosheath for both pressure increases and decreases, in an absence of IMF and solar wind dynamic pressure variations. This indicates that the dayside diffuse aurora can be directly modified by the dynamic pressure changes in the magnetosheath.

In summary, although magnetosheath HSJs are localized disturbances, they are quite geoeffective, including triggering ULF waves in the magnetosphere and discrete/diffuse auroral brightenings, similar to interplanetary shocks except that the HSJ-related responses are localized. Additionally, the discrete auroral brightenings likely reflect significant FACs, which are associated with a corresponding electric field enhancement, further demonstrating the MI coupling driven by HSJs.

Chapter 8

2D structure of foreshock-driven Pc5 ULF waves

In this chapter, two series of Pc5 ULF waves, which were driven by foreshock disturbances on June 29, 2008, were determined in a 2D perspective, by using the coordinated observation of the THEMIS satellites and the ASI at South Pole. Section 8.1 presents the instruments that are used in this study; Section 8.2 shows the observation of the first series of Pc5 ULF wave; Section 8.3 the observations of the second series of Pc5 ULF wave; Section 8.4 and 8.5 present a discussion and a conclusion, respectively.

8.1 Instrument locations for the conjunction events

This study uses the THEMIS satellite to observe the upstream activities and their corresponding responses in the magnetosphere, and the monochromatic ASI at South Pole station in Antarctica to identify dayside discrete and diffuse aurora.

During 1520 through 1630 UT and during 1650 through 1820 UT on June 29, 2008, THEMIS B and C were in the dayside solar wind, near the bow shock, while THEMIS A, D, E were in the dayside magnetosphere. The THEMIS satellites observations are thus used to observe the upstream activities and their corresponding responses in the magnetosphere. By mapping to equatorial plane through the T01 model, the FOV of the ASI at South Pole covers an area that swept across noon during the same period (Figure 8.1). It is clear that the FOV has a good

conjunction with all the THEMIS satellites, which is benefit to identify the auroral responses to the upstream disturbances.

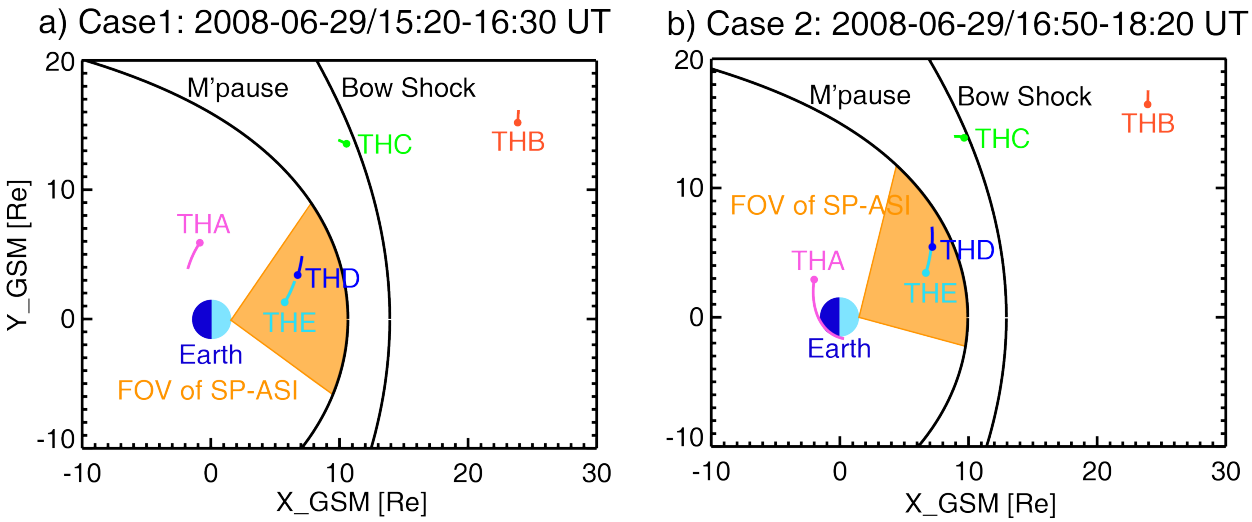

Figure 8.1 The orbits of the THEMIS satellites during (a) 1520-1630 UT and b) 1650-1820 UT on June 29, 2008. The orange shade shows the longitude coverage of the FOV of the ASI at South Pole station. The positions of magnetopause and bow shock are obtained from the *Shue et al*., [1998] and *Wu et al*., [2000] models.

Ground-based magnetometers at IQA, STF, B10 and B23 are also utilized to analyze ionospheric wave signatures, and compare with the optical observation.

8.2 The first Pc5 ULF wave: 1545-1610 UT on June 29, 2008

8.2.1 Upstream observation

During 1520 through 1630 UT on June 29, 2008, THEMIS B and C were in the solar wind (Figure 8.1a), ~30.5 Re away from the Earth and at ~14.2 MLT for THEMIS B, and ~18.0 Re away from the Earth and at ~15.5 MLT for THEMIS C. Figure 8.2 shows the IMF, wavelet analysis of total magnetic field, IMF cone angle, flow velocity, ion energy flux, dynamic pressure and the wavelet analysis of dynamic pressure, measured by THEMIS B (Figure 8.2a-

8.2g) and C (8.2h-8.2n). The pink shades highlight a foreshock transient occurring during ~1533 through 1603 UT. The foreshock transient is characterized by a significant depression in total magnetic field and large-amplitude oscillation, and slight total magnetic field increases at the edges. Figure 8.2c shows that during this time interval, the cone angle decreased to ~10° in minimum (~20-30° on average) from a background of ~45°. The small cone angles indicate that the IMF at the satellite location was likely connected to the bow shock, causing ions being reflected and accelerated. Superthermal ions were observed within this foreshock transient (Figure 8.2e, >~5 keV). Those observed features are consistent with a foreshock cavity [*Thomas & Brecht*, 1988] and also a proto-HFA [*Zhang et al*., 2010]. Figure 8.2f shows that the oscillations of the magnetic field and dynamic pressure in the foreshock transient was stronger than the background. The oscillation had ~250-350s periodicity, which was in the Pc5 frequency range (Figure 8.2b and 8.2g).

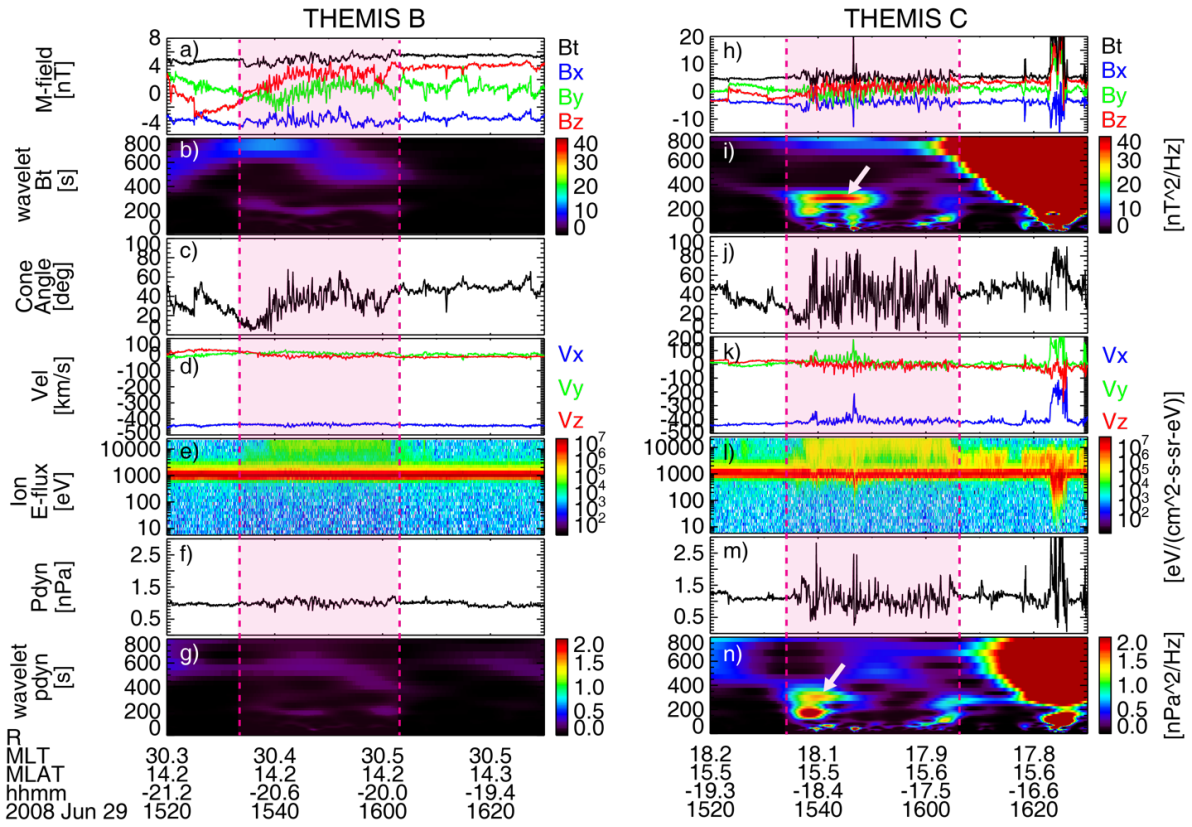

Figure 8.2 Solar wind observation by THEMIS B (Panels [a-g]) during 1520-1630 UT on June 29, 2008. Panels show (a) IMF, (b) wavelet analysis of total magnetic field, (c) IMF cone angle, (d) flow velocity, (e) ion energy flux, (f) dynamic pressure and (g) wavelet analysis of dynamic pressure. Here, IMF and flow velocity are in GSM. Panels (h-n) show the same format of panels (a-g), except for THEMIS C. The pink shades highlight the foreshock transient in this case.

Figures 8.2h-8.2n show the same format of data of Figure 8.2a-8.2g except for THEMIS C. The foreshock transient was observed during ~1534 through 1607 UT with similar features as detected by THEMIS B except for larger amplitudes: a) Its total magnetic field decreased in the core and increased at the edges; b) Its cone angle decreased to ~10-20° from a background of ~45°; c) It was filled with superthermal ions. THEMIS C observed much stronger perturbation in dynamic pressure oscillations during this foreshock transient. A significant dynamic pressure increase of ~0.7 nT was at the leading edge of the foreshock transient at ~1537 UT. Figure 8.2i and 8.2n present an intense ULF wave with a 250-350s period in total magnetic field and

dynamic pressure, respectively. This ULF wave was inside the foreshock transient and adjacent to its leading edge. It is noted that THEMIS C (closer to the bow shock) observed stronger signals than THEMIS B and such pressure variations did not exist in the OMNI data (https://omniweb.gsfc.nasa.gov/; not shown) in the pristine solar wind. It supports the idea that these are foreshock features created by interaction with the bow shock rather than structures originating in the solar wind.

8.2.2 Pc5 ULF waves in the dayside magnetosphere

THEMIS D was located at ~(6.9, 4.1, -3.5) Re in GSM, ~8.8 Re away from the Earth and at ~14.0 MLT in the dayside magnetosphere (Figure 8.1a). THEMIS E was at ~(6.1, 2.1, -2.9) Re, ~7.0 Re away from the Earth and ~13.2 MLT. Figures 8.3a-8.3j and 8.3k-8.3t show magnetic field after subtracting the T01-model field, wavelet spectra of field-aligned (Bp), azimuthal (Ba) and radial (Br) magnetic field, electric field, wavelet analysis of azimuthal (Ea) and radial (Er) electric field, electric field wave spectra, and electron and ion energy fluxes, measured by THEMIS D and E. Figure 8.3a shows a significant (~10 nT) increase in Bp observed by THEMIS D at ~1543 UT, which indicates a magnetospheric compression. Figure 8.3i shows an increase in electron energy flux right after ~1548 UT, observed by THEMIS D. It is a common signature of magnetospheric compression [*Zhou et al*., 2015]. During 1542-1553 UT, THEMIS E also observed the compressional signature of ~5 nT increase in Bp. This magnetospheric compression occurred ~5 min after the observation of the compressed leading edge of the foreshock transient by THEMIS C. Considering the lack of any other upstream changes, it indicates that the magnetosphere was compressed by the foreshock transient. Besides, the wavelet spectrum power of Bp shows a peak with a period of >300 s during the compression. It

is likely that the compressed leading edge of the foreshock transient also generated a compression wave propagating in the dayside magnetosphere.

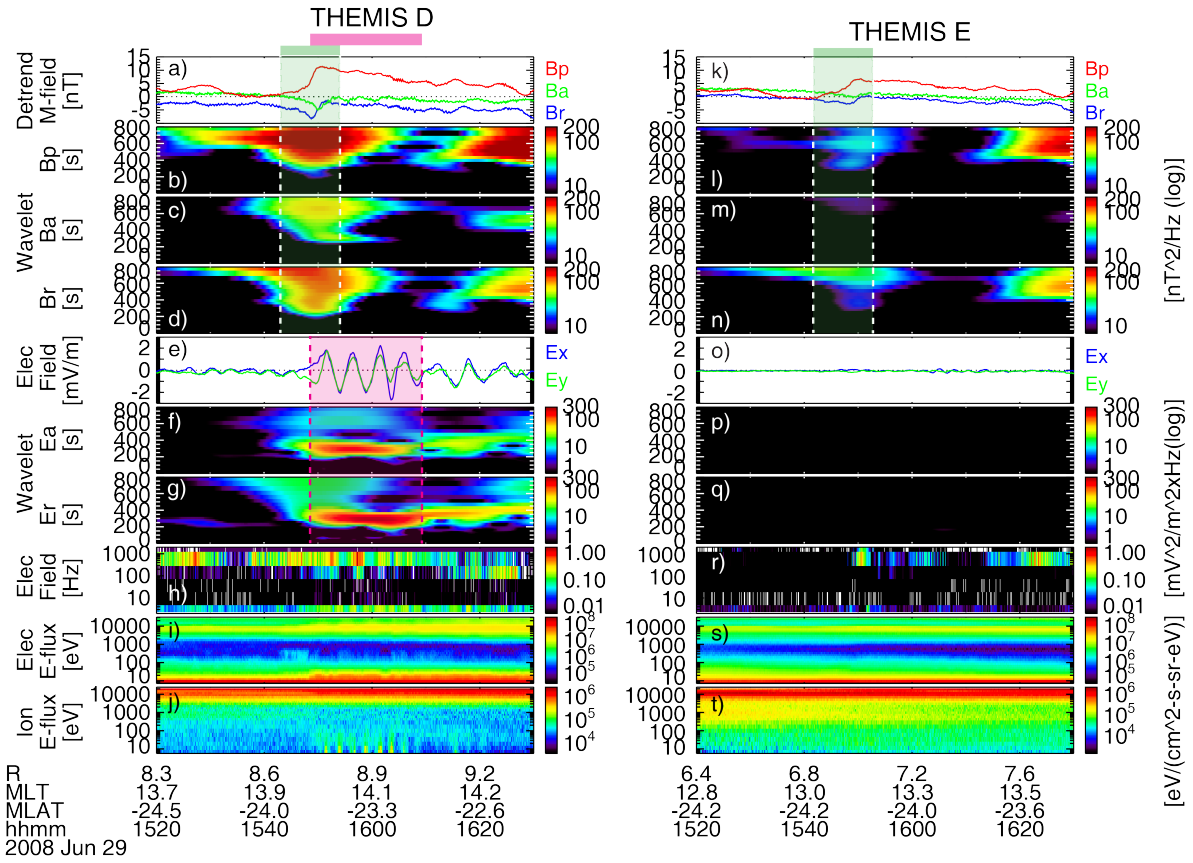

Figure 8.3 Magnetosphere observations by THEMIS D (Panels [a-j]) during 1520-1630 UT on June 29, 2008. Panels (a-j) show (a) magnetic field after subtracting the T01 model, wavelet analysis of the (b) field-aligned, (c) azimuthal and d) radial components of magnetic field, (e) electric field, wavelet analysis of (f) azimuthal and (g) radial components of electric field, (h) e-field spectra, (i) electron and (j) ion energy flux. Panels (k-t) show the same format of Panels (a-j), except for THEMIS E.

Following the compression signal, a strong ULF signal with a 250-350s period can be seen in electric field with a magnitude of ~2 mV/m in both azimuthal and radial components during ~1549-1609 UT (Figure 8.2f-8.2g), while the signal in magnetic field was very weak. This behavior suggests a standing wave with a node around the location of THEMIS D (near the equatorial plane or near the magnetopause). In contrast to THEMIS D, THEMIS E did not

observe ULF waves following the compressional signal, either in magnetic or electric field. This indicates that the ULF waves observed by THEMIS D did not propagate at least to the location of THEMIS E.

In order to identify the mode of the waves observed by THEMIS D during 1549-1609 UT, a 250-350s band was used to filter the magnetic and electric fields. Figure 8.4a and 8.4b show the magnetic field after subtracting average background with a 10-min sliding window, and electric field. Figure 8.4c-8.4e show the filtered compressional, toroidal and poloidal modes of filtered waves. Figure 8.4f shows the phase difference of each modes. It is clear that during 1549-1609 UT, the toroidal mode of this wave had a ~90° phase difference. It indicates that this wave was a standing wave. All the evidences shown above indicate that this wave was an FLR. Thus, the FLR distributed around TH-D (~8.8 Re) and was likely generated by the resonance between the shear alfvenic wave and a compressional wave with the same period, while THEMIS E (~7.7 Re) was outside the FLR.

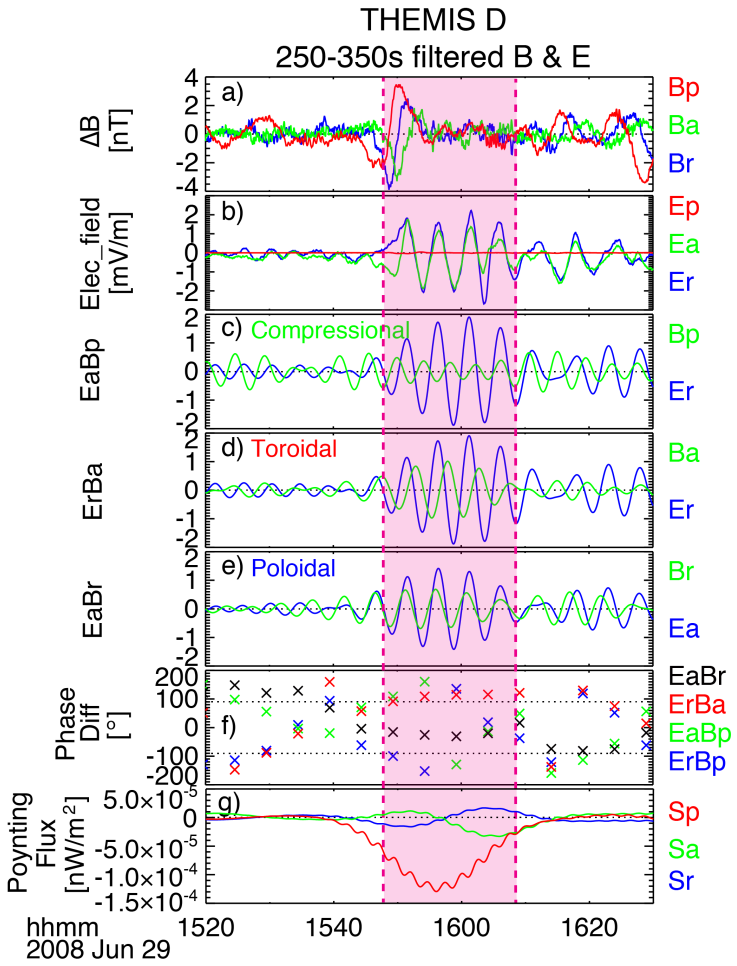

Figure 8.4 Analysis of magnetic and electric field data observed by THEMIS D during 1520-1630 UT on June 29, 2008. Panels show (a) magnetic field subtracting average background with 10-minute running window, (b) electric field, (c) compressional, (d) toroidal and (e) poloidal modes of the ULF wave with 250-350s band, (f) phase difference of the three modes and (g) Poynting flux.

There are two possible sources of the compressional Pc5 waves. One possibility is that the compressed leading edge of the foreshock transient caused the compression of the magnetosphere, and also generated a broadband Pc5 wave with >300s period during the magnetospheric compression as a response to the impulse. This is consistent with the idea of magnetospheric ULF response to the transient ion foreshock phenomena mentioned in the introduction. Transient ion foreshock phenomena can lead to variations in the upstream dynamic,

thermal, and/or magnetic pressure, which can excite Pc5 waves in the magnetosphere in much the same manner as large-scale dynamic pressure pulses in the pristine solar wind [*Hartinger et al.*, 2013]. The FLR occurs where the wave frequency matches the FLR frequency.

The second possibility is a directly-driven scenario. THEMIS C in the foreshock transient observed ULF waves that had the same period as the ULF waves in the magnetosphere. Compressional waves generated in the foreshock could penetrate into the magnetosphere and converted to FLRs where the compressional wave frequency matches the FLR frequency. This scenario has been predicted by a hybrid simulation by *Lin & Wang* [2005], and our study provides observational evidence of this process. We think that this scenario is more likely because the FLR was seen only near the L-shell of THEMIS-D but not near THEMIS-E despite that the compressional signal was seen at both satellites. Thus, the compressional Pc5 waves in the frequency contained in foreshock transient could also be a possible source of dayside magnetospheric Pc5 waves.

8.2.3 Auroral responses to Pc5 ULF waves

Figure 8.5 shows snapshots of red-line emission during 1528:38-1604:13 UT at South Pole. In order to see auroral structures clearly, we present differential intensity by subtracting the previous frame of image from the current image, which removes a slowly varying background. A localized discrete auroral brightening emerged in the FOV at ~1551 UT (Figure 8.5b) and propagated equatorward and duskward. This is consistent with the auroral response to the localized compression, which was generated by propagating foreshock transients, as shown in Chapter 6. The brightening occurred ~9 min after the compression signal detected by both THEMIS D and E.

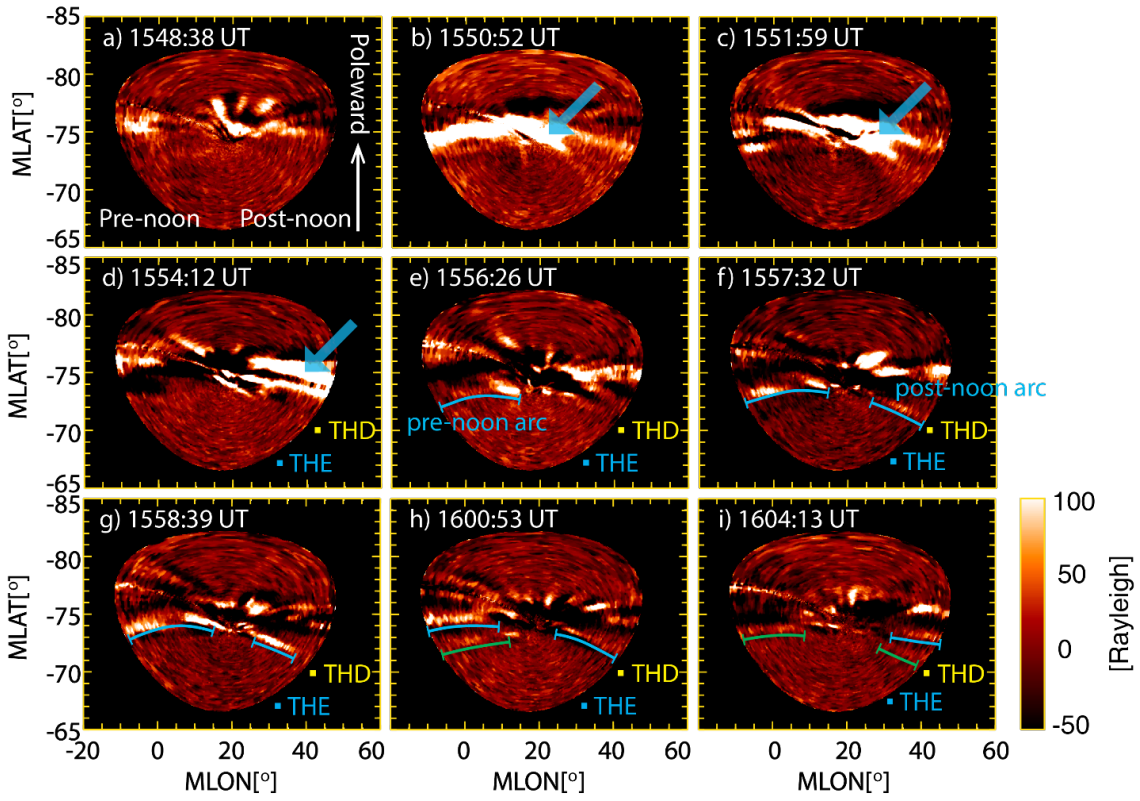

Figure 8.5 Panels (a-i) show the snapshots of red-line emission during 1548:38 through 1604:13 UT. The local noon during this period was at about the central longitude of the FOV. Here, the blue arrows point out the bright regions and solid blue/green lines present the east-west arcs.

Following the discrete auroral brightening, an east-west arc emerged at ~72° MLAT at ~1556 UT at pre-noon. This arc propagated poleward by ~3° and disappeared. At ~1557 UT, another arc showed up at similar latitudes in the postnoon sector, also propagating poleward by ~3°. These two arcs are considered as the first group of arcs and highlighted by the blue lines. It is noted that there was a gap of ~10° in longitudes near noon between the prenoon and the postnoon arcs. At ~1601 and ~1603 UT, a new group of arcs appeared in the prenoon and postnoon, respectively, at similar latitude to the first group. As a whole the arcs appeared and propagated poleward periodically.

Figure 8.6a-8.6b show the keograms of the red- and green-line emission. The keograms were made by the slice at ~15° longitude west of the FOV center, which covers the pre-noon aurora. The first auroral brightening showed up both in red- and green-line at ~1550 UT. This is the auroral signature that is related to the compressional signal, as we discussed in the beginning of this subsection. It was followed by four poleward moving arcs, mainly shown at the red-line wavelength. Figure 8.6c showed the average red-line intensity between 73.5° and 74° MLAT. Its wavelet analysis (Figure 8.6d) presents that these arcs had a period of ~300-450s, which was similar to the FLR period measured by THEMIS D.

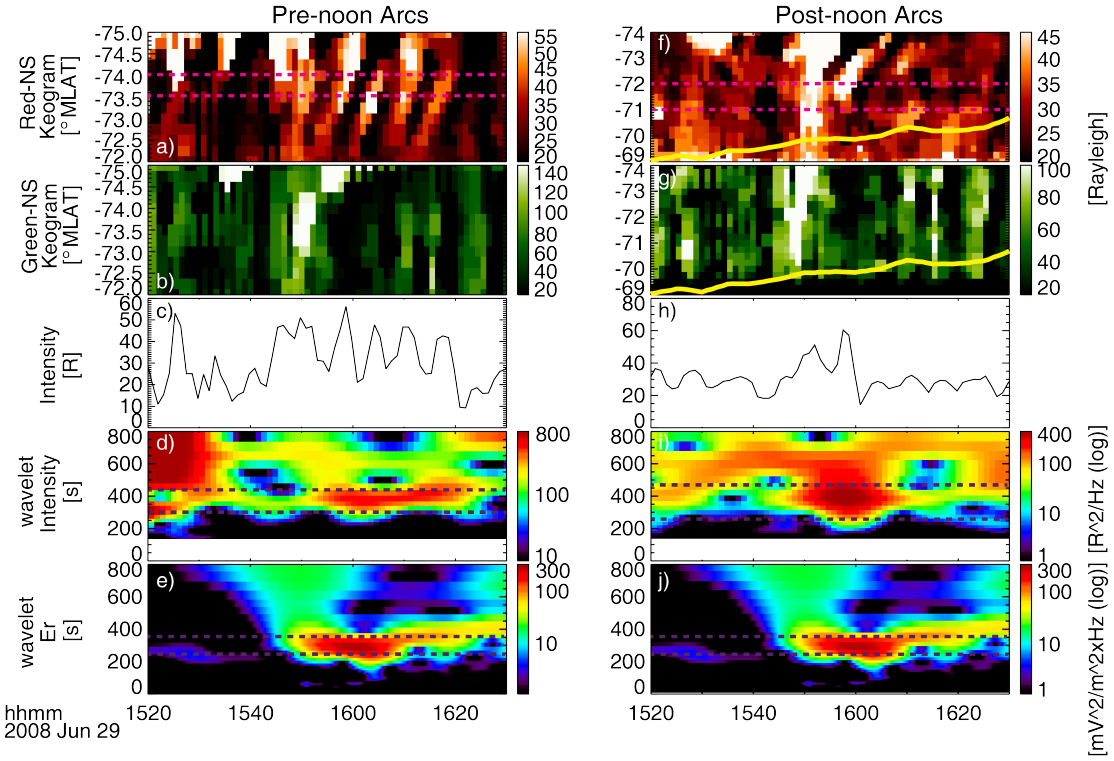

Figure 8.6 Panels (a-e) show keograms of (a) red-line and (b) green-line emission using the slice at ~15° longitude west of the FOV center of ASI at South Pole, (c) average intensity between 73.5°-74°S MLAT, (d) wavelet analysis of average intensity and (e) wavelet analysis of radial component of electric field by THEMIS D. Panels (f-j) show the same format of Panels (a-e), except for using the slice at ~15° longitude east of the FOV center of ASI at South Pole to make the keogram. Here, yellow lines show the ionospheric footprints of THEMIS D.

The post-noon arcs are shown by the keograms, which were made by the slice at ~15° longitude east of the FOV center (Figures 8.6f-8.6g). They had similar features to the pre-noon arcs. Figure 8.6i shows that the post-noon arcs also had a ~300-450s periodicity, which is consistent with the FLR period measured by THEMIS D. It is also noted that the ionospheric footprint of THEMIS D was located around the post-noon arcs, while the ionospheric footprint of THEMIS E, which did not observe any substantial Pc5 waves, was ~4° lower in latitudes. It indicates that these periodic poleward moving east-west arcs were the ionospheric signature of the foreshock-driven FLR.

We also compared the auroral signature with ground-based magnetometer observation. Figure 8.7 a-8.7j show the magnetic field and the wavelet analysis of the corresponding H component, observed by those stations. The dashed vertical line shows the initial time that THEMIS D observed the FLR. IQA and B23 were at the gap between the pre- and post- noon arcs (Figure 8.7). The stations did not detect clear FLR during the occurrence of the poleward moving east-west arcs. On the other hand, ATU and STF were near the post-noon arcs and they detected the clear FLR frequency associated with auroral response. Specifically, STF was at the center of post-noon arcs while ATU was at the poleward edge of those arcs. Correspondingly, the magnetometer at STF observed stronger FLR signal than the magnetometer at ATU. The consistency between the poleward moving east-west arcs and the ground-based observation shown above confirms that the arcs were the ionospheric signature of the FLR. Additionally, the magnetometer at B10 also observed the FLR frequency. It indicates that the post-noon arc and the FLR probably extended duskward to the location of B10.

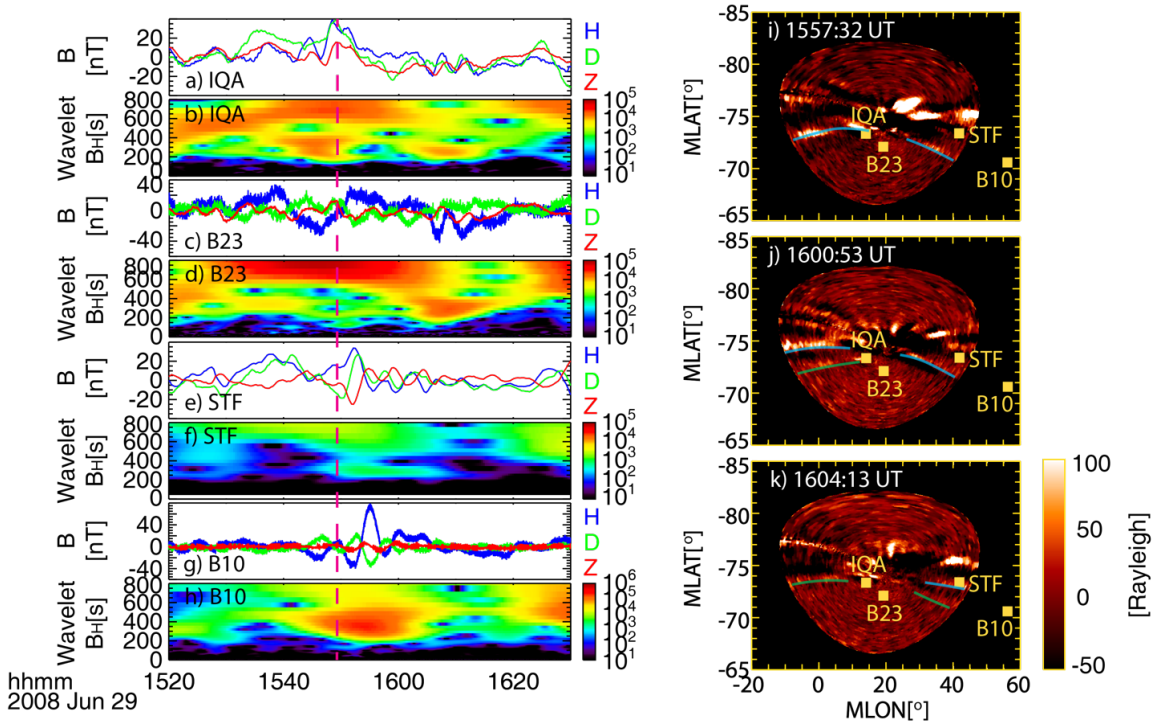

Figure 8.7 Panels (a), (c), (e) and (g) show the magnetic field observed by ground-based magnetometers at IQA, B23, ATU, STF and B10 stations, respectively. Panels (b), (d), (f) and (h) show the wavelet analysis of the H component of the magnetic field in Panels (a), (c), (e) and (g), respectively. Panels (i-k) show the snapshots at 1557:32, 1600:53 and 1604:13 UT, with the positions of B10 and B23, and the conjugate positions of IQA and STF around South Pole.

The poleward propagation of those east-west arcs was interpreted as the 180° phase difference of the wave electric field across the resonance latitude [*Knox & Allan*, 1981; *Wright & Allan*, 1996]. This leads to a zero electric field region moving across the resonance region, giving a repetitive poleward phase propagation.

8.2.4 Comparison with global MHD simulation

While the existence of an FLR can be found by in situ observation, it is difficult to measure its 2D structure on the equatorial plane by a limited number of satellites. However, 2D

structure can be measured by the optical observation, which has higher spatial resolution than by other ground-based instruments, as shown in Subsection 8.2.4.

The first and second arcs were mapped to the equatorial plane by the T01 model [*Tsyganenko*, 2002], as shown in Figures 8.8a-8.8e by the red and orange solid lines, respectively. Within the MLT coverage of the ASI images around the latitudes of the arcs, the arcs were distributed symmetrically in the prenoon and postnoon sectors, with a gap around the noon. This is consistent with the global MHD simulation result [Figure 8.8h; adopted from *Claudepierre et al*., [2010], which shows that the toroidal component of the odd mode FLR has a two-peak structure with a node around the noon.

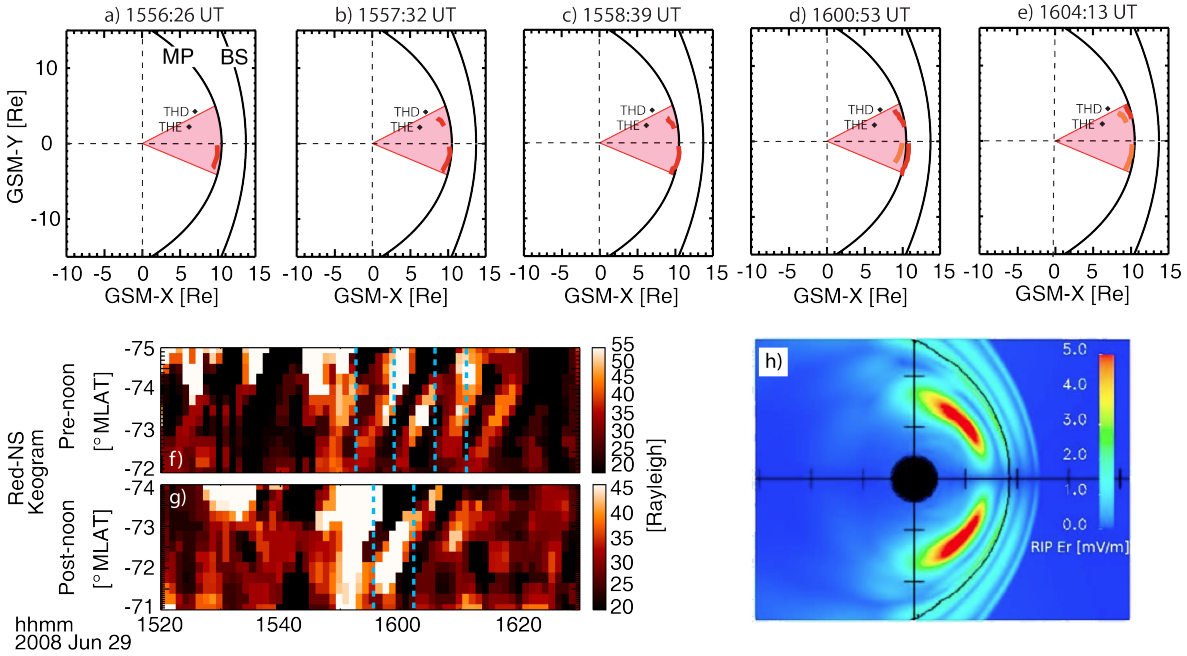

Figure 8.8 Thick solid red and orange lines in Panels (a-e) show the mapped structure of the arcs which are indicated by blue solid lines in Figures 8.5e-8.5i and green solid lines in Figures 8.5h and 8.5i, respectively, on the equatorial plane. Here, the red shades show the FOV coverage at the MLAT of the arc indicated by blue solid lines in Figures 8.6e-8.6i. Panels (f) and (g) are copied from Figures 8.6a and 8.6f, and the blue dashed lines show the initiation of each arc. Panel (h) is adopted from Figure 3a of *Claudepierre et al*., [2010].

Besides, Figures 8.8a-8.8e show that the pre-noon arcs showed up earlier than the post-noon arcs. This can be clearly shown in the keograms. Figures 8.8f-8.8g compare the prenoon and postnoon arcs shown in Figure 8.6. The blue dashed lines mark the initial time of each arc, showing that the postnoon arcs always occurred between the occurrences of two prenoon arcs. It indicates that the corresponding FLR signal in the prenoon and postnoon were in anti-phase. This is also consistent with behaviors of an odd mode FLR.

8.3 The second Pc5 ULF wave: 1700-1815 UT on June 29, 2008

8.3.1 Upstream observation

During 1650 through 1820 UT on June 29, 2008, there were two THEMIS satellites (THEMIS B and C) in the solar wind. As shown in Figure 8.1b, THEMIS B was ~30.8 Re away from the Earth and at ~14.4 MLT in the dayside. THEMIS C was ~17.2 Re away from the Earth and at ~15.8 MLT in the dayside.

The solar wind condition in this time interval was similar to that in the first event. An IMF discontinuity was observed at ~1704 UT by THEMIS B (Figure 8.9a). The reflected superthermal ions were seen right after this IMF discontinuity as shown in Figure 8.9e and 8.9l. THEMIS C observed that the IMF cone angle changed from ~30° to ~70°. It indicates that the IMF discontinuity that was observed by THEMIS B at ~1704 UT probably arrived at THEMIS C during 1703-1712 UT. The strong fluctuation was caused by the superthermal ions during 1703-1712 UT, which was associated with a significant reduction in Vx, and the dynamic pressure increases at the boundaries. The features of this foreshock transient were consistent with an HFA. This foreshock transient was associated with a 200-450s ULF wave, mainly shown in the dynamic pressure variation, during 1704-1718 UT.

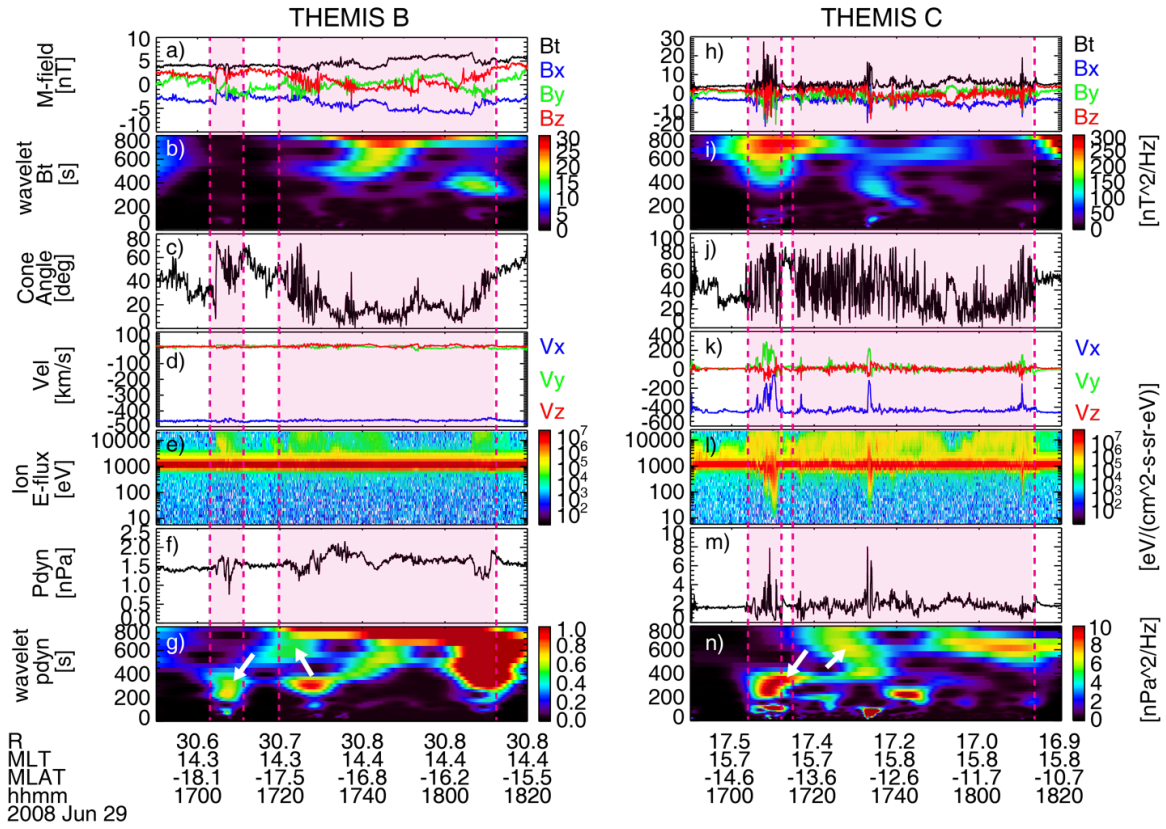

Figure 8.9 Same format as Figure 8.2, except during 1650-1820 UT on June 29, 2008.

Since ~1720 UT, both THEMIS B and C observed that the IMF started to rotate and the cone angle decreased to ~5°. The superthermal ions showed up within this time period. It was probably a travelling foreshock, which propagated with the low-cone-angle IMF structure [*Kajdič et al.*, 2017]. There was a 500-700s ULF within the travelling foreshock, adjacent to its leading edge at 1720 UT. There was another ULF wave with the same period, which was adjacent to its trailing edge during ~1750-1815 UT.

Besides, those ULF waves were not observed in OMNI, indicating that they were generated in the foreshock transients, instead of the pristine solar wind.

8.3.2 Pc5 ULF waves in the dayside magnetosphere

In the dayside magnetosphere, THEMIS D and E also observed perturbations during the foreshock disturbances. Figure 8.1b shows that in the second case, THEMIS D was ~10.0 Re away from the Earth and at ~14.7 MLT in the magnetosphere. THEMIS E was ~9.0 Re away from the Earth and at ~14.2 MLT in the magnetosphere.

Figure 8.10a shows magnetic field oscillation during ~1700-1720 UT. The wavelet analysis shows that its period was ~350-500s and its field-aligned component was dominant. This indicates that it was a compressional wave. The ULF waves with the same frequency was also found in THEMIS E during about the same time period. This compressional wave was highlighted by green shades in Figure 8.10a-8.10d and Figure 8.10k-8.10n. It occurred right after the first foreshock transient and the compressional wave with the similar period, observed by THEMIS B and C during ~1700-1718 UT. This indicates that the magnetospheric Pc5 compressional wave was probably driven by the foreshock.

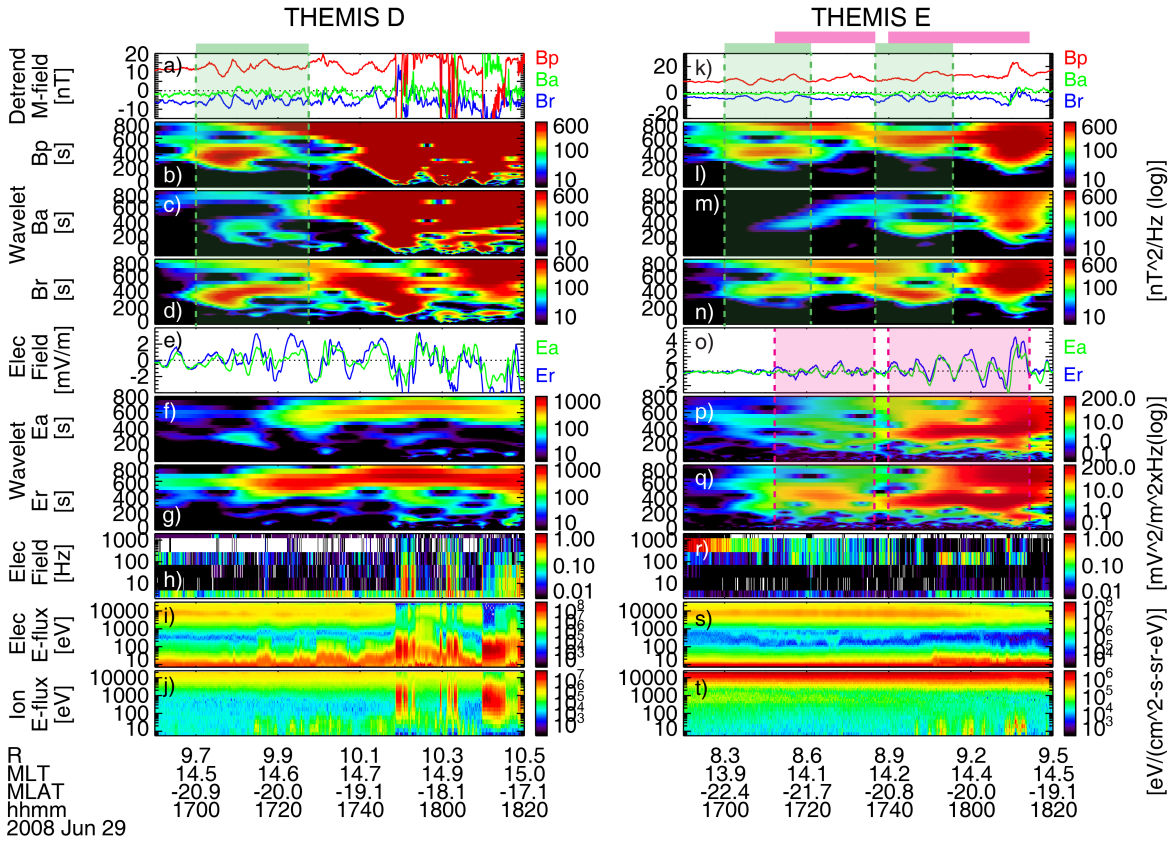

Figure 8.10 Same format as Figure 8.3, except during 1650-1820 UT on June 29, 2008.

Furthermore, the Pc5 wave with 350-500s period continuously existed especially in Br, while not substantially in Bp, during ~1718-1728 UT. This indicates that during 1700-1728 UT, the compressional waves may couple with other modes of ULF waves. Thus, more analysis of this wave is shown in Figure 8.11c-8.11g by filtering the data with a 350-500s passband. It is clear that during 1700-1728 UT, the toroidal and poloidal components of the magnetic field intensified. Furthermore, the phase difference of the toroidal component was ~90°. This indicates that the compressional wave was probably coupled with an FLR with the same period. THEMIS E also observed a 350-500s ULF wave in electric field variation, following the compressional wave, with relatively lower wavelet spectrum power (highlighted by the first pink shae in Figure 8.10o-8.10q). Figure 8.10m shows that the phase difference of the toroidal wave was firstly

~180° and then changed to 90°. It is possible that THEMIS E was at the earthward edge of the 350-500s FLR, and it detected a strong compressional but weak FLR signal.

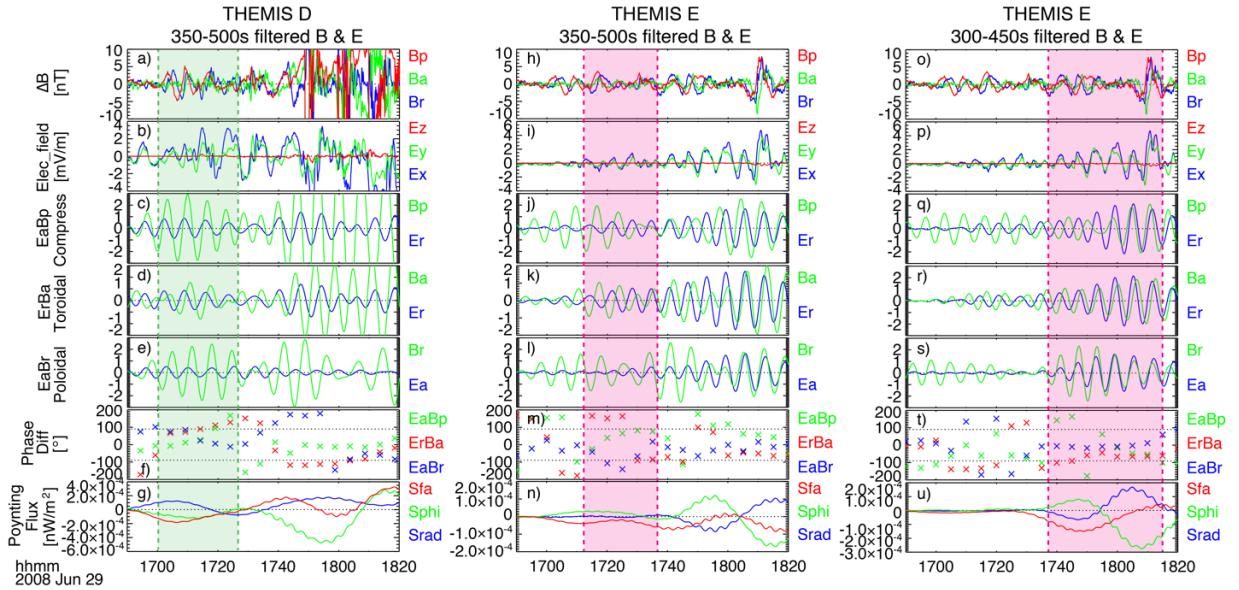

Figure 8.11 Panels (a-g) show the same format as Figure 8.4 except that the ULF waves were filtered by a 350-500s band; Panels (h-n) show the same format as Figure 8.4, except that the ULF waves were observed by THEMIS E and filtered by a 350-500s band; Panels (o-u) show the same format as Figure 8.4, except that the ULF waves were observed by THEMIS E and filtered by a 300-450s band.

Starting from 1720 UT, THEMIS D and E observed a ULF wave with a period of ~500-700s. Both satellites observed the intensification of the wavelet spectrum power of Bp, indicating it was a compressional wave. This magnetospheric compressional wave occurred spontaneously with the traveling foreshock, and it was associated with the same period of the waves in the foreshock, which were observed by THEMIS B and C (Figure 8.9g and 8.9n). It indicates that the magnetospheric compressional wave was driven by the foreshock. From ~1737 UT, a ULF wave with ~300-450s period was observed by THEMIS E, both in magnetic and electric field. It was probably the second harmonic of the compressional wave with 500-700s period. During

1756-1825 UT, the wavelet spectrum power of this ULF wave continuously existed in the electric field.

The ULF wave observed by THEMIS E was filtered with a 300-450s band and the related analysis is shown in Figure 8.11o-8.11u. Its toroidal component had the phase difference of ~90°. This indicates it was a toroidal standing wave, which was mostly an FLR.

It is noted that THEMIS E was ~1 Re closer to the Earth than THEMIS D and the period of the FLR observed by THEMIS E was shorter than that observed by THEMIS D. This was consistent with that the frequency of FLR depends on the magnetic field length.

8.3.3 Auroral response to the Pc5 ULF waves

Figure 8.12 shows the snapshots of red-line emission during 1723:12-1737:40 UT at South Pole. The center of the FOV during this time period was ~14 MLT and the entire FOV was in the postnoon sector. Similar to the first case, there were periodic poleward moving east-west arcs. While differently, there were two groups of arcs at different latitudes. One arc in the first group is marked by the blue lines, shown in Figure 8.12b and 8.12c. The center of it is at ~74° S in MLAT, near the ionospheric footprint of THEMIS D. One arc in the second group is marked by the green lines, shown in Figure 8.12d-8.12f. The center of it is at ~72° S in MLAT, near the ionospheric footprint of THEMIS E.

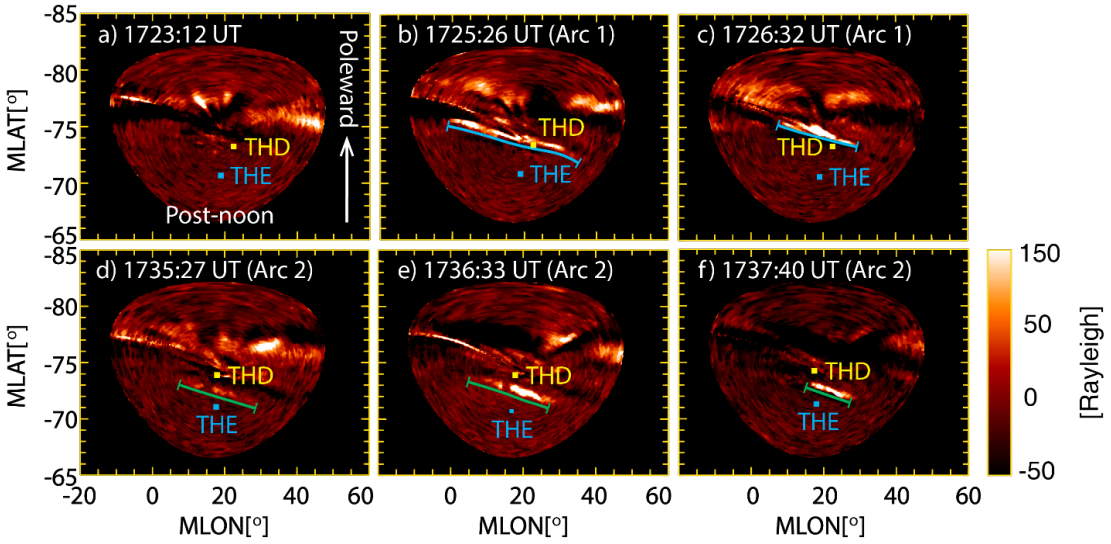

Figure 8.12 Panels (a-f) show the snapshots of red-line emission during 1723:12 through 1737:40 UT. The local noon during this period was at ~-10° MLON. Here, the solid blue/green lines highlight the east-west arcs.

Figure 8.13a shows the north-south keogram of red-line emission. The yellow and blue lines are the ionospheric footprints of THEMIS D and THEMIS E, respectively. The keogram clearly shows two groups of poleward moving arcs at ~74° S and ~72° S during ~1717-1730 UT and 1737-1817 UT, respectively. The integrated intensity between 73.5-74.5° S is shown in Figure 8.13b and the wavelet analysis of it is shown in Figure 8.12c. The period of this group of arcs was around ~500s, which was similar as the period of the FLR observed by THEMIS D and THEMIS E. The integrated intensity between 71.5-72.5° S is shown in Figure 8.13e and the wavelet analysis of it is shown in Figure 8.13f. The period of this group of arcs was around ~400-450s, which was similar to the period of the FLR observed by THEMIS E during the same time period. The consistency between the period of magnetospheric and auroral signals indicates that these two groups of periodic poleward moving arcs were the ionospheric signatures of the FLRs shown by THEMIS D and E.

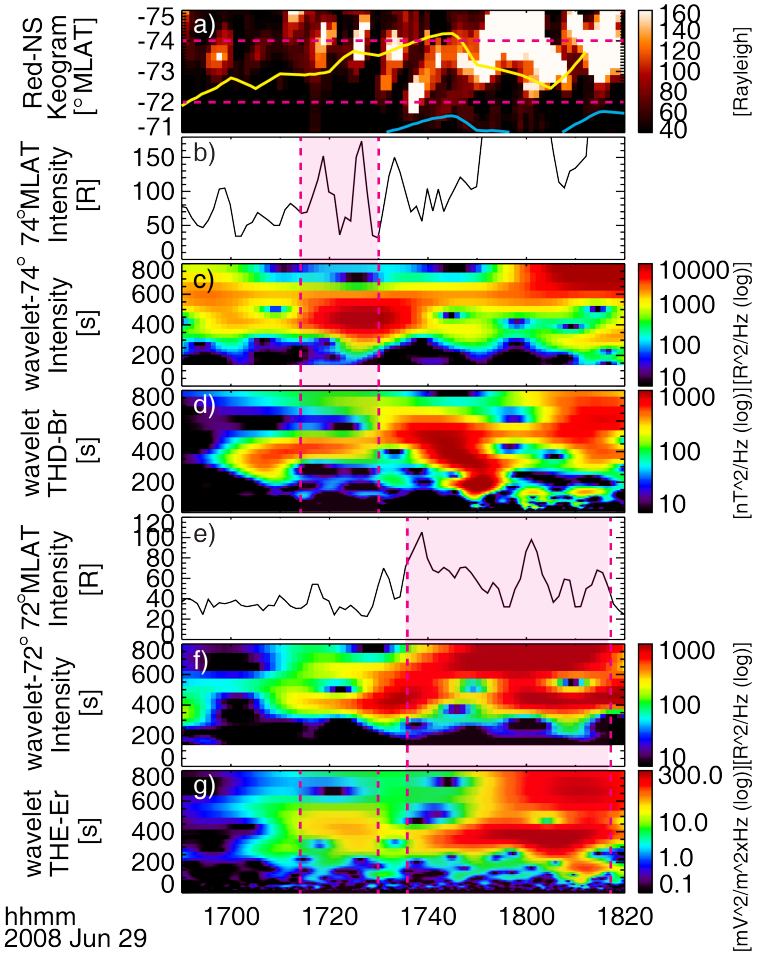

Figure 8.13 Panels (a-g) show (a) north-south keogram of red-line emission using the FOV center of ASI at South Pole, (b) average intensity between −73.5° and −74.5° MLAT, (c) wavelet analysis of average intensity shown in panel (b), (d) wavelet analysis of radial component of magnetic field observed by THEMIS D, (e) average intensity between −71.5° and −72.5° MLAT, (f) wavelet analysis of average intensity shown in panel (e), (g) wavelet analysis of radial component of electric field observed by THEMIS E. The yellow and blue lines in panel (a) show the ionospheric footprints of THEMIS D and E, respectively.

The observations by ground-based magnetometers at IQA, B23, STF and B10 are shown in Figure 8.14. Two dashed vertical lines show the initial time of the 350-500s FLR and the 300-450s FLR observed by THEMIS D and E. Both FLR frequencies were detected at all the stations. Among those, IQA and B23, which were right at the arcs, observed much stronger signals than STF, which was at the edge of the arcs. The ground magnetometer response confirms that those

poleward-moving east-west arcs were the ionospheric signature of the FLRs. Additionally, B10 observed strong signal of the 300-450s wave, which was comparable to the signal observed at IQA and B23. It is probably because the next azimuthal crest of the FLR wave was at around B10. This guess is consistent with that the distance between IQA/B23 and B10 (i.e. the distance between two consecutive crests, which is about the wavelength) was about double of the arc length (i.e. about a half wavelength) in the second group.

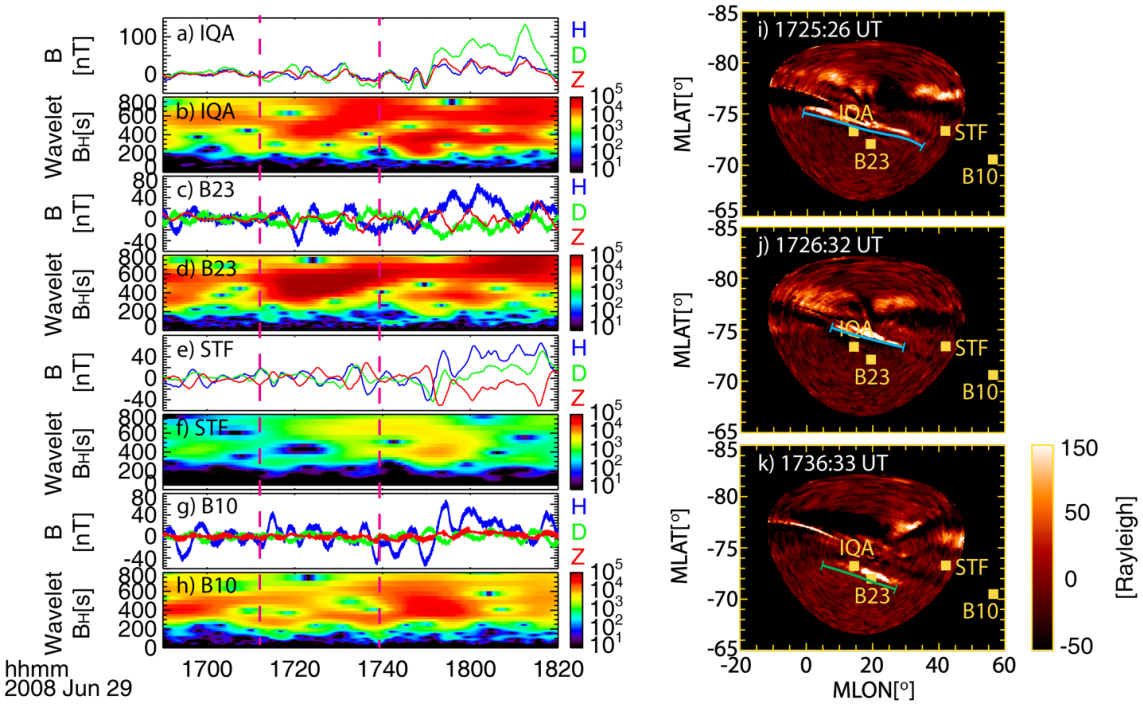

Figure 8.14 Panels (a-h) have the same format as Figures 8.7a-8.7h, except for the time range from 1650 UT to 1820 UT on June 29, 2008. Panels (i-k) show the snapshots at 1725:26, 1726:32 and 1736:33 UT, with the positions of B10 and B23, and the conjugate positions of IQA, and STF around South Pole.

8.3.4 2D structure of the FLR

Similar to the first case, with the auroral response to FLRs as shown in Subsection 8.3.3, the structure can be measured by the 2D snapshots.

The first and second group of arcs are mapped to the equatorial plane by T01 model, shown in Figure 8.15 by red and blue solid lines, respectively. Since the MLT coverage of the ASI images (red and blue shades) around the latitudes of the arcs were entirely in the postnoon sector, this case can present the entire arc structure. The first group of arcs had a maximum length of ~35°, which corresponded to half of a wavelength in the azimuthal direction. It indicates that its wavelength was about 2140 km in the ionosphere and 8.0 Re on the equatorial plane, and its toroidal wavenumber was ~5 if this is a periodic structure around the Earth. The second group of arcs had the maximum length of ~25°. It indicates that its wavelength was about ~1720 km wavelength in the ionosphere and 5.2 Re on the equatorial plane, and its toroidal wavenumber was ~7. Furthermore, the second group of arcs contain fine structures as shown in Figure 8.15e and 8.15f. Each fine structure was about ~2.5°, indicating a higher toroidal wavenumber of ~140. The corresponding wavelength was about ~86 km in the ionosphere and ~0.26 Re on the equatorial plane.

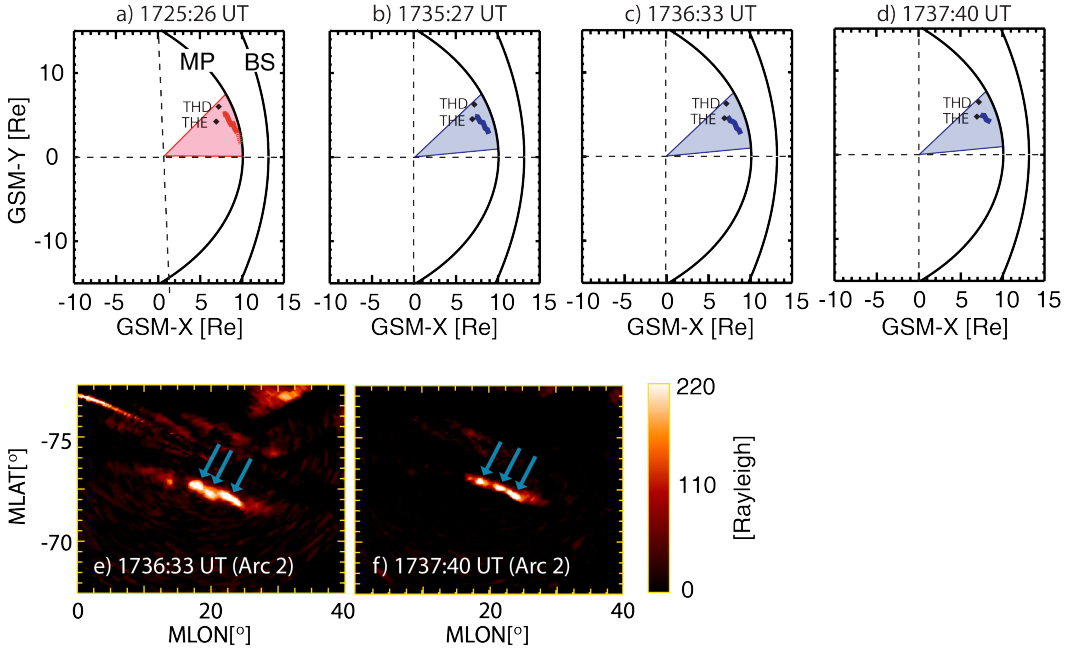

Figure 8.15 Thick solid red and blue lines in Panels (a-d) show the mapped structure of the arcs which are indicated by green and blue solid lines in Figure 8.11, respectively, on the equatorial plane. Here, the thick dashed red line show the estimated position of mapped arc near the open-closed filed line boundary, and the red and blue shades show the FOV coverage at the MLAT of the arc indicated by blue and green solid lines, respectively, in Figures 8.11. Panels (e) and (f) show the zoom-in snapshot of red-line emission at 1736:33 and 1737:40 UT, respectively.

8.4 Discussion

As discussed in the last two paragraphs of Subsection 8.2.2, we proposed two possible sources of the magnetospheric compressional waves for the first case. One was that the compression pulse could cause the magnetopause oscillation in the same manner as interplanetary shocks. Another one was that the compressional waves in the foreshock could directly penetrate into the magnetosphere and converted to FLRs.

In case 2, two compressional waves with different periods were observed ~1700 and 1720 UT in the dayside magnetosphere. They occurred right after the compressed boundary of two foreshock transients shown in Subsection 8.3.1. Thus, the magnetospheric compressional

waves could occur because of those dynamic pressure increases. However, the compressional waves in the foreshock were associated with the same or double period of the corresponding magnetospheric compression waves, which is in favor of the second scenario, because it is difficult to abruptly change the frequency of magnetospheric response to dynamic pressure pulses.

8.5 Conclusion

In this paper, we investigated the 2D structure of Pc5 ULF waves in the dayside magnetosphere, using the conjunction between the THEMIS satellites and the ASI at South Pole on June 29, 2008. The schematic illustration in Figure 8.16 shows the dayside Pc5 ULF waves and their auroral responses. Our results are summarized as follows:

1. The Pc5 ULF waves, including compressional waves and FLRs, in the dayside magnetosphere were driven by foreshock disturbances.
2. Periodic poleward moving east-west arcs were observed as the ionospheric signature of dayside FLRs:
    a. The arcs were distributed symmetrically in the prenoon and postnoon sectors in anti-phase with a node around the noon. This is consistent well with the simulation result of an odd-mode FLR.
    b. The arcs mapped to the equator in the second case were about 8.0 and 5.2 RE size, corresponding to the FLRs with the period of 350-500s and 300-450s, respectively. This case also presented that the frequency of the FLR decreases with increasing L-shell.

c. The arcs in the second case show the entire structure in the FOV. This can be used to measure the toroidal wavenumber of the FLR. In this case, the FLRs with the period of 350-500s and 300-450s were associated with the wavenumber of 5 and 7, respectively.

d. The fine structure of arcs in the second case indicates that a higher toroidal wavenumber (~140 for the FLR with the period of 300-450s) mode wave was coupled with the primary FLR. It provides the opportunity to determine a large wavenumber of Pc5 waves with optical images.

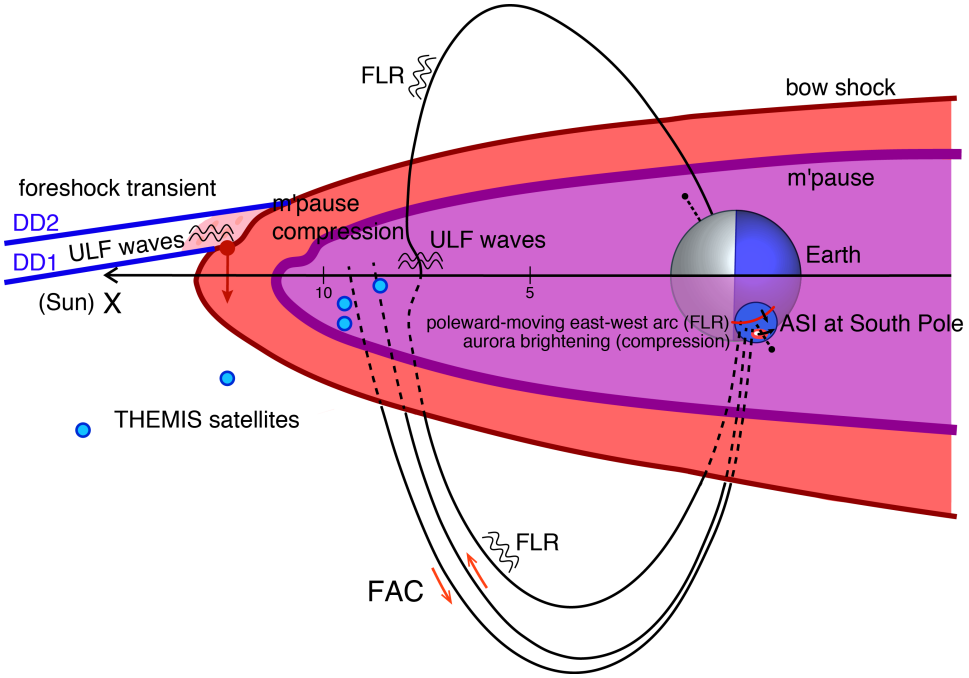

Figure 8.16 Schematic illustration of Pc5 ULF waves in the foreshock and dayside magnetosphere, and their auroral responds.

With the optical observation, this study was able to show how the dayside magnetospheric Pc5 ULF waves respond to foreshock disturbances in a 2D perspective and higher spatial resolution. A statistical perspective study are needed to address how common these findings are.

CHAPTER 9

Summary and open questions

9.1 Summary

The overarching objective of this dissertation is to identify the interaction between upstream transient disturbances and the coupled ionosphere-magnetosphere system, by a comprehensive study of their dayside auroral responses. Our study takes a unique and creative approach by taking advantage of high-resolution 2D imaging to advance community's understanding of magnetospheric and ionospheric responses to upstream disturbances, through tracing location, size and propagation of optical structures.

In optical measurements, four transient and localized structures, which are PMAFs, airglow patches, localized diffuse/discrete brightenings, periodic poleward-moving east-west arcs, are identified in this dissertation. According to the simultaneous in situ observation, those optical structures occur with different transient and localized upstream activities, including IMF southward turnings, foreshock transients and magnetosheath HSJs.

In **Chapter 4**, in order to identify upstream activities in triggering PMAFs, we surveyed all conjunctions between THEMIS B/C in the solar wind, at ~20-30 Re away from Earth, and the ASI at the AGO P1 station and identified 60 cases with PMAFs and upstream observations, during 2008, 2009 and 2011. The superposed epoch analysis shows that ~70% of events are preceded by IMF southward turnings by ~8 min. It indicates that IMF southward turnings play the most important role in triggering PMAFs. This is reasonable as PMAFs are believed to be the auroral signature of FTEs, which are localized reconnection at the dayside magnetopause.

Besides, the correlation between IMF measurements in the OMNI dataset and PMAFs occurrence is ~40%, which is much lower than the correlation measured with THEMIS measurements. It indicates the solar wind evolution between the L1 points and Earth or some small IMF structures did not pass the L1 point but finally arrived in Earth. Among the other ~30% PMAFs, although they occur during steady IMF, some other variances, such as IMF By reversals and foreshock disturbances, may contribute to the occurrence of those PMAFs. This study for the first time quantifies how commonly PMAFs are triggered by IMF orientation changes, which was elusive in the past studies due to limited availability of accurate solar wind information near the bow shock. Our finding indicates that FTEs are often triggered by solar wind changes rather than spontaneously occurring.

We further studied the evolution of PMAFs in the dayside polar cap in **Chapter 5**. We utilized the coordinated observations of the DMSP satellites and ASI at the AGO P1 station, and identified 50 airglow polar cap patches. Forty five out of them are evolved from PMAFs, and are collocated with fast anti-sunward flow channels. The flow channel speeds average 1100 m/s over the observed airglow patches, which is much faster than the background two-cell convection speeds of ~500 km/s. The average width of those flow channels is ~300 km, which is also comparable to the average width (~400 km) of those airglow patches. Those indicate that the dayside plasma density, which are ionized by sunlight, can be brought to the polar cap and forming airglow patches, by the fast channels, which are originally the reconnection bursty flows associated with PMAFs.

Besides transient IMF variations, we also examine the magnetospheric and ionospheric responses to localized dynamic pressure variations, which can be generated by foreshock transients and magnetosheath HSJs. Upstream dynamic variances have two magnetospheric

responses: dayside magnetospheric compressions and ULF waves. On the other hand, aurora behave differently with those two magnetospheric responses, which potentially help to identify the physical process in the magnetosphere in a 2D perspective.

In **Chapter 6**, we conducted a detailed analysis of a foreshock transient on 25 June 2008, based on the observation by the THEMIS and GOES satellites, ASI at South Pole station, and magnetometers in Greenland and Canada. A foreshock transient was observed by THEMIS B and C to propagate toward the Earth. The transient is probably a foreshock cavity or a proto-HFA, which was sandwiched within two tangential discontinuities and swept through the magnetosheath from the dawnside to duskside. Magnetospheric compressions were detected by THEMIS A, D, E, GOES 10 and 12 in the subsequent ~10 min, also propagating duskward, which is consistent with the motion of the foreshock transient. Diffuse aurora brightened soon after the foreshock transient observation. The mapped pattern of diffuse auroral brightening on the equatorial plane shows a width of ~4.3 Re in the GSM-Y direction, which is slightly larger but similar to the typical size of foreshock transients. The mapped pattern propagated duskward with an average speed of ~100 km/s, also similar to the motion of the upstream foreshock transient. The diffuse aurora also brightened in coincidence with the occurrence of an R2-sense FAC. Soon after diffuse aurora brightened, discrete aurora brightened. The discrete auroral brightening also shows a localized signature and propagated duskward. The equivalent current pattern shows that the discrete auroral brightening is associated with the upward FAC portion of the R1-sense FAC.

In addition to foreshock transients, Chapter 7 shows magnetospheric and auroral responses to magnetosheath HSJs based on the coordinated observation between the THEMIS satellites and the ASI at South Pole station during 2008 through 2010. Similar to foreshock

transients, all of eight HSJ events exhibited clear association between magnetosheath HSJs and discrete/diffuse auroral brightenings. Using those auroral responses, we were able to determine location, size, and motion of HSJ-magnetosphere interaction that are difficult to measure by other means. The patterns of the diffuse auroral brightenings mapped to the equatorial plane show an azimuthal width of ~3.7 Re, which characterizes the geoeffective scale of HSJs. In addition, the azimuthal velocities of those mapped patterns show a good consistency with the GSM-Y components of the magnetosheath background flows. This indicates that the compressed region of the magnetopause propagates azimuthally following the background magnetosheath flows. Although a slight azimuthal motion of auroral patterns is observed with magnetosheath HSJs, the azimuthal motion is much slower compare to that associated with foreshock transients.

At last, in **Chapter 8**, we investigated the 2D structure of magnetospheric Pc5 ULF waves driven by foreshock transients using two conjunction events of the THEMIS satellites and the ASI at South Pole on June 29, 2008. Both of the foreshock transients are associated with significant Pc5 ULF waves, which are found to be FLRs. The optical imagers show that they were associated periodic poleward moving east-west arcs with almost the same frequencies as the FLRs. By mapping those arcs to the equatorial plane by the T01 model, we determined the 2D structures of the foreshock-driven FLRs. The mapped patterns of the arcs were distributed symmetrically in prenoon and postnoon sectors with out-of-phase oscillations. This provides observational evidence of an odd-mode FLR predicted by global MHD simulations. The mapped patterns at higher L-shells were associated with lower frequencies, which is consistent with the physical properties of FLRs. Also, fine structures with a higher toroidal wavenumber mode waves were found and they were localized within the FLR arcs, which indicate coupling between the low and high wavenumber Pc5 waves.

In a summary, by using the coordinated observation between satellites and ground-based ASIs, this dissertation conducted a comprehensive study on dayside aurora, which allows to remotely sense the disturbances in the ionosphere, magnetosphere, magnetosheath, foreshock and solar wind, in a 2D perspective and high spatial resolution. Chapter 4 and 5 study a) the PMAFs as triggered by upstream transients, including IMF southward turnings and foreshock disturbances by satellite-imaging coordinated observation; and b) their evolution in the polar cap as airglow patches associated with the meso-scale flow channels. Chapter 6, 7 and 8 present a likely scenario revealed from the satellite-imaging coordinated observations as follows: Foreshock transients and magnetosheath HSJs drive compressions of the magnetopause at a few RE, much more localized than global compression by shocks. The compressions launch fast-mode waves and FLRs, which create localized electron precipitation and auroral brightenings. The auroral responses found in this study can highlight structure and evolution of the magnetosphere-ionosphere responses, and signify the geoeffectiveness of localized and transient upstream energy input.

9.2 Open questions and future work

1) Where are airglow patches generated? Cusp, or anywhere else?

In our study, the statistical study on the polar cap patches originated in PMAFs showed a By dependence, while the correlation is not very high. Some PMAFs have significant azimuthal propagation of about 6 MLT from noon along the auroral oval and then detached from the auroral oval, evolving to an airglow patches, while the IMF By was not very large. Although many studies suggested that azimuthal propagation or expansion were due to two-cell convection, which can be highly asymmetric under strong By conditions [*Reiff & Burch*, 1985; *Rich &*

Hairston, 1994], our results suggest that convection is even more skewed than known statistical two-cell convection, possibly due to localized fast flow channels. Some studies also reported that PMAFs can expand in the opposite direction of what is expected for the polarity of IMF By [*Milan et al*., 2000]. They suggested that the corresponding expansion of PMAFs were due to the expansion of the reconnection X-line. Besides, *Dang et al*. [under preparation, 2018] also presented two TOIs generated at different MLTs in both modeling results and the observation by DMSP. Thus, where PMAFs/reconnections occur, how patches detach from the auroral oval, and how they propagate under multi-scale convection, are important open questions.

In order to address those questions, a dense spatial coverage of convection pattern by radar measurements is needed to examine flow structures associated with the optical sequence. The relation between the convection pattern and airglow patches will help to understand patch formation. Large-scale auroral oval configuration should also be examined to cover the large PMAF MLT evolution.

2) What's the properties of geoeffective HSJs?

Although the properties of magnetosheath HSJs themselves are measured in both case and statistical studies, it is still difficult to know how often HSJs impact the magnetosphere. Previous papers considered that the geoeffective HSJs should be sufficiently large in width, and that a minimum diameter of ~2 Re is considered to be reasonable for the geoeffective HSJs [*Hietala et al*., 2012; *Plaschke et al*., 2016a; *Shue et al*., 2009]. But the 2 Re size was suggested only based several case studies or calculations based on upstream observations. Such measurements of geoeffective HSJs' diameters require at least 2 satellites with proper spatial separation, with large uncertainties, and at least another satellites in the dayside magnetosphere

at the same time. Such conjunctions are too difficult to find. Thus, there was still no statistical study describing the properties of geoeffective magnetosheath HSJs.

To address this question, our HSJ study with optical images provides a method to estimate the diameter of HSJs' geoeffectiveness. Although this number may be somewhat larger than the diameter of HSJs due to the radial propagation of compressional signals, they should still be comparable to each other. However, as shown in Chapter 7, due to the THEMIS orbits during 2008 through 2010, there were not many conjunctions between THEMIS and ASI at South Pole to study magnetosheath HSJs with auroral responses. This limits us to do a statistical study with eight events.

Fortunately, now we have newly-released data by ASI at South Pole during recent years, and also, THEMIS A, D and E had chances to cross solar wind, foreshock and magnetosheath in the summers during 2015 through 2017. Thus, it is expected to have more good conjunctions to study magnetosheath HSJs with optical images and a statistical study is promising.

3) Does HSJs also trigger dayside FLRs as foreshock transients?

Chapter 7 shows that magnetosheath HSJs can compress the dayside magnetosphere locally, and some HSJs are associated with Pc5 waves. Also, in Chapter 8, a 2D structure of foreshock-driven FLRs is presented. Those propose a straightforward question: whether HSJs can also drive magnetospheric FLRs? This question can be addressed by revisiting our current data set used in Chapter7.

4) What is the energy input from the magnetosphere to the ionosphere by compression and ULF waves?

In Chapter 6, 7 and 8, magnetospheric compressions and ULF waves were found to be associated with auroral brightening, which indicates the electron precipitation into the ionosphere. Those electron precipitation should be associated with the energy transport between the magnetosphere and ionosphere, causing aurora heating and affecting the conductance of the ionosphere. What the energy input in the ionosphere, which is caused by foreshock- or HSJ-driven compression and ULF waves, is an open question. Although in situ observation cannot provide the information of election precipitation, ground-based imagers can help with the measurements.

Auroral emission lines (e.g., 427.8, 557.7, 630.0 and 844.6 nm) are predicated by multiple electron transport models to be directly correlated with the incident electron population characteristics [*Hecht et al*., 2006; *Meier et al*., 1989; *Strickland et al*., 1999]. Furthermore, several recent studies have estimated the energy and flux of electron precipitation by using multispectral ground-based imager [*Grubbs et al*., 2018; *Lanchester et al*., 2009]. It is expected to determine the electron precipitation, which are driven by foreshock transients and magnetosheath HSJs, by revisiting the cases shown in Chapter 6, 7 and 8 with those techniques.

Bibliography

Allan, W., Poulter, E. M., Glassmeier, K.-H., & Junginger, H. (1985). Spatial and temporal structure of a high-latitude transient ULF pulsation. *Planetary and Space Science*, *33*(2), 159–173. https://doi.org/10.1016/0032-0633(85)90126-6

Angelopoulos, V. (2009). The THEMIS Mission. In J. L. Burch & V. Angelopoulos (Eds.), *The THEMIS Mission* (pp. 5–34). New York, NY: Springer New York. https://doi.org/10.1007/978-0-387-89820-9_2

Archer, M. O., & Horbury, T. S. (2013). Magnetosheath dynamic pressure enhancements: occurrence and typical properties. *Annales Geophysicae*, *31*(2), 319–331. https://doi.org/10.5194/angeo-31-319-2013

Archer, M. O., Horbury, T. S., & Eastwood, J. P. (2012). Magnetosheath pressure pulses: Generation downstream of the bow shock from solar wind discontinuities. *Journal of Geophysical Research: Space Physics*, *117*(A5). https://doi.org/10.1029/2011JA017468

Archer, M. O., Horbury, T. S., Eastwood, J. P., Weygand, J. M., & Yeoman, T. K. (2013). Magnetospheric response to magnetosheath pressure pulses: A low-pass filter effect. *Journal of Geophysical Research: Space Physics*, *118*(9), 5454–5466. https://doi.org/10.1002/jgra.50519

Archer, M. O., Turner, D. L., Eastwood, J. P., Horbury, T. S., & Schwartz, S. J. (2014). The role of pressure gradients in driving sunward magnetosheath flows and magnetopause motion. *Journal of Geophysical Research: Space Physics*, *119*(10), 8117–8125. https://doi.org/10.1002/2014JA020342

Ashour-Abdalla, M., & Kennel, C. F. (1978). Nonconvective and convective electron cyclotron harmonic instabilities. *Journal of Geophysical Research: Space Physics*, *83*(A4), 1531–1543. https://doi.org/10.1029/JA083iA04p01531

Axelsson, K., Sergienko, T., Nilsson, H., Brändström, U., Asamura, K., & Sakanoi, T. (2014). First negative system of N_2^+ in aurora: simultaneous space-borne and ground-based measurements and modeling results. *Annales Geophysicae*, *32*(5), 499–506. https://doi.org/10.5194/angeo-32-499-2014

Barbier, D., & Glaume, J. (1962). La couche ionosphérique nocturne F dans la zone intertropicale et ses relations avec l'émission de la raie 6300 Å du ciel nocturne. *Planetary and Space Science*, *9*(4), 133–148. https://doi.org/10.1016/0032-0633(62)90001-6

Billingham, L., Schwartz, S. J., & Wilber, M. (2011). Foreshock cavities and internal foreshock boundaries. *Planetary and Space Science*, *59*(7), 456–467. https://doi.org/10.1016/j.pss.2010.01.012

Blanco-Cano, X., Kajdič, P., Omidi, N., & Russell, C. T. (2011). Foreshock cavitons for different interplanetary magnetic field geometries: Simulations and observations. *Journal of Geophysical Research: Space Physics*, *116*(A9). https://doi.org/10.1029/2010JA016413

Burgess, D., Möbius, E., & Scholer, M. (2012). Ion Acceleration at the Earth's Bow Shock. *Space Science Reviews*, *173*(1), 5–47. https://doi.org/10.1007/s11214-012-9901-5

Burke, W. J., Kelley, M. C., Sagalyn, R. C., Smiddy, M., & Lai, S. T. (1979). Polar cap electric field structures with a northward interplanetary magnetic field. *Geophysical Research Letters*, *6*(1), 21–24. https://doi.org/10.1029/GL006i001p00021

Carlson, H. C., Moen, J., Oksavik, K., Nielsen, C. P., McCrea, I. W., Pedersen, T. R., & Gallop, P. (2006a). Direct observations of injection events of subauroral plasma into the polar cap. *Geophysical Research Letters*, *33*(5). https://doi.org/10.1029/2005GL025230

Carlson, H. C., Moen, J., Oksavik, K., Nielsen, C. P., McCrea, I. W., Pedersen, T. R., & Gallop, P. (2006b). Direct observations of injection events of subauroral plasma into the polar cap. *Geophysical Research Letters*, *33*(5), L05103. https://doi.org/10.1029/2005GL025230

Carlson, Herbert C. (2012). Sharpening our thinking about polar cap ionospheric patch morphology, research, and mitigation techniques. *Radio Science*, *47*(4). https://doi.org/10.1029/2011RS004946

Chen, L., & Hasegawa, A. (1974). A theory of long-period magnetic pulsations: 1. Steady state excitation of field line resonance. *Journal of Geophysical Research*, *79*(7), 1024–1032. https://doi.org/10.1029/JA079i007p01024

Chi, P. J., Lee, D.-H., & Russell, C. T. (2006). Tamao travel time of sudden impulses and its relationship to ionospheric convection vortices. *Journal of Geophysical Research: Space Physics*, *111*(A8). https://doi.org/10.1029/2005JA011578

Claudepierre, S. G., Hudson, M. K., Lotko, W., Lyon, J. G., & Denton, R. E. (2010). Solar wind driving of magnetospheric ULF waves: Field line resonances driven by dynamic pressure fluctuations. *Journal of Geophysical Research: Space Physics*, *115*(A11). https://doi.org/10.1029/2010JA015399

Coley, W. R., & Heelis, R. A. (1995). Adaptive identification and characterization of polar ionization patches. *Journal of Geophysical Research: Space Physics*, *100*(A12), 23819–23827. https://doi.org/10.1029/95JA02700

Cowley, S. W. H. (2013). Magnetosphere-Ionosphere Interactions: A Tutorial Review. In *Magnetospheric Current Systems* (pp. 91–106). American Geophysical Union (AGU). https://doi.org/10.1029/GM118p0091

Crooker, N. U., & Cliver, E. W. (1994). Postmodern view of M-regions. *Journal of Geophysical Research: Space Physics*, *99*(A12), 23383–23390. https://doi.org/10.1029/94JA02093

Crowley, G., Ridley, A. J., Deist, D., Wing, S., Knipp, D. J., Emery, B. A., et al. (2000). Transformation of high-latitude ionospheric F region patches into blobs during the March 21, 1990, storm. *Journal of Geophysical Research: Space Physics*, *105*(A3), 5215–5230. https://doi.org/10.1029/1999JA900357

Devine, P. E., Chapman, S. C., & Eastwood, J. W. (1995). One- and two-dimensional simulations of whistler mode waves in an anisotropic plasma. *Journal of Geophysical Research: Space Physics*, *100*(A9), 17189–17203. https://doi.org/10.1029/95JA00842

Dmitriev, A. V., & Suvorova, A. V. (2012). Traveling magnetopause distortion related to a large-scale magnetosheath plasma jet: THEMIS and ground-based observations. *Journal of Geophysical Research: Space Physics*, *117*(A8). https://doi.org/10.1029/2011JA016861

Drury, E. E., Mende, S. B., Frey, H. U., & Doolittle, J. H. (2003). Southern Hemisphere poleward moving auroral forms. *Journal of Geophysical Research: Space Physics*, *108*(A3). https://doi.org/10.1029/2001JA007536

Dungey, J. W. (1961). Interplanetary Magnetic Field and the Auroral Zones. *Physical Review Letters*, *6*(2), 47–48. https://doi.org/10.1103/PhysRevLett.6.47

Eastwood, J. P., Lucek, E. A., Mazelle, C., Meziane, K., Narita, Y., Pickett, J., & Treumann, R. A. (2005). The Foreshock. In G. Paschmann, S. J. Schwartz, C. P. Escoubet, & S. Haaland (Eds.), *Outer Magnetospheric Boundaries: Cluster Results* (pp. 41–94). Dordrecht: Springer Netherlands. https://doi.org/10.1007/1-4020-4582-4_3

Ebihara, Y., Tanaka, Y.-M., Takasaki, S., Weatherwax, A. T., & Taguchi, M. (2007). Quasi-stationary auroral patches observed at the South Pole Station. *Journal of Geophysical Research: Space Physics*, *112*(A1). https://doi.org/10.1029/2006JA012087

Echim, M. M., Maggiolo, R., Roth, M., & Keyser, J. D. (2009). A magnetospheric generator driving ion and electron acceleration and electric currents in a discrete auroral arc observed by Cluster and DMSP. *Geophysical Research Letters*, *36*(12). https://doi.org/10.1029/2009GL038343

Ellington, S. M., Moldwin, M. B., & Liemohn, M. W. (2016). Local time asymmetries and toroidal field line resonances: Global magnetospheric modeling in SWMF: TOROIDAL FIELD LINE RESONANCES. *Journal of Geophysical Research: Space Physics*, *121*(3), 2033–2045. https://doi.org/10.1002/2015JA021920

Engebretson, M., Glassmeier, K.-H., Stellmacher, M., Hughes, W. J., & Lühr, H. (1998). The dependence of high-latitude PcS wave power on solar wind velocity and on the phase of high-speed solar wind streams. *Journal of Geophysical Research: Space Physics*, *103*(A11), 26271–26283. https://doi.org/10.1029/97JA03143

Engebretson, M. J., Yeoman, T. K., Oksavik, K., Søraas, F., Sigernes, F., Moen, J. I., et al. (2013). Multi-instrument observations from Svalbard of a traveling convection vortex, electromagnetic ion cyclotron wave burst, and proton precipitation associated with a bow shock instability. *Journal of Geophysical Research: Space Physics*, *118*(6), 2975–2997. https://doi.org/10.1002/jgra.50291

Engebretson, Mark J., Moen, J., Posch, J. L., Lu, F., Lessard, M. R., Kim, H., & Lorentzen, D. A. (2009). Searching for ULF signatures of the cusp: Observations from search coil magnetometers and auroral imagers in Svalbard. *Journal of Geophysical Research: Space Physics*, *114*(A6). https://doi.org/10.1029/2009JA014278

Fairfield, D. H., Baumjohann, W., Paschmann, G., Lühr, H., & Sibeck, D. G. (1990). Upstream pressure variations associated with the bow shock and their effects on the magnetosphere. *Journal of Geophysical Research: Space Physics*, *95*(A4), 3773–3786. https://doi.org/10.1029/JA095iA04p03773

Farrugia, C. J., Gratton, F. T., Contin, J., Cocheci, C. C., Arnoldy, R. L., Ogilvie, K. W., et al. (2000). Coordinated Wind, Interball/tail, and ground observations of Kelvin-Helmholtz waves at the near-tail, equatorial magnetopause at dusk: January 11, 1997. *Journal of Geophysical Research: Space Physics*, *105*(A4), 7639–7667. https://doi.org/10.1029/1999JA000267

Farrugia, Charles J., Sandholt, P. E., Denig, W. F., & Torbert, R. B. (1998). Observation of a correspondence between poleward moving auroral forms and stepped cusp ion precipitation. *Journal of Geophysical Research: Space Physics*, *103*(A5), 9309–9315. https://doi.org/10.1029/97JA02882

Fasel, G. J., Minow, J. I., Smith, R. W., Deehr, C. S., & Lee, L. C. (1992). Multiple brightenings of transient dayside auroral forms during oval expansions. *Geophysical Research Letters*, *19*(24), 2429–2432. https://doi.org/10.1029/92GL02103

Fasel, Gerard J. (1995). Dayside poleward moving auroral forms: A statistical study. *Journal of Geophysical Research: Space Physics*, *100*(A7), 11891–11905. https://doi.org/10.1029/95JA00854

Fillingim, M. O., Eastwood, J. P., Parks, G. K., Angelopoulos, V., Mann, I. R., Mende, S. B., & Weatherwax, A. T. (2011). Polar UVI and THEMIS GMAG observations of the ionospheric response to a hot flow anomaly. *Journal of Atmospheric and Solar-Terrestrial Physics*, *73*(1), 137–145. https://doi.org/10.1016/j.jastp.2010.03.001

Fujita, S., Tanaka, T., Kikuchi, T., Fujimoto, K., Hosokawa, K., & Itonaga, M. (2003). A numerical simulation of the geomagnetic sudden commencement: 1. Generation of the field-aligned current associated with the preliminary impulse. *Journal of Geophysical Research: Space Physics*, *108*(A12). https://doi.org/10.1029/2002JA009407

Fuselier, S. A. (1995). Ion distributions in the Earth's foreshock upstream from the bow shock. *Advances in Space Research*, *15*(8), 43–52. https://doi.org/10.1016/0273-1177(94)00083-D

Fuselier, S. A., Klumpar, D. M., Shelley, E. G., Anderson, B. J., & Coates, A. J. (1991). He2+ and H+ dynamics in the subsolar magnetosheath and plasma depletion layer. *Journal of Geophysical Research: Space Physics*, *96*(A12), 21095–21104. https://doi.org/10.1029/91JA02145

Gallagher, D. L., Craven, P. D., & Comfort, R. H. (2000). Global core plasma model. *Journal of Geophysical Research: Space Physics*, *105*(A8), 18819–18833. https://doi.org/10.1029/1999JA000241

Glassmeier, K. H. (1995). ULF pulsations. In *Handbook of Atmospheric Electrodynamics* (pp. 463–502). CRC Press.

Gonzalez, W. D., Tsurutani, B. T., & Clúa de Gonzalez, A. L. (1999). Interplanetary origin of geomagnetic storms. *Space Science Reviews*, *88*(3), 529–562. https://doi.org/10.1023/A:1005160129098

Gosling, J. T. (1983). Ion acceleration at shocks in interplanetary space: A brief review of recent observations. *Space Science Reviews*, *34*(2), 113–126. https://doi.org/10.1007/BF00194621

Gosling, J. T., & Pizzo, V. J. (1999). Formation and Evolution of Corotating Interaction Regions and Their Three Dimensional Structure. In A. Balogh, J. T. Gosling, J. R. Jokipii, R. Kallenbach, & H. Kunow (Eds.), *Corotating Interaction Regions* (pp. 21–52). Springer Netherlands.

Gosling, J. T., McComas, D. J., & Phillips, J. L. (1991). *Counterstreaming solar wind halo electron events on open field lines* (No. LA-UR-91-3378; CONF-910915-3). Los Alamos National Lab., NM (United States). Retrieved from https://www.osti.gov/biblio/5008724

Grubbs, G., Michell, R., Samara, M., Hampton, D., Hecht, J., Solomon, S., & Jahn, J.-M. (2018). A Comparative Study of Spectral Auroral Intensity Predictions From Multiple Electron Transport Models. *Journal of Geophysical Research: Space Physics*, *123*(1), 993–1005. https://doi.org/10.1002/2017JA025026

Gulledge, I. S., Packer, D. M., Tilford, S. G., & Vanderslice, J. T. (1968). Intensity profiles of the 6300-A and 5577-A O I lines in the night airglow. *Journal of Geophysical Research*, *73*(17), 5535–5547. https://doi.org/10.1029/JA073i017p05535

Gupta, J. C. (1975). Long period Pc5 pulsations. *Planetary and Space Science*, *23*(5), 733–750. https://doi.org/10.1016/0032-0633(75)90012-4

Gussenhoven, M. S., Hardy, D. A., & Burke, W. J. (1981). DMSP/F2 electron observations of equatorward auroral boundaries and their relationship to magnetospheric electric fields.

Journal of Geophysical Research: Space Physics, *86*(A2), 768–778. https://doi.org/10.1029/JA086iA02p00768

Gutynska, O., Šimůnek, J., Šafránková, J., Němeček, Z., & Přech, L. (2012). Multipoint study of magnetosheath magnetic field fluctuations and their relation to the foreshock. *Journal of Geophysical Research: Space Physics*, *117*(A4). https://doi.org/10.1029/2011JA017240

Han, De-Sheng, Chen, X.-C., Liu, J.-J., Qiu, Q., Keika, K., Hu, Z.-J., et al. (2015). An extensive survey of dayside diffuse aurora based on optical observations at Yellow River Station. *Journal of Geophysical Research: Space Physics*, *120*(9), 7447–7465. https://doi.org/10.1002/2015JA021699

Han, D.-S., Nishimura, Y., Lyons, L. R., Hu, H.-Q., & Yang, H.-G. (2016). Throat aurora: The ionospheric signature of magnetosheath particles penetrating into the magnetosphere. *Geophysical Research Letters*, *43*(5), 1819–1827. https://doi.org/10.1002/2016GL068181

Han, D.-S., Hietala, H., Chen, X.-C., Nishimura, Y., Lyons, L. R., Liu, J.-J., et al. (2017). Observational properties of dayside throat aurora and implications on the possible generation mechanisms. *Journal of Geophysical Research: Space Physics*, *122*(2), 1853–1870. https://doi.org/10.1002/2016JA023394

Hao, Y., Lembege, B., Lu, Q., & Guo, F. (2016). Formation of downstream high-speed jets by a rippled nonstationary quasi-parallel shock: 2D hybrid simulations. *Journal of Geophysical Research: Space Physics*, *121*(3), 2080–2094. https://doi.org/10.1002/2015JA021419

Hao, Yufei, Gao, X., Lu, Q., Huang, C., Wang, R., & Wang, S. (2017). Reformation of rippled quasi-parallel shocks: 2D hybrid simulations. *Journal of Geophysical Research: Space Physics*, *122*(6), 6385–6396. https://doi.org/10.1002/2017JA024234

Hardy, D. A., Holeman, E. G., Burke, W. J., Gentile, L. C., & Bounar, K. H. (2008). Probability distributions of electron precipitation at high magnetic latitudes. *Journal of Geophysical Research: Space Physics*, *113*(A6). https://doi.org/10.1029/2007JA012746

Harrold, B. G., & Samson, J. C. (1992). Standing ULF modes of the magnetosphere: A theory. *Geophysical Research Letters*, *19*(18), 1811–1814. https://doi.org/10.1029/92GL01802

Hartinger, M. D., Turner, D. L., Plaschke, F., Angelopoulos, V., & Singer, H. (2013). The role of transient ion foreshock phenomena in driving Pc5 ULF wave activity. *Journal of Geophysical Research: Space Physics*, *118*(1), 299–312. https://doi.org/10.1029/2012JA018349

Hecht, J. H., Strickland, D. J., & Conde, M. G. (2006). The application of ground-based optical techniques for inferring electron energy deposition and composition change during auroral precipitation events. *Journal of Atmospheric and Solar-Terrestrial Physics*, *68*(13), 1502–1519. https://doi.org/10.1016/j.jastp.2005.06.022

Hietala, H., & Plaschke, F. (2013). On the generation of magnetosheath high-speed jets by bow shock ripples. *Journal of Geophysical Research: Space Physics*, *118*(11), 7237–7245. https://doi.org/10.1002/2013JA019172

Hietala, H., Laitinen, T. V., Andréeová, K., Vainio, R., Vaivads, A., Palmroth, M., et al. (2009). Supermagnetosonic Jets behind a Collisionless Quasiparallel Shock. *Physical Review Letters*, *103*(24), 245001. https://doi.org/10.1103/PhysRevLett.103.245001

Hietala, H., Partamies, N., Laitinen, T. V., Clausen, L. B. N., Facskó, G., Vaivads, A., et al. (2012). Supermagnetosonic subsolar magnetosheath jets and their effects: from the solar wind to the ionospheric convection. *Annales Geophysicae*, *30*(1), 33–48. https://doi.org/10.5194/angeo-30-33-2012

Hietala, H., Phan, T. D., Angelopoulos, V., Oieroset, M., Archer, M. O., Karlsson, T., & Plaschke, F. (2018). In Situ Observations of a Magnetosheath High-Speed Jet Triggering Magnetopause Reconnection. *Geophysical Research Letters*, *45*(4), 1732–1740. https://doi.org/10.1002/2017GL076525

Holmes, J. M., Johnsen, M. G., Deehr, C. S., Zhou, X.-Y., & Lorentzen, D. A. (2014). Circumpolar ground-based optical measurements of proton and electron shock aurora. *Journal of Geophysical Research: Space Physics*, *119*(5), 3895–3914. https://doi.org/10.1002/2013JA019574

Holzer, R. E., & Slavin, J. A. (1979). A correlative study of magnetic flux transfer in the magnetosphere. *Journal of Geophysical Research: Space Physics*, *84*(A6), 2573–2578. https://doi.org/10.1029/JA084iA06p02573

Horne, R. B., Thorne, R. M., Meredith, N. P., & Anderson, R. R. (2003). Diffuse auroral electron scattering by electron cyclotron harmonic and whistler mode waves during an isolated substorm. *Journal of Geophysical Research: Space Physics*, *108*(A7). https://doi.org/10.1029/2002JA009736

Hosokawa, K., Tsugawa, T., Shiokawa, K., Otsuka, Y., Ogawa, T., & Hairston, M. R. (2009). Unusually elongated, bright airglow plume in the polar cap F region: Is it a tongue of ionization? *Geophysical Research Letters*, *36*(7). https://doi.org/10.1029/2009GL037512

Hosokawa, K., St-Maurice, J.-P., Sofko, G. J., Shiokawa, K., Otsuka, Y., & Ogawa, T. (2010). Reorganization of polar cap patches through shears in the background plasma convection. *Journal of Geophysical Research: Space Physics*, *115*(A1). https://doi.org/10.1029/2009JA014599

Hosokawa, K., Moen, J. I., Shiokawa, K., & Otsuka, Y. (2011). Decay of polar cap patch. *Journal of Geophysical Research: Space Physics*, *116*(A5). https://doi.org/10.1029/2010JA016297

Hudson, P. D. (1970). Discontinuities in an anisotropic plasma and their identification in the solar wind. *Planetary and Space Science*, *18*(11), 1611–1622. https://doi.org/10.1016/0032-0633(70)90036-X

Hull, A. J., Bonnell, J. W., Mozer, F. S., & Scudder, J. D. (2003). A statistical study of large-amplitude parallel electric fields in the upward current region of the auroral acceleration region. *Journal of Geophysical Research: Space Physics*, *108*(A1), SMP 5-1-SMP 5-23. https://doi.org/10.1029/2001JA007540

Jacobsen, K. S., Phan, T. D., Eastwood, J. P., Sibeck, D. G., Moen, J. I., Angelopoulos, V., et al. (2009). THEMIS observations of extreme magnetopause motion caused by a hot flow anomaly. *Journal of Geophysical Research: Space Physics*, *114*(A8). https://doi.org/10.1029/2008JA013873

Kajdič, P., Blanco-Cano, X., Omidi, N., Rojas-Castillo, D., Sibeck, D. G., & Billingham, L. (2017). Traveling Foreshocks and Transient Foreshock Phenomena. *Journal of Geophysical Research: Space Physics*, *122*(9), 9148–9168. https://doi.org/10.1002/2017JA023901

Karimabadi, H., Roytershteyn, V., Vu, H. X., Omelchenko, Y. A., Scudder, J., Daughton, W., et al. (2014). The link between shocks, turbulence, and magnetic reconnection in collisionless plasmas. *Physics of Plasmas*, *21*(6), 062308. https://doi.org/10.1063/1.4882875

Karlson, K. A., Øieroset, M., Moen, J., & Sandholt, P. E. (1996). A statistical study of flux transfer event signatures in the dayside aurora: The IMF By -related prenoon-postnoon symmetry. *Journal of Geophysical Research: Space Physics*, *101*(A1), 59–68. https://doi.org/10.1029/95JA02590

Kepko, L., Spence, H. E., & Singer, H. J. (2002). ULF waves in the solar wind as direct drivers of magnetospheric pulsations. *Geophysical Research Letters*, *29*(8), 39-1-39–4. https://doi.org/10.1029/2001GL014405

Kivelson, M. G., & Southwood, D. J. (1986). Coupling of global magnetospheric MHD eigenmodes to field line resonances. *Journal of Geophysical Research: Space Physics*, *91*(A4), 4345–4351. https://doi.org/10.1029/JA091iA04p04345

Knox, F. B., & Allan, W. (1981). Damping and Coupling of Long-Period Hydromagnetic Waves by the Ionosphere. In D. J. Southwood (Ed.), *ULF Pulsations in the Magnetosphere: Reviews from the Special Sessions on Geomagnetic Pulsations at XVII General Assembly of the International Union for Geodesy and Geophysics, Canberra, 1979, December* (pp. 129–139). Dordrecht: Springer Netherlands. https://doi.org/10.1007/978-94-009-8426-4_8

Lanchester, B. S., Ashrafi, M., & Ivchenko, N. (2009). Simultaneous imaging of aurora on small scale in OI (777.4 nm) and $N_2$1P to estimate energy and flux of precipitation. *Annales Geophysicae*, *27*(7), 2881–2891. https://doi.org/10.5194/angeo-27-2881-2009

Le, G., & Russell, C. T. (1992). A study of ULF wave foreshock morphology—I: ULF foreshock boundary. *Planetary and Space Science*, *40*(9), 1203–1213. https://doi.org/10.1016/0032-0633(92)90077-2

Lee, D.-H., & Lysak, R. L. (1989). Magnetospheric ULF wave coupling in the dipole model: The impulsive excitation. *Journal of Geophysical Research: Space Physics*, *94*(A12), 17097–17103. https://doi.org/10.1029/JA094iA12p17097

Lei, W., Gendrin, R., Higel, B., & Berchem, J. (1981). Relationships between the solar wind electric field and the magnetospheric convection electric field. *Geophysical Research Letters*, *8*(10), 1099–1102. https://doi.org/10.1029/GL008i010p01099

Li, W., Thorne, R. M., Angelopoulos, V., Bortnik, J., Cully, C. M., Ni, B., et al. (2009). Global distribution of whistler-mode chorus waves observed on the THEMIS spacecraft. *Geophysical Research Letters*, *36*(9). https://doi.org/10.1029/2009GL037595

Li, W., Bortnik, J., Thorne, R. M., Nishimura, Y., Angelopoulos, V., & Chen, L. (2011). Modulation of whistler mode chorus waves: 2. Role of density variations. *Journal of Geophysical Research: Space Physics*, *116*(A6). https://doi.org/10.1029/2010JA016313

Lin, Y. (1997). Generation of anomalous flows near the bow shock by its interaction with interplanetary discontinuities. *Journal of Geophysical Research: Space Physics*, *102*(A11), 24265–24281. https://doi.org/10.1029/97JA01989

Lin, Y. (2002). Global hybrid simulation of hot flow anomalies near the bow shock and in the magnetosheath. *Planetary and Space Science*, *50*(5), 577–591. https://doi.org/10.1016/S0032-0633(02)00037-5

Lin, Y., & Wang, X. Y. (2005). Three-dimensional global hybrid simulation of dayside dynamics associated with the quasi-parallel bow shock. *Journal of Geophysical Research: Space Physics*, *110*(A12). https://doi.org/10.1029/2005JA011243

Lin, Y., Lee, L. C., & Yan, M. (1996a). Generation of dynamic pressure pulses downstream of the bow shock by variations in the interplanetary magnetic field orientation. *Journal of Geophysical Research: Space Physics*, *101*(A1), 479–493. https://doi.org/10.1029/95JA02985

Lin, Y., Swift, D. W., & Lee, L. C. (1996b). Simulation of pressure pulses in the bow shock and magnetosheath driven by variations in interplanetary magnetic field direction. *Journal of Geophysical Research: Space Physics*, *101*(A12), 27251–27269. https://doi.org/10.1029/96JA02733

Liu, Z., Turner, D. L., Angelopoulos, V., & Omidi, N. (2015). THEMIS observations of tangential discontinuity-driven foreshock bubbles. *Geophysical Research Letters*, *42*(19), 7860–7866. https://doi.org/10.1002/2015GL065842

Lockwood, M., & Carlson, H. C. (1992). Production of polar cap electron density patches by transient magnetopause reconnection. *Geophysical Research Letters*, *19*(17), 1731–1734. https://doi.org/10.1029/92GL01993

Lockwood, M., Fazakerley, A., Opgenoorth, H., Moen, J., Van Eyken, A. P., Dunlop, M., et al. (2001a). Coordinated Cluster and ground-based instrument observations of transient changes in the magnetopause boundary layer during an interval of predominantly northward IMF: relation to reconnection pulses and FTE signatures. *Annales Geophysicae*, *19*(10/12), 1613–1640.

Lockwood, M., Milan, S. E., Onsager, T., Perry, C. H., Scudder, J. A., Russell, C. T., & Brittnacher, M. (2001b). Cusp ion steps, field-aligned currents and poleward moving auroral forms. *Journal of Geophysical Research: Space Physics*, *106*(A12), 29555–29569. https://doi.org/10.1029/2000JA900175

Lockwood, M., Davies, J. A., Moen, J., Eyken, A. P. van, Oksavik, K., McCrea, I. W., & Lester, M. (2005). Motion of the dayside polar cap boundary during substorm cycles: II. Generation of poleward-moving events and polar cap patches by pulses in the magnetopause reconnection rate. *Annales Geophysicae*, *23*(11), 3513–3532. https://doi.org/10.5194/angeo-23-3513-2005

Lorentzen, D. A., Deehr, C. S., Minow, J. I., Smith, R. W., Stenbaek-Neielsen, H. C., Sigernes, F., et al. (1996). SCIFER-Dayside auroral signatures of magnetospheric energetic electrons. *Geophysical Research Letters*, *23*(14), 1885–1888. https://doi.org/10.1029/96GL00593

Lorentzen, D. A., Shumilov, N., & Moen, J. (2004). Drifting airglow patches in relation to tail reconnection. *Geophysical Research Letters*, *31*(2). https://doi.org/10.1029/2003GL017785

Lorentzen, D. A., Moen, J., Oksavik, K., Sigernes, F., Saito, Y., & Johnsen, M. G. (2010). In situ measurement of a newly created polar cap patch. *Journal of Geophysical Research: Space Physics*, *115*(A12). https://doi.org/10.1029/2010JA015710

Lorentzen, D. A., & Moen, J. (2000). Auroral proton and electron signatures in the dayside aurora. Journal of Geophysical Research, 105(A6), 12,733–12,745. https://doi.org/10.1029/1999JA900405

Lui, A. T. Y., & Sibeck, D. G. (1991). Dayside auroral activities and their implications for impulsive entry processes in the dayside magnetosphere. *Journal of Atmospheric and Terrestrial Physics*, *53*(3), 219–229. https://doi.org/10.1016/0021-9169(91)90106-H

Lyons, L. R. (1996). Substorms: Fundamental observational features, distinction from other disturbances, and external triggering. *Journal of Geophysical Research: Space Physics*, *101*(A6), 13011–13025. https://doi.org/10.1029/95JA01987

Lyons, L. R., Nagai, T., Blanchard, G. T., Samson, J. C., Yamamoto, T., Mukai, T., et al. (1999). Association between Geotail plasma flows and auroral poleward boundary intensifications observed by CANOPUS photometers. *Journal of Geophysical Research: Space Physics*, *104*(A3), 4485–4500. https://doi.org/10.1029/1998JA900140

Lyons, L. R., Nishimura, Y., Kim, H.-J., Donovan, E., Angelopoulos, V., Sofko, G., et al. (2011). Possible connection of polar cap flows to pre- and post-substorm onset PBIs and streamers. *Journal of Geophysical Research: Space Physics*, *116*(A12). https://doi.org/10.1029/2011JA016850

Lysak, R. L., & Lee, D. (1992). Response of the dipole magnetosphere to pressure pulses. *Geophysical Research Letters*, *19*(9), 937–940. https://doi.org/10.1029/92GL00625

MacDougall, J. W., & Jayachandran, P. T. (2001). Polar cap convection relationships with solar wind. *Radio Science*, *36*(6), 1869–1880. https://doi.org/10.1029/2001RS001007

Maltsev, Y. P., & Lyatsky, W. B. (1975). Field-aligned currents and erosion of the dayside magnetosphere. *Planetary and Space Science*, *23*(9), 1257–1260. https://doi.org/10.1016/0032-0633(75)90149-X

McDiarmid, D. R., & Allan, W. (1990). Simulation and analysis of auroral radar signatures generated by a magnetospheric cavity mode. *Journal of Geophysical Research: Space Physics*, *95*(A12), 20911–20922. https://doi.org/10.1029/JA095iA12p20911

McDiarmid, D. R., & Nielsen, E. (1987). Simultaneous observation of monochromatic and variable period geomagnetic pulsations. *Journal of Geophysical Research: Space Physics*, *92*(A5), 4449–4457. https://doi.org/10.1029/JA092iA05p04449

McDiarmid, D. R., Yeoman, T. K., Grant, I. F., & Allan, W. (1994). Simultaneous observation of a traveling vortex structure in the morning sector and a field line resonance in the postnoon sector. *Journal of Geophysical Research: Space Physics*, *99*(A5), 8891–8904. https://doi.org/10.1029/94JA00205

McWilliams, K. A., Yeoman, T. K., & Cowley, S. W. H. (2000). Two-dimensional electric field measurements in the ionospheric footprint of a flux transfer event. *Annales Geophysicae*, *18*(12), 1584–1598. https://doi.org/10.1007/s00585-001-1584-2

Meier, R. R., Strickland, D. J., Hecht, J. H., & Christensen, A. B. (1989). Deducing composition and incident electron spectra from ground-based auroral optical measurements: A study of auroral red line processes. *Journal of Geophysical Research: Space Physics*, *94*(A10), 13541–13552. https://doi.org/10.1029/JA094iA10p13541

Mende, S. B., Swenson, G. R., Geller, S. P., Viereck, R. A., Murad, E., & Pike, C. P. (1993). Limb view spectrum of the Earth's airglow. *Journal of Geophysical Research: Space Physics*, *98*(A11), 19117–19125. https://doi.org/10.1029/93JA02282

Mende, S. B., Frey, H. U., Geller, S. P., & Doolittle, J. H. (1999). Multistation observations of auroras: Polar cap substorms. *Journal of Geophysical Research: Space Physics*, *104*(A2), 2333–2342. https://doi.org/10.1029/1998JA900084

Mende, S. B., Frey, H. U., McFadden, J., Carlson, C. W., Angelopoulos, V., Glassmeier, K.-H., et al. (2009a). Coordinated observation of the dayside magnetospheric entry and exit of the THEMIS satellites with ground-based auroral imaging in Antarctica. *Journal of Geophysical Research: Space Physics*, *114*(A1). https://doi.org/10.1029/2008JA013496

Mende, S. B., Harris, S. E., Frey, H. U., Angelopoulos, V., Russell, C. T., Donovan, E., et al. (2009b). The THEMIS Array of Ground-based Observatories for the Study of Auroral Substorms. *The THEMIS Mission*, 357–387. https://doi.org/10.1007/978-0-387-89820-9_16

Meng, Ching-I., & Akasofu, S.-I. (1983). Electron precipitation equatorward of the auroral oval and the mantle aurora in the midday sector. *Planetary and Space Science*, *31*(8), 889–899. https://doi.org/10.1016/0032-0633(83)90144-7

Meng, C.-I., Mauk, B., & McIlwain, C. e. (1979). Electron precipitation of evening diffuse aurora and its conjugate electron fluxes near the magnetospheric equator. *Journal of Geophysical Research: Space Physics*, *84*(A6), 2545–2558. https://doi.org/10.1029/JA084iA06p02545

Milan, S. E., Lester, M., Cowley, S. W. H., & Brittnacher, M. (2000). Convection and auroral response to a southward turning of the IMF: Polar UVI, CUTLASS, and IMAGE signatures of transient magnetic flux transfer at the magnetopause. *Journal of Geophysical Research: Space Physics*, *105*(A7), 15741–15755. https://doi.org/10.1029/2000JA900022

Milan, Stephen E., Sato, N., Ejiri, M., & Moen, J. (2001). Auroral forms and the field-aligned current structure associated with field line resonances. *Journal of Geophysical Research: Space Physics*, *106*(A11), 25825–25833. https://doi.org/10.1029/2001JA900077

Moen, J., Sandholt, P. E., Lockwood, M., Denig, W. F., Løvhaug, U. P., Lybekk, B., et al. (1995). Events of enhanced convection and related dayside auroral activity. *Journal of Geophysical Research: Space Physics*, *100*(A12), 23917–23934. https://doi.org/10.1029/95JA02585

Moen, J., Gulbrandsen, N., Lorentzen, D. A., & Carlson, H. C. (2007). On the MLT distribution of F region polar cap patches at night. *Geophysical Research Letters*, *34*(14). https://doi.org/10.1029/2007GL029632

Moen, J., Rinne, Y., Carlson, H. C., Oksavik, K., Fujii, R., & Opgenoorth, H. (2008). On the relationship between thin Birkeland current arcs and reversed flow channels in the winter cusp/cleft ionosphere. *Journal of Geophysical Research: Space Physics*, *113*(A9). https://doi.org/10.1029/2008JA013061

Moen, J., Carlson, H. C., Rinne, Y., & Skjæveland, Å. (2012). Multi-scale features of solar terrestrial coupling in the cusp ionosphere. *Journal of Atmospheric and Solar-Terrestrial Physics*, *87–88*, 11–19. https://doi.org/10.1016/j.jastp.2011.07.002

Motoba, T., Kadokura, A., Ebihara, Y., Frey, H. U., Weatherwax, A. T., & Sato, N. (2009). Simultaneous ground-satellite optical observations of postnoon shock aurora in the Southern Hemisphere. *Journal of Geophysical Research: Space Physics*, *114*(A7). https://doi.org/10.1029/2008JA014007

Murr, D. L., & Hughes, W. J. (2003). Solar wind drivers of Traveling Convection Vortices. *Geophysical Research Letters*, *30*(7). https://doi.org/10.1029/2002GL015498

Nakamura, R., Baumjohann, W., Schödel, R., Brittnacher, M., Sergeev, V. A., Kubyshkina, M., et al. (2001). Earthward flow bursts, auroral streamers, and small expansions. *Journal of Geophysical Research: Space Physics*, *106*(A6), 10791–10802. https://doi.org/10.1029/2000JA000306

Němeček, Z., Šafránková, J., Přech, L., Sibeck, D. G., Kokubun, S., & Mukai, T. (1998). Transient flux enhancements in the magnetosheath. *Geophysical Research Letters*, *25*(8), 1273–1276. https://doi.org/10.1029/98GL50873

Newton, R. S., Southwood, D. J., & Hughes, W. J. (1978). Damping of geomagnetic pulsations by the ionosphere. *Planetary and Space Science*, *26*(3), 201–209. https://doi.org/10.1016/0032-0633(78)90085-5

Ni, B., Thorne, R. M., Shprits, Y. Y., & Bortnik, J. (2008). Resonant scattering of plasma sheet electrons by whistler-mode chorus: Contribution to diffuse auroral precipitation. *Geophysical Research Letters*, *35*(11). https://doi.org/10.1029/2008GL034032

Nishimura, Y., Bortnik, J., Li, W., Thorne, R. M., Lyons, L. R., Angelopoulos, V., et al. (2010a). Identifying the Driver of Pulsating Aurora. *Science*, *330*(6000), 81–84. https://doi.org/10.1126/science.1193186

Nishimura, Y., Lyons, L. R., Zou, S., Angelopoulos, V., & Mende, S. B. (2010b). Reply to comment by Harald U. Frey on "Substorm triggering by new plasma intrusion: THEMIS all-sky imager observations." *Journal of Geophysical Research: Space Physics*, *115*(A12). https://doi.org/10.1029/2010JA016182

Nishimura, Y., Lyons, L. R., Shiokawa, K., Angelopoulos, V., Donovan, E. F., & Mende, S. B. (2013). Substorm onset and expansion phase intensification precursors seen in polar cap patches and arcs. *Journal of Geophysical Research: Space Physics*, *118*(5), 2034–2042. https://doi.org/10.1002/jgra.50279

Nishimura, Y., Lyons, L. R., Zou, Y., Oksavik, K., Moen, J. I., Clausen, L. B., et al. (2014). Day-night coupling by a localized flow channel visualized by polar cap patch propagation. *Geophysical Research Letters*, *41*(11), 3701–3709. https://doi.org/10.1002/2014GL060301

Nishimura, Yukitoshi, Kikuchi, T., Ebihara, Y., Yoshikawa, A., Imajo, S., Li, W., & Utada, H. (2016). Evolution of the current system during solar wind pressure pulses based on aurora and magnetometer observations. *Earth, Planets and Space*, *68*(1), 144. https://doi.org/10.1186/s40623-016-0517-y

Øieroset, M., Sandholt, P. E., Denig, W. F., & Cowley, S. W. H. (1997). Northward interplanetary magnetic field cusp aurora and high-latitude magnetopause reconnection. *Journal of Geophysical Research: Space Physics*, *102*(A6), 11349–11362. https://doi.org/10.1029/97JA00559

Oksavik, K., Moen, J., & Carlson, H. C. (2004). High-resolution observations of the small-scale flow pattern associated with a poleward moving auroral form in the cusp. *Geophysical Research Letters*, *31*(11). https://doi.org/10.1029/2004GL019838

Oksavik, K., Moen, J., Carlson, H. C., Greenwald, R. A., Milan, S. E., Lester, M., et al. (2005). Multi-instrument mapping of the small-scale flow dynamics related to a cusp auroral transient. *Annales Geophysicae*, *23*(7), 2657–2670. https://doi.org/10.5194/angeo-23-2657-2005

Oksavik, K., Barth, V. L., Moen, J., & Lester, M. (2010). On the entry and transit of high-density plasma across the polar cap. *Journal of Geophysical Research: Space Physics*, *115*(A12). https://doi.org/10.1029/2010JA015817

Omidi, N., Sibeck, D. G., & Blanco-Cano, X. (2009). Foreshock compressional boundary. *Journal of Geophysical Research: Space Physics*, *114*(A8). https://doi.org/10.1029/2008JA013950

Omidi, N., Eastwood, J. P., & Sibeck, D. G. (2010). Foreshock bubbles and their global magnetospheric impacts. *Journal of Geophysical Research: Space Physics*, *115*(A6). https://doi.org/10.1029/2009JA014828

Omidi, N., Sibeck, D., Blanco-Cano, X., Rojas-Castillo, D., Turner, D., Zhang, H., & Kajdič, P. (2013). Dynamics of the foreshock compressional boundary and its connection to foreshock cavities. *Journal of Geophysical Research: Space Physics*, *118*(2), 823–831. https://doi.org/10.1002/jgra.50146

Parker, E. N. (1965). Dynamical theory of the solar wind. *Space Science Reviews*, *4*(5), 666–708. https://doi.org/10.1007/BF00216273

Parks, G. K., Lee, E., Mozer, F., Wilber, M., Lucek, E., Dandouras, I., et al. (2006). Larmor radius size density holes discovered in the solar wind upstream of Earth's bow shock. *Physics of Plasmas*, *13*(5), 050701. https://doi.org/10.1063/1.2201056

Paschmann, G., Sckopke, N., Papamastorakis, I., Asbridge, J. R., Bame, S. J., & Gosling, J. T. (1981). Characteristics of reflected and diffuse ions upstream from the Earth's bow shock. *Journal of Geophysical Research: Space Physics*, *86*(A6), 4355–4364. https://doi.org/10.1029/JA086iA06p04355

Paterson, W. R., Frank, L. A., Kokubun, S., & Yamamoto, T. (1998). Geotail survey of ion flow in the plasma sheet: Observations between 10 and 50 RE. *Journal of Geophysical Research: Space Physics*, *103*(A6), 11811–11825. https://doi.org/10.1029/97JA02881

Pinnock, M., Rodger, A. S., Dudeney, J. R., Baker, K. B., Newell, P. T., Greenwald, R. A., & Greenspan, M. E. (1993). Observations of an enhanced convection channel in the cusp ionosphere. *Journal of Geophysical Research: Space Physics*, *98*(A3), 3767–3776. https://doi.org/10.1029/92JA01382

Plaschke, F., & Glassmeier, K.-H. (2011). Properties of standing Kruskal-Schwarzschild-modes at the magnetopause. *Annales Geophysicae*, *29*(10), 1793–1807. https://doi.org/10.5194/angeo-29-1793-2011

Plaschke, F., Glassmeier, K.-H., Auster, H. U., Constantinescu, O. D., Magnes, W., Angelopoulos, V., et al. (2009). Standing Alfvén waves at the magnetopause. *Geophysical Research Letters*, *36*(2). https://doi.org/10.1029/2008GL036411

Plaschke, F., Hietala, H., & Angelopoulos, V. (2013). Anti-sunward high-speed jets in the subsolar magnetosheath. *Annales Geophysicae*, *31*(10), 1877–1889. https://doi.org/10.5194/angeo-31-1877-2013

Plaschke, F., Hietala, H., Angelopoulos, V., & Nakamura, R. (2016). Geoeffective jets impacting the magnetopause are very common. *Journal of Geophysical Research: Space Physics*, *121*(4), 3240–3253. https://doi.org/10.1002/2016JA022534

Provan, G., & Yeoman, T. K. (1999). Statistical observations of the MLT, latitude and size of pulsed ionospheric flows with the CUTLASS Finland radar. *Annales Geophysicae*, *17*(7), 855–867. https://doi.org/10.1007/s00585-999-0855-1

Provan, G., Yeoman, T. K., & Milan, S. E. (1998). CUTLASS Finland radar observations of the ionospheric signatures of flux transfer events and the resulting plasma flows. *Annales Geophysicae*, *16*(11), 1411–1422. https://doi.org/10.1007/s00585-998-1411-0

Provan, G., Yeoman, T. K., & Cowley, S. W. H. (1999). The influence of the IMF By component on the location of pulsed flows in the dayside ionosphere observed by an HF radar. *Geophysical Research Letters*, *26*(4), 521–524. https://doi.org/10.1029/1999GL900009

Rae, I. J., Mann, I. R., Dent, Z. C., Milling, D. K., Donovan, E. F., & Spanswick, E. (2007). Multiple field line resonances: Optical, magnetic and absorption signatures. *Planetary and Space Science*, *55*(6), 701–713. https://doi.org/10.1016/j.pss.2006.02.009

Rae, I. Jonathan, Mann, I. R., Murphy, K. R., Ozeke, L. G., Milling, D. K., Chan, A. A., et al. (2012). Ground-based magnetometer determination of in situ Pc4–5 ULF electric field wave spectra as a function of solar wind speed. *Journal of Geophysical Research: Space Physics*, *117*(A4). https://doi.org/10.1029/2011JA017335

Rankin, R., Kabin, K., Lu, J. Y., Mann, I. R., Marchand, R., Rae, I. J., et al. (2005). Magnetospheric field-line resonances: Ground-based observations and modeling. *Journal of Geophysical Research: Space Physics*, *110*(A10). https://doi.org/10.1029/2004JA010919

Rearwin, S., & Hones, E. W. (1974). Near-simultaneous measurement of low-energy electrons by sounding rocket and satellite. *Journal of Geophysical Research*, *79*(28), 4322–4325. https://doi.org/10.1029/JA079i028p04322

Reiff, P. H., & Burch, J. L. (1985). IMF By-dependent plasma flow and Birkeland currents in the dayside magnetosphere: 2. A global model for northward and southward IMF. *Journal of Geophysical Research*, *90*(A2), 1595. https://doi.org/10.1029/JA090iA02p01595

Rich, F. J., & Hairston, M. (1994). Large-scale convection patterns observed by DMSP. *Journal of Geophysical Research: Space Physics*, *99*(A3), 3827–3844. https://doi.org/10.1029/93JA03296

Rinne, Y., Moen, J., Oksavik, K., & Carlson, H. C. (2007). Reversed flow events in the winter cusp ionosphere observed by the European Incoherent Scatter (EISCAT) Svalbard radar. *Journal of Geophysical Research: Space Physics*, *112*(A10). https://doi.org/10.1029/2007JA012366

Rinne, Y., Moen, J., Carlson, H. C., & Hairston, M. R. (2010). Stratification of east-west plasma flow channels observed in the ionospheric cusp in response to IMF BY polarity changes. *Geophysical Research Letters*, *37*(13). https://doi.org/10.1029/2010GL043307

Ruohoniemi, J. M., Greenwald, R. A., Baker, K. B., & Samson, J. C. (1991). HF radar observations of Pc 5 field line resonances in the midnight/early morning MLT sector. *Journal of Geophysical Research: Space Physics*, *96*(A9), 15697–15710. https://doi.org/10.1029/91JA00795

Sakai, J., Hosokawa, K., Taguchi, S., & Ogawa, Y. (2014). Storm time enhancements of 630.0 nm airglow associated with polar cap patches. *Journal of Geophysical Research: Space Physics*, *119*(3), 2214–2228. https://doi.org/10.1002/2013JA019197

Samson, J. C., Jacobs, J. A., & Rostoker, G. (1971). Latitude-dependent characteristics of long-period geomagnetic micropulsations. *Journal of Geophysical Research*, *76*(16), 3675–3683. https://doi.org/10.1029/JA076i016p03675

Samson, J. C., Hughes, T. J., Creutzberg, F., Wallis, D. D., Greenwald, R. A., & Ruohoniemi, J. M. (1991). Observations of a detached, discrete arc in association with field line resonances. *Journal of Geophysical Research: Space Physics*, *96*(A9), 15683–15695. https://doi.org/10.1029/91JA00796

Samson, J. C., Harrold, B. G., Ruohoniemi, J. M., Greenwald, R. A., & Walker, A. D. M. (1992). Field line resonances associated with MHD waveguides in the magnetosphere. *Geophysical Research Letters*, *19*(5), 441–444. https://doi.org/10.1029/92GL00116

Sandholt, P. E., Denig, W. F., Farrugia, C. J., Lybekk, B., & Trondsen, E. (2002). Auroral structure at the cusp equatorward boundary: Relationship with the electron edge of low-latitude boundary layer precipitation. Journal of Geophysical Research, 107(A9), 1235. https://doi.org/10.1029/2001JA005081

Sandholt, P. E., & Farrugia, C. J. (2003). Does the aurora provide evidence for the occurrence of antiparallel magnetopause reconnection? *Journal of Geophysical Research: Space Physics*, *108*(A12), 1466. https://doi.org/10.1029/2003JA010066

Sandholt, P. E., & Farrugia, C. J. (2007). Poleward moving auroral forms (PMAFs) revisited: responses of aurorae, plasma convection and Birkeland currents in the pre- and postnoon sectors under positive and negative IMF By conditions. *Annales Geophysicae*, *25*(7), 1629–1652.

Sandholt, P. E., Egeland, A., Lybekk, B., Deehr, C. S., Sivjee, G. G., & Romick, G. J. (1983). Effects of interplanetary magnetic field and magnetospheric substorm variations on the dayside aurora. *Planetary and Space Science*, *31*(11), 1345–1362. https://doi.org/10.1016/0032-0633(83)90071-5

Sandholt, P. E., Deehr, C. S., Egeland, A., Lybekk, B., Viereck, R., & Romick, G. J. (1986). Signatures in the dayside aurora of plasma transfer from the magnetosheath. *Journal of Geophysical Research: Space Physics*, *91*(A9), 10063–10079. https://doi.org/10.1029/JA091iA09p10063

Sandholt, P. E., Lybekk, B., Egeland, A., Nakamura, R., & Oguti, T. (1989a). Midday Auroral Breakup. *Journal of Geomagnetism and Geoelectricity*, *41*(4), 371–387. https://doi.org/10.5636/jgg.41.371

Sandholt, P. E., Jacobsen, B., Lybekk, B., Egeland, A., Meng, C.-I., Newell, P. T., et al. (1989b). Structure and dynamics in the polar cleft: Coordinated satellite and ground-based observations in the prenoon sector. *Journal of Geophysical Research: Space Physics*, *94*(A7), 8928–8942. https://doi.org/10.1029/JA094iA07p08928

Sandholt, P. E., Moen, J., Rudland, A., Opsvik, D., Denig, W. F., & Hansen, T. (1993). Auroral event sequences at the dayside polar cap boundary for positive and negative interplanetary magnetic field BY. *Journal of Geophysical Research: Space Physics*, *98*(A5), 7737–7755. https://doi.org/10.1029/92JA02256

Sandholt, P. E., Farrugia, C. J., Cowley, S. W. H., & Lester, M. (2001). Dayside auroral bifurcation sequence during B y -dominated interplanetary magnetic field: Relationship with merging and lobe convection cells. *Journal of Geophysical Research: Space Physics*, *106*(A8), 15429–15444. https://doi.org/10.1029/2000JA900161

Sandholt, P. E., Farrugia, C. J., Denig, W. F., Cowley, S. W. H., & Lester, M. (2003). Spontaneous and driven cusp dynamics: Optical aurora, particle precipitation, and plasma convection. *Planetary and Space Science*, *51*(12), 797–812. https://doi.org/10.1016/S0032-0633(03)00114-4

Sandholt, P. E., Farrugia, C. J., & Denig, W. F. (2004). Dayside aurora and the role of IMF |By|/|Bz| detailed morphology and response to magnetopause reconnection. *Annales Geophysicae*, *22*(2), 613–628. https://doi.org/10.5194/angeo-22-613-2004

Sandholt, Per Even, & Farrugia, C. J. (1999). On the dynamic cusp aurora and IMF B y. *Journal of Geophysical Research: Space Physics*, *104*(A6), 12461–12472. https://doi.org/10.1029/1999JA900126

Savin, S., Amata, E., Zelenyi, L., Lutsenko, V., Safrankova, J., Nemecek, Z., et al. (2012). Super fast plasma streams as drivers of transient and anomalous magnetospheric dynamics. *Annales Geophysicae*, *30*(1), 1–7. https://doi.org/10.5194/angeo-30-1-2012

Schwartz, S. J. (1995). Hot flow anomalies near the Earth's bow shock. *Advances in Space Research*, *15*(8), 107–116. https://doi.org/10.1016/0273-1177(94)00092-F

Schwartz, Steven J., Burgess, D., Wilkinson, W. P., Kessel, R. L., Dunlop, M., & Lühr, H. (1992). Observations of short large-amplitude magnetic structures at a quasi-parallel shock. *Journal of Geophysical Research: Space Physics*, *97*(A4), 4209–4227. https://doi.org/10.1029/91JA02581

Sergeev, V. A., Angelopoulos, V., Gosling, J. T., Cattell, C. A., & Russell, C. T. (1996). Detection of localized, plasma-depleted flux tubes or bubbles in the midtail plasma sheet. *Journal of Geophysical Research: Space Physics*, *101*(A5), 10817–10826. https://doi.org/10.1029/96JA00460

Sergeev, V. A., Sauvaud, J.-A., Popescu, D., Kovrazhkin, R. A., Liou, K., Newell, P. T., et al. (2000). Multiple-spacecraft observation of a narrow transient plasma jet in the Earth's plasma sheet. *Geophysical Research Letters*, *27*(6), 851–854. https://doi.org/10.1029/1999GL010729

Shen, X.-C., Shi, Q., Wang, B., Zhang, H., Hudson, M. K., Nishimura, Y., et al. (2018). Dayside Magnetospheric and Ionospheric Responses to a Foreshock Transient on 25 June 2008: 1. FLR Observed by Satellite and Ground-Based Magnetometers. *Journal of Geophysical Research: Space Physics*, *123*(8), 6335–6346. https://doi.org/10.1029/2018JA025349

Shi, Q. Q., Hartinger, M., Angelopoulos, V., Zong, Q.-G., Zhou, X.-Z., Zhou, X.-Y., et al. (2013). THEMIS observations of ULF wave excitation in the nightside plasma sheet during sudden impulse events. *Journal of Geophysical Research: Space Physics*, *118*(1), 284–298. https://doi.org/10.1029/2012JA017984

Shue, J.-H., Song, P., Russell, C. T., Steinberg, J. T., Chao, J. K., Zastenker, G., et al. (1998). Magnetopause location under extreme solar wind conditions. *Journal of Geophysical Research: Space Physics*, *103*(A8), 17691–17700. https://doi.org/10.1029/98JA01103

Shue, J.-H., Chao, J.-K., Song, P., McFadden, J. P., Suvorova, A., Angelopoulos, V., et al. (2009). Anomalous magnetosheath flows and distorted subsolar magnetopause for radial

interplanetary magnetic fields. *Geophysical Research Letters*, *36*(18). https://doi.org/10.1029/2009GL039842

Sibeck, D. G. (1992). Transient events in the outer magnetosphere: Boundary waves or flux transfer events? *Journal of Geophysical Research: Space Physics*, *97*(A4), 4009–4026. https://doi.org/10.1029/91JA03017

Sibeck, D. G., Borodkova, N. L., Schwartz, S. J., Owen, C. J., Kessel, R., Kokubun, S., et al. (1999). Comprehensive study of the magnetospheric response to a hot flow anomaly. *Journal of Geophysical Research: Space Physics*, *104*(A3), 4577–4593. https://doi.org/10.1029/1998JA900021

Sibeck, D. G., Phan, T.-D., Lin, R., Lepping, R. P., & Szabo, A. (2002). Wind observations of foreshock cavities: A case study. *Journal of Geophysical Research: Space Physics*, *107*(A10), SMP 4-1-SMP 4-10. https://doi.org/10.1029/2001JA007539

Sitar, R. J., Baker, J. B., Clauer, C. R., Ridley, A. J., Cumnock, J. A., Papitashvili, V. O., et al. (1998). Multi-instrument analysis of the ionospheric signatures of a hot flow anomaly occurring on July 24, 1996. *Journal of Geophysical Research: Space Physics*, *103*(A10), 23357–23372. https://doi.org/10.1029/98JA01916

Sojka, J. J., Bowline, M. D., Schunk, R. W., Decker, D. T., Valladares, C. E., Sheehan, R., et al. (1993). Modeling polar cap F-region patches using time varying convection. *Geophysical Research Letters*, *20*(17), 1783–1786. https://doi.org/10.1029/93GL01347

Solomon, S. C., Hays, P. B., & Abreu, V. J. (1988). The auroral 6300 Å emission: Observations and modeling. *Journal of Geophysical Research: Space Physics*, *93*(A9), 9867–9882. https://doi.org/10.1029/JA093iA09p09867

Sonnerup, B. U. Ö. (1969). Acceleration of particles reflected at a shock front. *Journal of Geophysical Research*, *74*(5), 1301–1304. https://doi.org/10.1029/JA074i005p01301

Spreiter, J. R., Summers, A. L., & Alksne, A. Y. (1966). Hydromagnetic flow around the magnetosphere. *Planetary and Space Science*, *14*(3), 223–253. https://doi.org/10.1016/0032-0633(66)90124-3

Strickland, D. J., Cox, R. J., Meier, R. R., & Drob, D. P. (1999). Global O/N2 derived from DE 1 FUV dayglow data: Technique and examples from two storm periods. *Journal of Geophysical Research: Space Physics*, *104*(A3), 4251–4266. https://doi.org/10.1029/98JA02817

Takahashi, K., Kistler, L. M., Potemra, T. A., McEntire, R. W., & Zanetti, L. J. (1988). Magnetospheric ULF waves observed during the major magnetospheric compression of November 1, 1984. *Journal of Geophysical Research: Space Physics*, *93*(A12), 14369–14382. https://doi.org/10.1029/JA093iA12p14369

Takahashi, Kazue, Lee, D.-H., Merkin, V. G., Lyon, J. G., & Hartinger, M. D. (2016). On the origin of the dawn-dusk asymmetry of toroidal Pc5 waves. *Journal of Geophysical Research: Space Physics*, *121*(10), 9632–9650. https://doi.org/10.1002/2016JA023009

Tanaka, Y.-M., Ebihara, Y., Saita, S., Yoshikawa, A., Obana, Y., & Weatherwax, A. T. (2012). Poleward moving auroral arcs observed at the South Pole Station and the interpretation by field line resonances. *Journal of Geophysical Research: Space Physics*, *117*(A9). https://doi.org/10.1029/2012JA017899

Thomas, V. A., & Brecht, S. H. (1988). Evolution of diamagnetic cavities in the solar wind. *Journal of Geophysical Research: Space Physics*, *93*(A10), 11341–11353. https://doi.org/10.1029/JA093iA10p11341

Thorne, R. M., Ni, B., Tao, X., Horne, R. B., & Meredith, N. P. (2010). Scattering by chorus waves as the dominant cause of diffuse auroral precipitation. *Nature*, *467*(7318), 943–946. https://doi.org/10.1038/nature09467

Tsurutani, B. T., Zhou, X.-Y., Vasyliunas, V. M., Haerendel, G., Arballo, J. K., & Lakhina, G. S. (2001). Interplanetary Shocks, Magnetopause Boundary Layers and Dayside Auroras: The Importance of a Very Small Magnetospheric Region. *Surveys in Geophysics*, *22*(2), 101–130. https://doi.org/10.1023/A:1012952414384

Tsyganenko, N. A. (2002). A model of the near magnetosphere with a dawn-dusk asymmetry 1. Mathematical structure. *Journal of Geophysical Research: Space Physics*, *107*(A8), SMP 12-1-SMP 12-15. https://doi.org/10.1029/2001JA000219

Turner, D. L., Omidi, N., Sibeck, D. G., & Angelopoulos, V. (2013). First observations of foreshock bubbles upstream of Earth's bow shock: Characteristics and comparisons to HFAs. *Journal of Geophysical Research: Space Physics*, *118*(4), 1552–1570. https://doi.org/10.1002/jgra.50198

Valladares, C. E., Decker, D. T., Sheehan, R., Anderson, D. N., Bullett, T., & Reinisch, B. W. (1998). Formation of polar cap patches associated with north-to-south transitions of the interplanetary magnetic field. *Journal of Geophysical Research: Space Physics*, *103*(A7), 14657–14670. https://doi.org/10.1029/97JA03682

Vorobjev, V., & Zverev, V. (1993). Dayside aurora signatures associated with ionospheric travelling twin vortices. In *Airglow and Aurora* (Vol. 2050, pp. 27–37). International Society for Optics and Photonics. https://doi.org/10.1117/12.164828

Vorobjev, V. G., Gustafsson, G., Starkov, G. V., Feldstein, Y. I., & Shevnina, N. F. (1975). Dynamics of day and night aurora during substorms. *Planetary and Space Science*, *23*(2), 269–278. https://doi.org/10.1016/0032-0633(75)90132-4

Vorobjev, V. G., Yagodkina, O. I., Sibeck, D. G., Liou, K., & Meng, C.-I. (2001). Polar UVI observations of dayside auroral transient events. *Journal of Geophysical Research: Space Physics*, *106*(A12), 28897–28911. https://doi.org/10.1029/2000JA000396

Walker, A. D. M. (1987). Theory of magnetospheric standing hydromagnetic waves with large azimuthal wave number: 1. Coupled magnetosonic and Alfvén waves. *Journal of Geophysical Research: Space Physics*, *92*(A9), 10039–10045. https://doi.org/10.1029/JA092iA09p10039

Wang, S., Zong, Q., & Zhang, H. (2013). Cluster observations of hot flow anomalies with large flow deflections: 1. Velocity deflections. *Journal of Geophysical Research: Space Physics*, *118*(2), 732–743. https://doi.org/10.1002/jgra.50100

Weber, E. J., & Buchau, J. (1981). Polar cap F-layer auroras. *Geophysical Research Letters*, *8*(1), 125–128. https://doi.org/10.1029/GL008i001p00125

Weimer, D. R. (2005). Improved ionospheric electrodynamic models and application to calculating Joule heating rates. *Journal of Geophysical Research: Space Physics*, *110*(A5). https://doi.org/10.1029/2004JA010884

Wilder, F. D., Crowley, G., Eriksson, S., Newell, P. T., & Hairston, M. R. (2012). Ionospheric Joule heating, fast flow channels, and magnetic field line topology for IMF By-dominant conditions: Observations and comparisons with predicted reconnection jet speeds. *Journal of Geophysical Research: Space Physics*, *117*(A11). https://doi.org/10.1029/2012JA017914

Wright, A. N., & Allan, W. (1996). Structure, phase motion, and heating within Alfvén resonances. *Journal of Geophysical Research: Space Physics*, *101*(A8), 17399–17408. https://doi.org/10.1029/96JA01141

Wu, D. J., Chao, J. K., & Lepping, R. P. (2000). Interaction between an interplanetary magnetic cloud and the Earth's magnetosphere: Motions of the bow shock. *Journal of Geophysical Research: Space Physics*, *105*(A6), 12627–12638. https://doi.org/10.1029/1999JA000265

Xu, B.-L., Samson, J. C., Liu, W. W., Creutzberg, F., & Hughes, T. J. (1993). Observations of optical aurora modulated by resonant Alfvén waves. *Journal of Geophysical Research: Space Physics*, *98*(A7), 11531–11541. https://doi.org/10.1029/93JA00435

Yeoman, T. K., Lester, M., Cowley, S. W. H., Milan, S. E., Moen, J., & Sandholt, P. E. (1997). Simultaneous observations of the cusp in optical, DMSP and HF radar data. *Geophysical Research Letters*, *24*(17), 2251–2254. https://doi.org/10.1029/97GL02072

Yumoto, K. (1985). Low-frequency upstream wave as a probable source of low-latitude Pc 3–4 magnetic pulsations. *Planetary and Space Science*, *33*(2), 239–249. https://doi.org/10.1016/0032-0633(85)90133-3

Zhang, H., Sibeck, D. G., Zong, Q.-G., Gary, S. P., McFadden, J. P., Larson, D., et al. (2010). Time History of Events and Macroscale Interactions during Substorms observations of a series of hot flow anomaly events. *Journal of Geophysical Research: Space Physics*, *115*(A12). https://doi.org/10.1029/2009JA015180

Zhang, Q.-H., Zhang, B.-C., Liu, R.-Y., Dunlop, M. W., Lockwood, M., Moen, J., et al. (2011). On the importance of interplanetary magnetic field |By| on polar cap patch formation. *Journal of Geophysical Research: Space Physics*, *116*(A5). https://doi.org/10.1029/2010JA016287

Zhang, Q.-H., Zhang, B.-C., Moen, J., Lockwood, M., McCrea, I. W., Yang, H.-G., et al. (2013). Polar cap patch segmentation of the tongue of ionization in the morning convection cell. *Geophysical Research Letters*, *40*(12), 2918–2922. https://doi.org/10.1002/grl.50616

Zhang, Qing-He, Zhang, B.-C., Lockwood, M., Hu, H.-Q., Moen, J., Ruohoniemi, J. M., et al. (2013). Direct Observations of the Evolution of Polar Cap Ionization Patches. *Science*, *339*(6127), 1597–1600. https://doi.org/10.1126/science.1231487

Zhang, X. Y., Zong, Q.-G., Wang, Y. F., Zhang, H., Xie, L., Fu, S. Y., et al. (2010). ULF waves excited by negative/positive solar wind dynamic pressure impulses at geosynchronous orbit. *Journal of Geophysical Research: Space Physics*, *115*(A10). https://doi.org/10.1029/2009JA015016

Zhao, L. L., Zhang, H., & Zong, Q. G. (2017). Global ULF waves generated by a hot flow anomaly. *Geophysical Research Letters*, *44*(11), 5283–5291. https://doi.org/10.1002/2017GL073249

Zhou, C., Li, W., Thorne, R. M., Bortnik, J., Ma, Q., An, X., et al. (2015). Excitation of dayside chorus waves due to magnetic field line compression in response to interplanetary shocks. *Journal of Geophysical Research: Space Physics*, *120*(10), 8327–8338. https://doi.org/10.1002/2015JA021530

Zhou, X.-Y., Strangeway, R. J., Anderson, P. C., Sibeck, D. G., Tsurutani, B. T., Haerendel, G., et al. (2003). Shock aurora: FAST and DMSP observations. *Journal of Geophysical Research: Space Physics*, *108*(A4). https://doi.org/10.1029/2002JA009701

Zhou, X.-Y., Fukui, K., Carlson, H. C., Moen, J. I., & Strangeway, R. J. (2009). Shock aurora: Ground-based imager observations. *Journal of Geophysical Research: Space Physics*, *114*(A12). https://doi.org/10.1029/2009JA014186

Ziesolleck, C. W. S., & McDiarmid, D. R. (1994). Auroral latitude Pc 5 field line resonances: Quantized frequencies, spatial characteristics, and diurnal variation. *Journal of Geophysical Research: Space Physics*, *99*(A4), 5817–5830. https://doi.org/10.1029/93JA02903

Zong, Q.-G., & Zhang, H. (2011). On magnetospheric response to solar wind discontinuities. *Journal of Atmospheric and Solar-Terrestrial Physics*, *73*(1), 1–4. https://doi.org/10.1016/j.jastp.2010.11.001

Zong, Q.-G., Zhou, X.-Z., Wang, Y. F., Li, X., Song, P., Baker, D. N., et al. (2009). Energetic electron response to ULF waves induced by interplanetary shocks in the outer radiation

belt. *Journal of Geophysical Research: Space Physics*, *114*(A10). https://doi.org/10.1029/2009JA014393

Zou, Y., Nishimura, Y., Lyons, L. R., Donovan, E. F., Ruohoniemi, J. M., Nishitani, N., & McWilliams, K. A. (2014). Statistical relationships between enhanced polar cap flows and PBIs. *Journal of Geophysical Research: Space Physics*, *119*(1), 151–162. https://doi.org/10.1002/2013JA019269

Zou, Ying, Nishimura, Y., Lyons, L. R., Shiokawa, K., Donovan, E. F., Ruohoniemi, J. M., et al. (2015). Localized polar cap flow enhancement tracing using airglow patches: Statistical properties, IMF dependence, and contribution to polar cap convection. *Journal of Geophysical Research: Space Physics*, *120*(5), 4064–4078. https://doi.org/10.1002/2014JA020946